Hybrid Quantum Algorithms for Summary Statistics of Nonlinear PDEs with Random Initial Data *

Soo-Jong Rey

Kwangwoon University, Seoul 01897 Korea

Fields Institute for Research in Mathematical Sciences, Toronto ON M5T3J1 Canada

hexagon:2611.00575v1

Abstract

I develop a hybrid classical–quantum algorithm for summary statistics of nonlinear PDEs with Gaussian random initial data. Perturbative expansion and Wick's theorem reduce ensemble averages to deterministic momentum and time integrals. Classical interpolation and quantum amplitude estimation then evaluate these integrals with improved accuracy dependence for sufficiently smooth integrands, without quantum random-access memory. I apply the method to the Einstein–de Sitter Euler–Poisson perturbation theory developed by Goroff, Grinstein, Rey, and Wise. For the one-loop matter power spectrum, I establish the integrand regularity required by the algorithm under specified assumptions on the initial spectrum. Cubic nonlinear Schrödinger evolution provides a comparison involving resonances and diagram cancellations. I account separately for preprocessing and circuit costs.

Contents

1 Introduction **2**

2 From nonlinear evolution to integrals **5**

3 Quantum integration of the remaining error **10**

4 GGRW benchmark and random-wave comparison **14**
4.1 GGRW Euler–Poisson hierarchy 14
4.2 Random-wave comparison 18

5 Outlook **20**

A Deriving the integrals and bounding their derivatives **22**
A.1 Perturbative expansion and Gaussian averaging 22
A.2 Changes of variables and derivative bounds 25

B Quantum circuit and its cost **29**
B.1 Classical interpolation and quantum estimation of its residual 29
B.2 Reversible evaluation and total computational cost 35

*DOI 10.5281/zenodo.23736209

C Calibration with Burgers and Navier–Stokes **38**
C.1 Viscous Burgers equation 39
C.2 Incompressible Navier–Stokes equation 41

D GGRW technical details and Euler–Poisson singularities **44**
D.1 GGRW kernels and one-loop momentum integrals 44
D.2 Flat-space Euler–Poisson and caustic formation 50
D.3 Einstein–de Sitter expansion and algebraic damping 52
D.4 Euler–Poisson and forced Navier–Stokes singularities 55

E Random-wave Schrödinger equations and cancellation between diagrams **58**

F Non-Gaussian initial data, errors, and computational costs **61**
F.1 Non-Gaussian initial data and error control 61
F.2 Preprocessing and computational comparisons 64

1 Introduction

Galaxies form clusters, walls, and filaments separated by large voids. The cosmic web grew from small primordial density perturbations originating in quantum fluctuations of the early universe [1–6]. Their statistics are nearly Gaussian, with a nearly scale-invariant primordial power spectrum. Gravitational instability amplified these perturbations as the Universe evolved. Matter flowed toward over-dense regions and away from under-dense regions, forming the large-scale structures of the Universe. The ensuing nonlinear evolution coupled Fourier modes and generated correlations among them.

With Goroff, Grinstein, and Wise, I studied nonlinear density correlations in an Einstein–de Sitter (EdS) universe (GGRW) [7] [1]. The model treated matter as a pressureless Newtonian fluid (dust), governed by the Euler-Poisson equation. I specified Gaussian initial density fluctuations with a Harrison–Zel'dovich primordial power spectrum modified by a cold-dark-matter transfer function. Perturbation theory determined the nonlinear density kernels order by order. Gaussian contraction then reduced the resulting density correlations and smoothed-density moments to momentum integrals.

The GGRW Euler–Poisson system is an example of deterministic nonlinear evolution with random initial conditions. More generally, I consider nonlinear partial differential equations (PDEs) of the form [10, 11]

$$\partial_t u(\mathbf{x}, t) = \mathcal{L}[u(\mathbf{x}, t)], \qquad u(\mathbf{x}, 0) = \xi(\mathbf{x}), \qquad \xi \sim \mu_0. \tag{1.1}$$

Here μ_0 is the probability distribution of the initial field $\xi(\mathbf{x})$. For a prescribed observable $\mathcal{O}$ at time $T > 0$, I seek its ensemble expectation

$$Q(T) = \mathbb{E}_{\mu_0}\left[\mathcal{O}(u(T))\right]. \tag{1.2}$$

A direct Monte Carlo calculation estimates $Q(T)$ by solving the nonlinear PDE Eq. (1.1) for independently sampled initial fields ξ and then averaging $\mathcal{O}(u(T;\xi))$ over μ_0.

The computational demands of fully nonlinear cosmological evolution are illustrated by large-scale N-body simulations. Quijote performed 44,100 simulations spanning more than 7,000 cosmological models, requiring over 35 million core hours [12]. AbacusSummit evolved

[1] Related perturbative results for cosmological correlation functions were obtained by Fry [8]. A broader review is given by Bernardeau et al. [9].

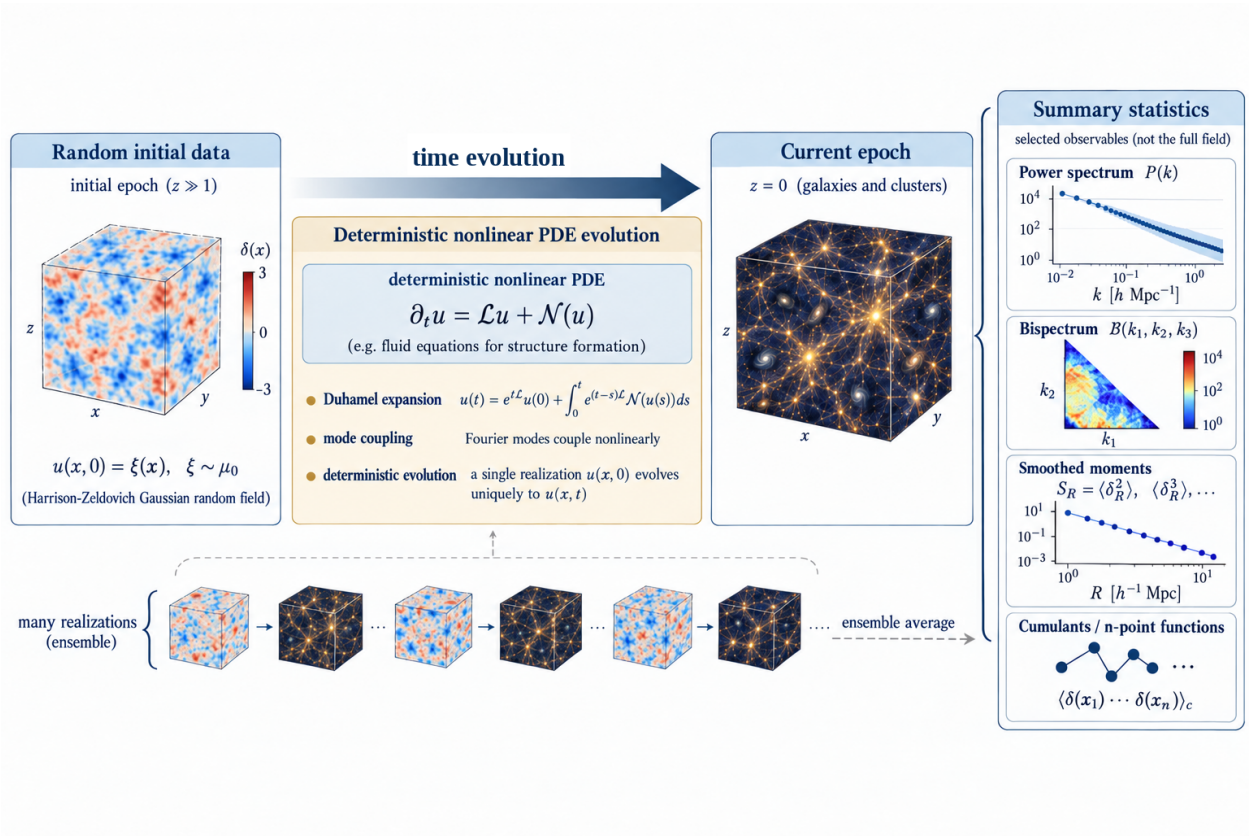


Figure 1: *Schematic illustration of the evolution from primordial density fluctuations to statistical observables. A random initial field evolves under the deterministic Euler–Poisson equations. An ensemble of evolved fields defines the power spectrum, bispectrum, smoothed density moments, and connected correlations. I develop a quantum algorithm to evaluate their fixed-order perturbative contributions after Gaussian averaging reduces them to momentum integrals.*

nearly 60 trillion particles across 97 cosmological models [13]. These computational costs concern nonlinear simulations, not the evaluation of fixed-order perturbative coefficients. Quantum algorithms have also addressed linearized Vlasov–Poisson plasma dynamics and gravitationally driven neutrino Vlasov evolution, while recent studies have investigated nonlinear electrostatic Vlasov–Poisson evolution [14–17].

More broadly, quantum algorithms for differential equations have been developed using linear evolution methods [18–20], Carleman and related nonlinear embeddings [21–24], and Liouville, Koopman, and level-set formulations [25, 26]. Other approaches address nonlinear unitary dynamics [27], uncertainty quantification for PDEs [28], and stochastic nonlinear evolution [29–31]. These methods provide alternative representations of differential evolution or its statistical observables, with different requirements for state preparation, stability, and measurement.

In this work, I develop a hybrid classical–quantum algorithm for evaluating fixed-order perturbative contributions to cosmological summary statistics, including the matter power spectrum, bispectrum, higher connected density correlation functions, and moments and cumulants of the smoothed density contrast. I examine the one-loop power spectrum as the first explicit GGRW application, deriving its momentum regularity and quantum integration bound. Higher-order applications require corresponding bounds for simultaneous soft and hard loop momenta.

For the EdS growing solution, the nth-order density perturbation is proportional to $a^n(t)$,

where $a(t)$ is the cosmological scale factor. Its momentum dependence is determined by the GGRW kernel $F_n^{(s)}$ convolved with n initial density amplitudes. I apply Wick's theorem to their Gaussian ensemble averaging. Each contraction contributes the linear matter power spectrum $P_0(\mathbf{k})$, while momentum conservation eliminates dependent integration variables. The resulting statistical correlations are momentum integrals with explicit powers of the scale factor a.

The convergence and differentiability of these integrals depend on the initial power spectrum and the momentum structure of the gravitational kernels. In particular, the leading contributions of large nearly opposite momenta cancel within the symmetrized kernels, suppressing their coupling to long-wavelength density perturbations. I retain these cancellations in the complete kernels and transform the momentum integrals to establish bounded derivatives.

I integrate each transformed function by separating a classically calculated coarse approximation from its remaining error. For an integrand f on $[0,1]^D$, the derivative analysis supplies the following bound for an integer $r \geq 2$.

$$\|f\|_{W_\infty^r} \leq M. \tag{1.3}$$

On a mesh of spacing h, a local interpolating polynomial of degree $(r-1)$ obeys

$$\|f - \Pi_h f\|_\infty \leq c_{D,r} M h^r. \tag{1.4}$$

I integrate $\Pi_h f$ classically using $O(h^{-D})$ function values. A reversible circuit evaluates the residual $f - \Pi_h f$ at requested points. Quantum amplitude estimation integrates that residual to absolute error ϵ with $O(Mh^r/\epsilon)$ further evaluations. Balancing the two costs gives the asymptotics

$$h \asymp \left(\frac{\epsilon}{M}\right)^{1/(D+r)}, \qquad N_Q = O_{D,r}\left[\left(\frac{M}{\epsilon}\right)^{D/(D+r)}\right]. \tag{1.5}$$

Here N_Q counts both the classical function evaluations used to construct the interpolation and the coherent evaluations used to estimate its residual, with D and r fixed. The interpolation-and-residual construction and its quantum integration exponent follow from Novak and Heinrich [32–34]. For the same bounded-derivative input class, the optimal randomized classical integration rate is

$$N_{\mathrm{C,rand}} = O_{D,r}\left[\left(\frac{M}{\epsilon}\right)^{2D/(D+2r)}\right]. \tag{1.6}$$

These rates provide the worst-case function-query comparison between randomized classical and quantum integration.

The circuit evaluates f and its local interpolating polynomial reversibly for each midpoint label in a coherent superposition. It recomputes the r^D interpolation-node values rather than retrieving a precomputed table from quantum memory. Section 3 derives the estimator, while Appendix B establishes its gate count, numerical precision requirements, and quadrature error.

The quantum bound derived above requires momentum integrands with controlled derivatives. I first examine their construction in two simpler fluid equations. For viscous Burgers evolution, I derive the time-integrated quadratic kernel, remove its apparent singularity, and verify the Gaussian contractions. In incompressible Navier–Stokes evolution, the same perturbative calculation introduces transverse momentum projectors and tensor covariances whose singular momentum limits require separate treatment. I give both calculations in Appendix C before applying the method to the GGRW hierarchy.

I use the one-loop GGRW power spectrum to establish an explicit application of the quantum integration algorithm. The one-loop correction is $P_{22}(k) + P_{13}(k)$. I analyze the soft

and hard momentum limits of P_{22} and the complete rational and logarithmic kernel of P_{13}. For a linear matter spectrum satisfying the regularity conditions of Appendix D, the transformed integrands have two bounded derivatives and at most three momentum coordinates. The corresponding combined function-evaluation bound is

$$N_Q^{\mathrm{1loop}} = O\left[\left(\frac{M_{\mathrm{1loop}}}{\epsilon}\right)^{3/5}\right]. \tag{1.7}$$

The bound concerns the fixed one-loop coefficient and includes the classical interpolation stage. It uses the unreduced three-dimensional loop momentum. For isotropic spectra, rotational symmetry reduces P_{22} to two momentum coordinates and P_{13} to one. Specialized classical algorithms such as FAST-PT and FFTLog also exploit the convolution structure of these integrals [35, 36]. Appendix D gives the kernel expressions, momentum integrations, and derivative estimates.

I also examine cubic nonlinear Schrödinger evolution with Gaussian random initial Fourier amplitudes. Its finite-time resonance factors are regular, while the kinetic-limit analysis requires cancellations among families of paired diagrams [37]. Gravitational perturbation theory likewise involves cancellations both within symmetrized kernels and between different diagrams, although their momentum and time structures differ. The random-wave calculation illustrates the corresponding finite-order Gaussian contractions and conservation identities without establishing a separate quantum integration complexity bound. Appendix E develops this calculation [2].

The resulting quantum complexity estimates apply to fixed-order integrals with established derivative bounds. Determining an end-to-end advantage for the corresponding physical observables requires comparison with classical algorithms using the same spectra, interaction kernels, and accuracy requirements, including preprocessing and integrand-evaluation costs.

2 From nonlinear evolution to integrals

Consider m field components $u_a(\mathbf{x}, t)$ in d spatial dimensions. I use the Fourier convention

$$\begin{aligned}
\widehat{u}_a(\mathbf{k}, t) &= \int_{\mathbb{R}^d} e^{-\mathrm{i}\mathbf{k}\cdot\mathbf{x}} u_a(\mathbf{x}, t)\, \mathrm{d}^d x, \\
u_a(\mathbf{x}, t) &= \int_{\mathbb{R}^d} \frac{\mathrm{d}^d k}{(2\pi)^d} e^{\mathrm{i}\mathbf{k}\cdot\mathbf{x}} \widehat{u}_a(\mathbf{k}, t).
\end{aligned} \tag{2.1}$$

On a periodic domain, the momentum integrals become Fourier sums. For translation-invariant polynomial evolution, Eq. (1.1) takes the form

$$\begin{aligned}
\partial_t \widehat{u}_a(\mathbf{k}, t) = &\sum_{b=1}^{m} L_{ab}(\mathbf{k}, t) \widehat{u}_b(\mathbf{k}, t) \\
&+ \sum_{q=2}^{p} g_q \sum_{b_1,\ldots,b_q=1}^{m} \int \left[\prod_{j=1}^{q-1} \frac{\mathrm{d}^d k_j}{(2\pi)^d}\right] \\
&\times V^{(q)}_{a;b_1\cdots b_q}(\mathbf{k}_1, \ldots, \mathbf{k}_q; t) \prod_{j=1}^{q} \widehat{u}_{b_j}(\mathbf{k}_j, t),
\end{aligned} \tag{2.2}$$

[2] I apologize to cosmological readers for the cosmic emphasis on quantum-computing methods and terminology. This emphasis is deliberate and central to the results of this paper.

where momentum conservation fixes

$$\mathbf{k}_q = \mathbf{k} - \sum_{j=1}^{q-1} \mathbf{k}_j. \tag{2.3}$$

The matrix L_{ab} governs linear evolution and component mixing. The q-field interaction has coupling g_q and momentum kernel $V^{(q)}$, and p is the highest polynomial degree. Spatial derivatives and constraints enter through these kernels.

The propagator $S_{ab}(t, s; \mathbf{k})$ defined by the linear part of Eq.(2.2) satisfies

$$\partial_t S_{ab}(t, s; \mathbf{k}) = \sum_{c=1}^{m} L_{ac}(\mathbf{k}, t) S_{cb}(t, s; \mathbf{k}), \qquad S_{ab}(s, s; \mathbf{k}) = \delta_{ab}. \tag{2.4}$$

For the initial field $u_a(\mathbf{x}, 0) = \xi_a(\mathbf{x})$ given in Eq.(1.1), the linear solution is

$$\widehat{u}_a^{[0]}(\mathbf{k}, t) = \sum_{b=1}^{m} S_{ab}(t, 0; \mathbf{k}) \widehat{\xi}_b(\mathbf{k}). \tag{2.5}$$

I take the initial fields to be centered, jointly Gaussian, and statistically homogeneous. Their Fourier covariance is

$$\mathbb{E}_{\mu_0}\left[\widehat{\xi}_a(\mathbf{k}) \widehat{\xi}_b(\mathbf{k}')\right] = (2\pi)^d \delta^{(d)}(\mathbf{k} + \mathbf{k}') C_{ab}(\mathbf{k}). \tag{2.6}$$

Here μ_0 is the probability distribution of the initial field. For a real scalar field, C is its power spectrum. For several components, C_{ab} also gives their cross correlations. The delta function expresses statistical translation invariance. For complex fields, I include the field and its conjugate among the jointly Gaussian components.

The observable $\mathcal{O}[u(\cdot)]$ is a product of n prescribed linear measurements of the evolved fields. With momentum weights $w_{j,a}(\mathbf{k})$ (furnished by window function and bias), define

$$X_j(T) = \sum_{a=1}^{m} \int_{\mathbb{R}^d} \frac{\mathrm{d}^d k}{(2\pi)^d} w_{j,a}(\mathbf{k}) \widehat{u}_a(\mathbf{k}, T), \tag{2.7}$$

so that

$$\mathcal{O}[u(T)] = \prod_{j=1}^{n} X_j(T) = \prod_{j=1}^{n} \left[\sum_{a=1}^{m} \int_{\mathbb{R}^d} \frac{\mathrm{d}^d k}{(2\pi)^d} w_{j,a}(\mathbf{k}) \widehat{u}_a(\mathbf{k}, T) \right]. \tag{2.8}$$

The ensemble averages of these products give smoothed moments and Fourier correlation functions. Connected correlations are obtained by subtracting disconnected products, with perturbative orders distributed among their factors as required by the moment–cumulant formula.

I multiply the nonlinear part of Eq. (2.2) by a formal parameter z, leaving the couplings g_q unchanged, and expand

$$\widehat{u}_a(\mathbf{k}, t; z) = \sum_{\ell=0}^{\infty} z^\ell \widehat{u}_a^{[\ell]}(\mathbf{k}, t). \tag{2.9}$$

The coefficient of z^ℓ contains ℓ nonlinear interaction vertices. The physical evolution corresponds to $z = 1$. Dyson's recursion formula (Duhamel's formula) determines these coefficients

recursively. For a quadratic interaction,

$$\begin{aligned}\widehat{u}_a^{[\ell]}(\mathbf{k},t) = g_2 \int_0^t \mathrm{d}s \sum_{a'=1}^{m} S_{aa'}(t,s;\mathbf{k}) \sum_{\substack{\ell_1,\ell_2\geq 0\\ \ell_1+\ell_2=\ell-1}} \sum_{b,c=1}^{m} \\ \times \int_{\mathbb{R}^d} \frac{\mathrm{d}^d q}{(2\pi)^d} V^{(2)}_{a';bc}(\mathbf{q},\mathbf{k}-\mathbf{q};s) \\ \times \widehat{u}_b^{[\ell_1]}(\mathbf{q},s)\widehat{u}_c^{[\ell_2]}(\mathbf{k}-\mathbf{q},s), \qquad \ell \geq 1. \end{aligned} \tag{2.10}$$

The interaction at time s joins two fields of orders ℓ_1 and ℓ_2, with $\ell_1 + \ell_2 = \ell - 1$, since the interaction itself contributes one vertex. Repeated substitution generates rooted interaction trees. Each vertex contributes an interaction kernel and a time integral, each internal line contributes a linear propagator, and each leaf contributes a factor of $\widehat{\xi}$. Since the zeroth-order solution is linear in $\widehat{\xi}$, a tree with ℓ quadratic vertices has $\ell + 1$ leaves, as follows recursively from $(\ell_1 + 1) + (\ell_2 + 1) = \ell + 1$.

To extract the contribution of total interaction order K to the statistical observable, write

$$X_j(T;z) = \sum_{\ell\geq 0} z^\ell X_j^{[\ell]}(T), \tag{2.11}$$

where $X_j^{[\ell]}$ is the same linear measurement applied to $\widehat{u}^{[\ell]}$. Then

$$\begin{aligned} Q_K(T) &= [z^K]\, \mathbb{E}_{\mu_0}\left[\mathcal{O}[u(T;z)]\right] \\ &= \sum_{\substack{\ell_1,\ldots,\ell_n\geq 0\\ \ell_1+\cdots+\ell_n=K}} \mathbb{E}_{\mu_0}\left[\prod_{j=1}^{n} X_j^{[\ell_j]}(T)\right]. \end{aligned} \tag{2.12}$$

For quadratic evolution, every term on the second line contains $\sum_j(\ell_j + 1) = n + K$ initial amplitudes. For example, the order-$K = 2$ two-point function receives contributions with $(\ell_1, \ell_2) = (0, 2), (1, 1), (2, 0)$. Each contains four initial amplitudes, irrespective of how the two interaction vertices are distributed. In the GGRW power spectrum, these distributions produce the 13 and 22 contributions.

Wick's theorem performs the Gaussian average. For the quadratic case with $n + K = 2s$, it states

$$\begin{aligned} &\mathbb{E}_{\mu_0}\left[\prod_{i=1}^{2s} \widehat{\xi}_{a_i}(\mathbf{k}_i)\right] \\ &\quad = \sum_{\mathcal{P}\in\mathfrak{P}_{2s}} \prod_{(i,j)\in\mathcal{P}} \left[(2\pi)^d \delta^{(d)}(\mathbf{k}_i + \mathbf{k}_j) C_{a_i a_j}(\mathbf{k}_i)\right], \end{aligned} \tag{2.13}$$

where $\mathfrak{P}_{2s}$ denotes all pairings of the $2s$ indices. Each pairing contributes s covariance factors and their momentum delta functions. For odd $n + K$, the centered Gaussian expectation vanishes. The delta functions fix opposite momenta within each pair. Momentum conservation at the interaction vertices imposes further relations, so the dependent momenta can be integrated out. The remaining coefficient has the deterministic form

$$Q_K(T) = \sum_B \int_{\mathcal{D}_B} A_B(\mathbf{q},\mathbf{t})\, \mathrm{d}\mathbf{q}\, \mathrm{d}\mathbf{t}. \tag{2.14}$$

Here $\mathbf{q}$ collects the independent momentum variables and $\mathbf{t}$ the ordered interaction times. Each A_B contains the resulting covariance spectra, interaction kernels, linear propagators,

observable weights, and combinatorial coefficients. The index B groups contributions that have been expressed in the same integration variables, including the Jacobians of any changes of variables needed to combine them. Fourier correlations at fixed external momenta carry an overall conservation delta function, which is factored out in their reduced definition.

Proposition 1 (Reduction to integrals at fixed order)**.** *Fix the spatial dimension d, the number of field components m, maximal nonlinear degree p, observable degree n, perturbative order K, and final time T. For the regularized evolution Eq.*(2.2) *with Gaussian initial data Eq.*(2.6)*, the coefficient $Q_K(T)$ is a finite sum of deterministic momentum and time integrals. On a periodic domain with a Fourier cutoff, the momentum integrals are finite sums. The number of independent momentum and time coordinates is bounded in terms of d, p, n, K, independently of the number of Fourier modes.*

Proof. Each interaction vertex of degree q_v replaces one field by q_v fields. Thus a term with K vertices in an observable of degree n contains

$$N_\xi = n + \sum_{v=1}^{K} (q_v - 1) \le n + K(p-1) \tag{2.15}$$

initial amplitudes. At fixed K there are finitely many interaction trees and Gaussian pairings. Before momentum conservation is imposed, there are at most dN_ξ momentum coordinates and K interaction times. Therefore a bound on the total number of integration coordinates is

$$D_G \le d[n + K(p-1)] + K. \tag{2.16}$$

Covariance pairings and vertex delta functions reduce this number. Increasing a Fourier cutoff changes the integration ranges or the number of terms in each sum, but not the number of independent momentum coordinates. □

The dimension bound in Eq. (2.16) fixes the number of integration variables but does not control the derivatives of the integrands. The polynomial approximation used in Section 3 requires such control. I therefore examine the momentum dependence of each A_B before estimating its derivatives.

Cancellations can improve the behavior of the integrands in singular momentum limits. In GGRW, symmetrized gravitational kernels suppress the coupling of two large nearly opposite momenta to a fixed external momentum. In incompressible fluid evolution, transverse projectors remove longitudinal contributions. Time integrations can also produce apparent singularities that disappear in the full expression. For example,

$$\Phi_T(\Omega) = \int_0^T e^{\mathrm{i}\Omega s}\,\mathrm{d}s = \frac{e^{\mathrm{i}\Omega T} - 1}{\mathrm{i}\Omega}, \qquad \Phi_T(0) = T. \tag{2.17}$$

The apparent pole at $\Omega = 0$ is removable. I evaluate the complete kernels and time integrals before estimating their derivatives. When cancellations between different diagrams are required for convergence, bounded derivatives, or stable numerical evaluation, I combine their contributions in common integration variables. Separately controlled integrals may remain separate when this preserves lower-dimensional representations.

I divide each integration domain into finitely many regions adapted to soft momenta, large momenta, vanishing partial momentum sums, and other singular configurations. Let χ_σ be smooth partition weights satisfying $\sum_\sigma \chi_\sigma = 1$. On each region, a coordinate transformation Φ_σ maps the unit cube $(0,1)^{D_\sigma}$ onto the corresponding integration domain $\mathcal{D}_{B,\sigma}$. The transformed integrand is

$$f_\sigma^{(0)}(x) = \chi_\sigma(\Phi_\sigma(x)) A_B(\Phi_\sigma(x)) \left|\det D\Phi_\sigma(x)\right|. \tag{2.18}$$

The partition weights and Jacobians preserve the original integral. The coordinate maps place the relevant singular limits at the boundaries of the unit cube.

I next examine the behavior of the completed integrands at these boundaries. After reflecting coordinates when necessary, I place each singular endpoint at $x_j = 0$. The derivative analysis applies when the transformed integrand admits a finite endpoint representation of the form

$$f_\sigma^{(0)}(x) = \sum_{\nu=1}^{J_\sigma} \left[\prod_{j=1}^{D_\sigma} x_j^{a_{\sigma\nu j}} (\log x_j)^{m_{\sigma\nu j}} \right] g_{\sigma\nu}(x), \tag{2.19}$$

where

$$a_{\sigma\nu j} > -1, \qquad m_{\sigma\nu j} \in \mathbb{N}_0, \qquad g_{\sigma\nu} \in C^r([0,1]^{D_\sigma}). \tag{2.20}$$

The endpoint powers ensure integrability, but derivatives may still diverge. The exponents and the regularity of $g_{\sigma\nu}$ must be determined from the interaction kernels and initial covariance. The fixed-order perturbative expansion alone does not establish this representation.

I remove the endpoint loss of differentiability by choosing positive integers ρ_j and substituting

$$x_j = y_j^{\rho_j}. \tag{2.21}$$

Including the Jacobian changes each endpoint power to

$$b_{\sigma\nu j} = \rho_j(a_{\sigma\nu j} + 1) - 1. \tag{2.22}$$

Since $a_{\sigma\nu j} > -1$, I can choose ρ_j so that $b_{\sigma\nu j} > r$ for every term ν.

The effect is explicit in one dimension. For

$$h(x) = x^a (\log x)^m g(x), \qquad a > -1, \quad g \in C^r([0,1]), \tag{2.23}$$

the substitution $x = y^\rho$ gives

$$\widetilde{h}(y) = \rho^{m+1} y^{\rho(a+1)-1} (\log y)^m g(y^\rho). \tag{2.24}$$

Writing $b = \rho(a+1) - 1$ and $\eta = b - r > 0$, derivatives of the endpoint factor through order r contain powers $y^{b-j}(\log y)^{m'}$ with $j \le r$. These terms remain bounded and extend continuously to $y = 0$ because $b - j > 0$. The product and chain rules give

$$\begin{aligned} \|\widetilde{h}\|_{C^r([0,1])} &\le C_{r,m} \rho^{m+r+1} (1+b)^r \\ &\quad \times (1 + \eta^{-m}) \|g\|_{C^r([0,1])}. \end{aligned} \tag{2.25}$$

The constant $C_{r,m}$ depends only on r and m.

Applying the substitutions to every coordinate, the final transformed integrand becomes

$$f_\sigma(y) = f_\sigma^{(0)}(y_1^{\rho_1}, \ldots, y_{D_\sigma}^{\rho_{D_\sigma}}) \prod_{j=1}^{D_\sigma} \rho_j y_j^{\rho_j - 1}. \tag{2.26}$$

The preceding argument bounds its mixed derivatives through total order r. I write

$$\|f_\sigma\|_{W^r_\infty([0,1]^{D_\sigma})} \le M_\sigma. \tag{2.27}$$

The constant M_σ depends on the physical kernels, initial covariance, coordinate transformations, endpoint exponents, and momentum regulators. It must be established for each physical application and need not remain uniform as a regulator is removed. This bound controls the interpolation accuracy in Section 3, while the cost of evaluating the integrand reversibly enters the computational complexity separately. Appendix A provides the detailed endpoint estimates, while Appendix D examines the gravitational one-loop integrals.

3 Quantum integration of the remaining error

Section 2 reduces each fixed-order statistical coefficient to a finite sum of integrals. The interaction kernels and Gaussian covariance determine their integrands. When the required cancellations and coordinate transformations yield bounded derivatives, I apply the quantum integration method of Novak and Heinrich [33,34]. A classically integrated polynomial approximates each integrand with an error bounded by $O(Mh^r)$. Quantum amplitude estimation then calculates the integral of this smaller residual rather than estimating the full integrand directly.

Consider one real integrand

$$f : [0,1]^D \longrightarrow \mathbb{R}, \qquad I(f) = \int_{[0,1]^D} f(x)\,\mathrm{d}^D x. \tag{3.1}$$

Here D is the number of independent momentum and time variables after the reductions of Section 2. I take D and the integer $r \geq 2$ to be fixed, as required for the continuous local interpolation used below. The derivative analysis supplies

$$\|f\|_{W^r_\infty([0,1]^D)} \leq M. \tag{3.2}$$

Thus M bounds the function and its derivatives through order r. I first treat a real integrand. I integrate the real and imaginary parts separately for complex coefficients.

Divide the unit cube into cells of side length $h = 2^{-m}$, where m is a nonnegative integer. On this mesh I construct a continuous tensor-product interpolating polynomial $\Pi_h f$ of degree $(r-1)$ in each coordinate. Its coefficients are determined by the values of f at the interpolation nodes. Standard interpolation estimates give

$$\|f - \Pi_h f\|_\infty \leq c_{D,r} M h^r. \tag{3.3}$$

The constant $c_{D,r}$ depends on the dimension, interpolation degree, and choice of nodes.

Define the residual by

$$R_h(x) = f(x) - \Pi_h f(x), \qquad B_h = 2c_{D,r} M h^r. \tag{3.4}$$

The interpolation bound gives $|R_h(x)| \leq B_h/2$ throughout the cube. The factor of two keeps the subsequent controlled rotation away from probabilities zero and one. The integral separates exactly:

$$I(f) = I_h + \int_{[0,1]^D} R_h(x)\,\mathrm{d}^D x, \qquad I_h = \int_{[0,1]^D} \Pi_h f(x)\,\mathrm{d}^D x. \tag{3.5}$$

I evaluate I_h classically. Integration of each interpolation polynomial is elementary. Constructing the interpolant requires $O_{D,r}(h^{-D})$ evaluations of f. The remaining integral has an integrand bounded in absolute value by B_h, which decreases as h^r.

I estimate this remaining integral on a fine grid using a quantum circuit. Let q denote the number of binary digits used for each integration coordinate. The midpoint grid contains

$$N = 2^{qD} \tag{3.6}$$

points, with coordinates

$$x_j = \frac{k_j + 1/2}{2^q}, \qquad k_j = 0, \ldots, 2^q - 1, \qquad j = 1, \ldots, D. \tag{3.7}$$

The circuit uses qD qubits to represent the grid indices. Hadamard gates prepare their uniform superposition. Reversible arithmetic converts each index into its corresponding midpoint coordinate.

The circuit evaluates $f(x)$ and its local polynomial interpolation $\Pi_h f(x)$ coherently over the superposition of midpoint labels. It does not enumerate the 2^{qD} grid points individually. For each label, the interpolating polynomial of degree $r-1$ in every coordinate uses

$$\nu_{D,r} = r^D \tag{3.8}$$

local nodes. The circuit evaluates f reversibly at these nodes and combines their values with the interpolation weights. It therefore reconstructs the polynomial without retrieving precomputed values from quantum random-access memory.

I normalize the residual as

$$z_h(x) = \frac{R_h(x)}{B_h}, \qquad -1/2 \le z_h(x) \le 1/2. \tag{3.9}$$

The normalized value is stored in a binary register. A controlled rotation of an auxiliary qubit implements

$$|z\rangle|0\rangle_a \longmapsto |z\rangle \left[\sqrt{\frac{1-z}{2}}|0\rangle_a + \sqrt{\frac{1+z}{2}}|1\rangle_a \right]. \tag{3.10}$$

The probability of measuring the auxiliary qubit in state $|1\rangle_a$ is $(1+z)/2$. I then reverse the arithmetic operations and return the temporary registers to zero.

Averaging over the uniform superposition gives the probability

$$a_h = \frac{1}{2} + \frac{1}{2N} \sum_{x \in \mathcal{X}_q} \frac{R_h(x)}{B_h}, \tag{3.11}$$

where $\mathcal{X}_q$ denotes the midpoint grid. As the result,

$$B_h(2a_h - 1) = \frac{1}{N} \sum_{x \in \mathcal{X}_q} R_h(x). \tag{3.12}$$

The right-hand side is the midpoint approximation to the residual integral. Quantum amplitude estimation determines a_h from repeated coherent applications of the circuit and its inverse.

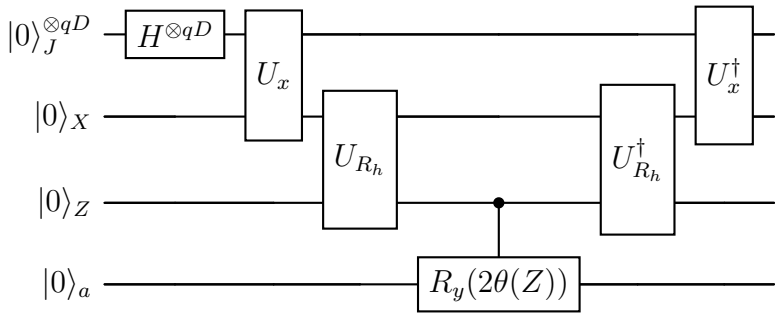


Figure 2: Quantum circuit for evaluating the residual integral. The index register J specifies a midpoint of the fine grid. The circuit U_x computes its coordinates. The circuit U_{R_h} evaluates f, reconstructs the local interpolation, and calculates $z_h = R_h/B_h$. The controlled rotation satisfies $\sin^2\theta(z) = (1+z)/2$. The subsequent inverse operations return the arithmetic registers to zero. Quantum amplitude estimation uses this circuit and its inverse to determine the probability a_h.

The quantum calculation has two principal integration errors. One comes from replacing the residual integral by its midpoint sum, and the other from estimating the probability a_h. Within each interpolation cell, the residual satisfies

$$\|\nabla R_h\|_\infty \le c'_{D,r} M h^{r-1}. \tag{3.13}$$

Since R_h is continuous across cell boundaries, this estimate also provides a global Lipschitz bound. The midpoint discretization error is therefore bounded by

$$\left| \int_{[0,1]^D} R_h(x)\, \mathrm{d}^D x - \frac{1}{N} \sum_{x \in \mathcal{X}_q} R_h(x) \right| \leq c_D c'_{D,r} M h^{r-1} 2^{-q}. \tag{3.14}$$

I choose the coordinate precision so that this error is at most a fixed fraction of the target accuracy ϵ. It is sufficient to take

$$2^{-q} \leq \frac{\epsilon}{8 c_D c'_{D,r} M h^{r-1}}. \tag{3.15}$$

Thus the grid resolution grows algebraically with inverse accuracy, while the required number of coordinate qubits grows logarithmically.

Now let $\widetilde{a}_h$ be the quantum estimate of a_h. Its contribution to the integration error is

$$|B_h(2\widetilde{a}_h - 1) - B_h(2a_h - 1)| = 2B_h|\widetilde{a}_h - a_h|. \tag{3.16}$$

To make this error $O(\epsilon)$, I require

$$|\widetilde{a}_h - a_h| = O\left(\frac{\epsilon}{B_h}\right). \tag{3.17}$$

Quantum amplitude estimation achieves an additive probability error δ_a with $O(\delta_a^{-1})$ applications of the state-preparation circuit and its inverse, at fixed success probability. The residual therefore requires

$$N_{\mathrm{res}} = O\left(\max\left\{1, \frac{B_h}{\epsilon}\right\}\right) \tag{3.18}$$

coherent circuit evaluations.

For $M/\epsilon \gg 1$, substituting $B_h = 2c_{D,r} M h^r$ gives

$$N_{\mathrm{res}} = O_{D,r}\left(\frac{M h^r}{\epsilon}\right). \tag{3.19}$$

Each residual state-preparation call evaluates f at one midpoint and at most r^D interpolation nodes. The total coherent function-evaluation count is therefore bounded by $(1 + r^D)N_{\mathrm{res}}$. Adding the classical evaluations used to construct the coarse approximation gives

$$N(h) = O_{D,r}\left(h^{-D} + (1 + r^D)\frac{M h^r}{\epsilon}\right). \tag{3.20}$$

The classical cost increases as the coarse mesh becomes finer, while the quantum cost decreases because the residual becomes smaller. For fixed D and r, balancing these contributions determines the optimal mesh

$$h \asymp \left(\frac{\epsilon}{M}\right)^{1/(D+r)}. \tag{3.21}$$

The resulting total number of function evaluations is

$$N(h) = O_{D,r}\left[\left(\frac{M}{\epsilon}\right)^{D/(D+r)}\right]. \tag{3.22}$$

This reproduces Eq. (1.5) for fixed D and r. The coherent interpolation overhead must be retained explicitly when comparing problems with different integration dimensions.

I now apply this construction to the integrals obtained from nonlinear evolution.

Theorem 2 (Quantum integration of a fixed-order coefficient)**.** *Let a fixed perturbative coefficient be expressed as a finite sum of integrals over regions labeled by σ. In each region, combine the terms required by the momentum cancellations and transform the integration domain to $[0,1]^{D_\sigma}$. Let the resulting integrand f_σ satisfy*

$$\|f_\sigma\|_{W_\infty^r} \leq M_\sigma, \tag{3.23}$$

with fixed D_σ and $r \geq 2$. Assume that a reversible circuit evaluates f_σ to prescribed absolute precision with gate cost $C_{\mathrm{eval},\sigma}(b)$ at b-bit precision. Then the coefficient can be estimated to additive error ϵ with fixed success probability using classical interpolation and quantum amplitude estimation.

For a fixed finite number of regions and positive error allocations ϵ_σ satisfying $\sum_\sigma \epsilon_\sigma \leq \epsilon$, the combined number of classical evaluations and coherent elementary evaluations of the sector integrands obeys

$$N_Q = O\left[\sum_\sigma \max\left\{1, \left(\frac{M_\sigma}{\epsilon_\sigma}\right)^{D_\sigma/(D_\sigma+r)}\right\}\right]. \tag{3.24}$$

The quantum circuit evaluates each transformed integrand and its local interpolation directly. It requires no quantum random-access memory.

The function-evaluation count and the gate count measure different resources. I now make their relation explicit.

Let $C_{\mathrm{eval}}(b)$ be the reversible gate cost of one integrand evaluation. One application of the residual state-preparation circuit evaluates $f(x)$ and at most $\nu_{D,r}$ interpolation values. It also computes the interpolation weights, performs the subtraction, normalizes the result by B_h, and implements the controlled rotation. Denote this complete circuit by $\mathcal{A}$. Its gate cost obeys

$$C_{\mathcal{A}} \leq (1+\nu_{D,r})C_{\mathrm{eval}}(b) + \mathrm{poly}\left(D, r, b, q, \log(1+B_{\mathrm{abs}})\right), \tag{3.25}$$

where B_{abs} bounds the magnitudes of the intermediate quantities in the chosen evaluation formula. The circuit uses qD qubits for the integration coordinates, together with the registers required for arithmetic and the auxiliary rotation.

The bound M controls derivatives of the complete integrand. The quantity B_{abs} controls the precision required while evaluating its constituent expressions. These bounds serve different purposes. Near a cancellation, individual terms may be much larger than their sum. I evaluate the combined expression with sufficient absolute precision to resolve the residual after subtraction. Finite-precision reversible arithmetic produces an approximation to the residual. Its evaluation error introduces a fixed bias in the integral, and repeated calls do not multiply this bias. Errors in approximate quantum gates, however, can accumulate across coherent calls. For the stable evaluation formulas considered here, the required arithmetic and gate-synthesis precision grows logarithmically with inverse accuracy, the intermediate arithmetic bounds, and the number of circuit calls. Appendix B establishes these bounds.

For sector σ, the quantum gate count consequently has the form

$$G_{\mathrm{quantum},\sigma} = O\left[N_{\mathrm{res},\sigma}\left((1+\nu_{D_\sigma,r})C_{\mathrm{eval},\sigma}(b_\sigma) + P_\sigma\right)\right], \tag{3.26}$$

where P_σ is the reversible-arithmetic overhead and $N_{\mathrm{res},\sigma}$ is the number of amplitude-estimation calls. The classical stage requires

$$O_{D_\sigma,r}(h_\sigma^{-D_\sigma}) \tag{3.27}$$

ordinary function evaluations. The construction of the perturbative integrands, their algebraic cancellations, and the derivation of their derivative bounds are additional classical operations. I retain these costs separately in the complete resource analysis.

Appendix B gives the detailed reversible implementation, precision bounds, and resource accounting. The next section applies the resulting integration algorithm to the gravitational interaction kernels of GGRW.

4 GGRW benchmark and random-wave comparison

4.1 GGRW Euler–Poisson hierarchy

I consider pressureless, self-gravitating matter in an Einstein–de Sitter universe. Let a denote the cosmological scale factor, $\delta(\mathbf{x},\tau)$ the density contrast, and $\mathbf{v}(\mathbf{x},\tau)$ the peculiar velocity. Here τ is conformal time and $\mathcal{H} = a^{-1}\mathrm{d}a/\mathrm{d}\tau$ is the conformal Hubble parameter. The continuity, Euler, and Poisson equations are

$$\partial_\tau \delta + \nabla\cdot[(1+\delta)\mathbf{v}] = 0, \tag{4.1}$$

$$\partial_\tau \mathbf{v} + \mathcal{H}\mathbf{v} + (\mathbf{v}\cdot\nabla)\mathbf{v} = -\nabla\phi, \tag{4.2}$$

$$\nabla^2\phi = \frac{3}{2}\mathcal{H}^2\delta. \tag{4.3}$$

I retain the irrotational growing solution. Its velocity field is determined by the divergence $\theta = \nabla\cdot\mathbf{v}$.

Introduce logarithmic scale-factor time $\eta = \log a$ and the Fourier doublet

$$\Psi_a(\mathbf{k},\eta) = \left(\delta(\mathbf{k},\eta), -\frac{\theta(\mathbf{k},\eta)}{\mathcal{H}}\right), \qquad a = 1,2. \tag{4.4}$$

The field index a labels density and velocity divergence. The evolution equations become

$$\partial_\eta \Psi_a(\mathbf{k}) + \sum_{b=1}^{2}\Omega_{ab}\Psi_b(\mathbf{k}) = \sum_{b,c=1}^{2}\int_{\mathbb{R}^3}\frac{\mathrm{d}^3q}{(2\pi)^3}\gamma_{abc}(\mathbf{k},\mathbf{q},\mathbf{k}-\mathbf{q})\Psi_b(\mathbf{q})\Psi_c(\mathbf{k}-\mathbf{q}), \qquad \Omega = \begin{pmatrix} 0 & -1 \\ -3/2 & 1/2 \end{pmatrix}. \tag{4.5}$$

The matrix Ω describes linear gravitational evolution. The vertices γ_{abc} describe the quadratic mode coupling. Their nonzero components are determined by

$$\alpha(\mathbf{p},\mathbf{q}) = \frac{(\mathbf{p}+\mathbf{q})\cdot\mathbf{p}}{p^2}, \qquad \beta(\mathbf{p},\mathbf{q}) = \frac{|\mathbf{p}+\mathbf{q}|^2(\mathbf{p}\cdot\mathbf{q})}{2p^2q^2}, \tag{4.6}$$

through

$$\gamma_{121}(\mathbf{k},\mathbf{p},\mathbf{q}) = \frac{1}{2}\alpha(\mathbf{p},\mathbf{q}), \tag{4.7}$$

$$\gamma_{112}(\mathbf{k},\mathbf{p},\mathbf{q}) = \frac{1}{2}\alpha(\mathbf{q},\mathbf{p}), \tag{4.8}$$

$$\gamma_{222}(\mathbf{k},\mathbf{p},\mathbf{q}) = \beta(\mathbf{p},\mathbf{q}), \qquad \mathbf{k} = \mathbf{p}+\mathbf{q}. \tag{4.9}$$

Equation (4.5) is therefore the quadratic system of Section 2, with two field components and three-dimensional momenta.

The eigenvalues of $-\Omega$ are 1 and $-3/2$. The growing linear solution is proportional to $e^\eta = a$. Consequently, the Einstein–de Sitter growth factor is

$$D_+(a) = a. \tag{4.10}$$

The linear matrix and interaction vertices are independent of η. On the regular growing branch, successive nonlinear corrections consequently separate into powers of D_+ and time-independent momentum kernels.

I write the density perturbation as

$$\delta(\mathbf{k}, a) = \sum_{r=1}^{\infty} D_+^r(a)\delta^{(r)}(\mathbf{k}). \tag{4.11}$$

The coefficient $\delta^{(r)}$ is of degree r in the primordial density field δ_0. Its Fourier representation is

$$\delta^{(r)}(\mathbf{k}) = \int \prod_{j=1}^{r} \frac{\mathrm{d}^3 q_j}{(2\pi)^3} (2\pi)^3 \delta^{(3)}\left(\mathbf{k} - \sum_{j=1}^{r} \mathbf{q}_j\right) \times F_r^{(s)}(\mathbf{q}_1, \ldots, \mathbf{q}_r) \prod_{j=1}^{r} \delta_0(\mathbf{q}_j). \tag{4.12}$$

Here $F_r^{(s)}$ is the GGRW density kernel symmetrized over its r incoming momenta. Substituting the lower-order solutions into Eq. (4.5) determines $F_r^{(s)}$ recursively. The time integrations of Section 2 reduce to algebraic coefficients because every growing solution carries a definite power of a.

The primordial density field is Gaussian, with

$$\langle \delta_0(\mathbf{k})\delta_0(\mathbf{k}')\rangle = (2\pi)^3 \delta^{(3)}(\mathbf{k} + \mathbf{k}')P_0(k). \tag{4.13}$$

The function $P_0(k)$ is the linear matter power spectrum at a reference epoch, with subsequent EdS growth factored out. For the physical benchmark, I use the linear total CDM–baryon spectrum within the single-pressureless-fluid approximation. The CDM-only spectrum of GGRW remains a comparison.

For the analysis below, I assume $P_0(k) = k^{n_s} A_{\mathrm{IR}}(k)$ near $k = 0$, where $A_{\mathrm{IR}} \in C^2$, and $P_0 \in C^2$ at nonzero finite momentum. At sufficiently large k, I require

$$\left|\frac{\mathrm{d}^j P_0(k)}{\mathrm{d}k^j}\right| \leq C_j k^{n_s - 4 - j}[1 + \log(k/k_*)]^2, \qquad j = 0, 1, 2, \tag{4.14}$$

where $k \geq k_* > 0$ and $-1 < n_s < 3$. These conditions specify the differentiated infrared and ultraviolet behavior required by the integration algorithm. They must be verified for the chosen linear matter spectrum.

I now apply Wick's theorem to products of the perturbative solutions. Each covariance contraction joins two initial fields and supplies one factor of P_0. The momentum delta functions leave integrals over independent internal momenta.

The relation to the general expansion of Section 2 is exact. A quadratic interaction vertex increases the number of initial fields by one. An n-point observable with K interaction vertices therefore contains $n + K$ initial fields. Wick's theorem pairs them into

$$I = \frac{n + K}{2} \tag{4.15}$$

covariance lines. For a connected contribution with L statistical loops, graph counting gives

$$I = n - 1 + L. \tag{4.16}$$

Consequently,

$$K = n - 2 + 2L. \tag{4.17}$$

Every initial field carries one power of D_+. The complete contribution therefore carries

$$D_+^{2(n-1+L)}. \tag{4.18}$$

Thus the number of external fields and statistical loops fixes both the nonlinear perturbative order and the cosmological growth factor. The remaining coefficient is a deterministic momentum integral.

I now examine the one-loop correction to the matter power spectrum. Its perturbative expansion is

$$P(k,a) = D_+^2(a)P_0(k) + D_+^4(a)\left[P_{22}(k) + P_{13}(k)\right] + O(D_+^6). \tag{4.19}$$

The one-loop contribution has two nonlinear interaction vertices and two primordial covariance lines. Its two terms are

$$P_{22}(k) = 2\int_{\mathbb{R}^3} \frac{\mathrm{d}^3q}{(2\pi)^3} \left|F_2^{(s)}(\mathbf{q}, \mathbf{k}-\mathbf{q})\right|^2 P_0(q)P_0(|\mathbf{k}-\mathbf{q}|), \tag{4.20}$$

$$P_{13}(k) = 6P_0(k)\int_{\mathbb{R}^3} \frac{\mathrm{d}^3q}{(2\pi)^3} F_3^{(s)}(\mathbf{k}, \mathbf{q}, -\mathbf{q})P_0(q). \tag{4.21}$$

The first term correlates two second-order density fields. The second correlates a first-order field with a third-order field. Their numerical coefficients count the corresponding Gaussian pairings.

The symmetrized GGRW kernels have an important large-momentum property. For fixed remaining momenta, a pair of large opposite momenta gives

$$F_r^{(s)}(\mathbf{k}_1, \ldots, \mathbf{k}_{r-2}, \mathbf{p}, -\mathbf{p}) = O(p^{-2}), \qquad p \longrightarrow \infty. \tag{4.22}$$

GGRW established this decoupling through explicit calculations for $r = 3, 4, 5, 6$. The suppression emerges after symmetrization. It expresses the weak influence of a short-wavelength opposite-momentum pair on a fixed long-wavelength density perturbation.

The second-order kernel is

$$F_2^{(s)}(\mathbf{p}, \mathbf{q}) = \frac{5}{7} + \frac{1}{2}\frac{\mathbf{p}\cdot\mathbf{q}}{pq}\left(\frac{p}{q} + \frac{q}{p}\right) + \frac{2}{7}\frac{(\mathbf{p}\cdot\mathbf{q})^2}{p^2q^2}. \tag{4.23}$$

For fixed nonzero $\mathbf{k}$, write $\mathbf{q} = \rho\mathbf{n}$, with $\rho = |\mathbf{q}|$ and $|\mathbf{n}| = 1$. Near $\rho = 0$,

$$F_2^{(s)}(\rho\mathbf{n}, \mathbf{k} - \rho\mathbf{n}) = \frac{\mathbf{k}\cdot\mathbf{n}}{2\rho} + O(1). \tag{4.24}$$

Using $P_0(\rho) = \rho^{n_s}A_{\mathrm{IR}}(\rho)$ and including the radial measure, the integrand takes the form

$$\rho^{n_s}H(\rho, \mathbf{n})\,\mathrm{d}\rho\,\mathrm{d}\Omega_2, \tag{4.25}$$

where H has bounded derivatives through order two in the radial and regular angular coordinates. The substitution $\rho = y^s$, with $s(n_s+1) - 1 > 2$, gives two bounded derivatives at $y = 0$. The same argument applies near $\mathbf{k} - \mathbf{q} = \mathbf{0}$.

At large ρ, the two incoming momenta nearly cancel. The explicit symmetrized kernel gives

$$F_2^{(s)}(\mathbf{q}, \mathbf{k}-\mathbf{q}) = \frac{k^2}{14\rho^2}(3 - 10\mu^2) + O(\rho^{-3}), \qquad \mu = \frac{\mathbf{k}\cdot\mathbf{n}}{k}. \tag{4.26}$$

The ultraviolet spectrum then gives the radial integrand, including its measure, the bound

$$O\left(\rho^{2n_s-10}[1 + \log\rho]^4\right). \tag{4.27}$$

Under $x = 1/\rho$, including the Jacobian, the endpoint has the bound

$$O\left(x^{8-2n_s}[1 + |\log x|]^4\right). \tag{4.28}$$

The differentiated spectrum and kernel bounds give corresponding estimates for the first two derivatives. Since $n_s < 3$, these derivatives remain bounded at $x = 0$. Finite regular angular charts provide uniform angular bounds.

The soft and hard regions therefore yield the required two bounded derivatives. Appendix D gives the complete regional analysis.

The P_{13} integral provides a second, more explicit test. Angular integration reduces it to a single radial integral [38],

$$P_{13}(k) = \frac{k^3 P_0(k)}{252(4\pi^2)} \int_0^\infty \mathrm{d}r\, P_0(kr)\mathcal{K}_{13}(r), \tag{4.29}$$

where $r = q/k$ and

$$\begin{aligned}\mathcal{K}_{13}(r) = \frac{12}{r^2} - 158 + 100r^2 - 42r^4 \\ + \frac{3}{r^3}(r^2-1)^3(7r^2+2)\log\left|\frac{1+r}{1-r}\right|.\end{aligned} \tag{4.30}$$

The rational and logarithmic terms in this expression must be combined before their endpoint behavior is evaluated.

At small r, their leading powers cancel. Direct expansion of the complete function gives

$$\mathcal{K}_{13}(r) = -168 + \frac{928}{5}r^2 + O(r^4), \qquad r \longrightarrow 0. \tag{4.31}$$

The apparent r^{-2} divergence has disappeared. Since $P_0(kr) = O(r^{n_s})$ with $n_s > -1$, the radial integrand is integrable at the origin.

The logarithm in Eq. (4.30) also appears singular at $r = 1$. Set $r = 1 + h$. The complete expansion is

$$\mathcal{K}_{13}(1+h) = -88 + 8h - 116h^2 + 216h^3\left[\log 2 - 1 - \log|h|\right] + O\left(h^4|\log|h||\right). \tag{4.32}$$

The logarithm begins at cubic order. Its first two derivatives remain finite at $h = 0$. The full radial kernel is therefore twice continuously differentiable across this point. The apparent logarithmic singularity belongs to an individual term, while the complete interaction kernel is regular to the order required for the integration algorithm.

At large r, the polynomial terms again cancel:

$$\mathcal{K}_{13}(r) = -\frac{488}{5} + \frac{96}{5r^2} + O(r^{-4}), \qquad r \longrightarrow \infty. \tag{4.33}$$

The ultraviolet spectrum gives $P_0(kr) = O(r^{n_s-4}[1+\log r]^2)$, so the radial integral converges for $n_s < 3$.

To establish bounded derivatives after compactification, set $x = 1/r$. Including the Jacobian, the transformed integrand is

$$f_{\mathrm{UV}}(x) = x^{-2}P_0(k/x)\mathcal{K}_{13}(1/x). \tag{4.34}$$

The differentiated spectrum bounds and the large-r expansion of $\mathcal{K}_{13}$ give

$$\left|\frac{\mathrm{d}^j f_{\mathrm{UV}}}{\mathrm{d}x^j}\right| \le C_j x^{2-n_s-j}[1+|\log x|]^2, \qquad j = 0, 1, 2. \tag{4.35}$$

I choose a positive integer s satisfying $s(3-n_s)-1 > 2$ and set $x = y^s$. Including its Jacobian gives two bounded derivatives at $y = 0$.

At the soft endpoint I use $r = y^s$ with $s(n_s + 1) - 1 > 2$. The complete radial kernel is already twice continuously differentiable at $r = 1$, as shown by Eq. (4.32). Appendix D gives the corresponding regional bounds.

I have now obtained the input required by the quantum estimator. The one-loop coefficient is a finite sum of integrals. Their domains are mapped to unit cubes. Their transformed integrands have two bounded derivatives:

$$\|f_\sigma\|_{W^2_\infty} \le M_\sigma. \tag{4.36}$$

Each integrand is an explicit function of the primordial spectrum and the GGRW interaction kernels. Its value can be calculated reversibly at the requested momentum coordinates.

I apply Theorem 2 to these integrals. Keeping all three components of an internal loop momentum gives the conservative dimension bound $D \le 3$. With $r = 2$, Eq. (3.24) yields

$$N_Q^{\mathrm{1loop}} = O\left[\left(\frac{M_{\mathrm{1loop}}}{\epsilon}\right)^{3/5}\right], \tag{4.37}$$

for $M_{\mathrm{1loop}}/\epsilon$ in the asymptotic precision regime. Here M_{1loop} collects the derivative bounds and fixed coefficients of the finite integration regions. The count includes construction of the classical interpolation and quantum evaluation of its residual. The gate count additionally includes reversible evaluation of the spectrum, kernels, interpolation, and controlled rotations, as developed in Appendix B.

For an isotropic initial spectrum, rotational symmetry reduces P_{22} to two momentum coordinates, while P_{13} already has a one-dimensional radial representation. Under the established W^2_∞ bounds, their respective quantum integration exponents are 1/2 and 1/3. The 3/5 exponent above is a conservative bound for the unreduced three-dimensional representation. FAST-PT and FFTLog exploit further convolution and spectral structure in the same cosmological integrals [35,36]. The Sobolev quantum bound therefore establishes applicability of the algorithm, but does not by itself establish a computational advantage over these specialized classical methods.

The same construction applies to higher-point GGRW statistics. Let

$$\delta_R(\mathbf{x}, a) = \int_{\mathbb{R}^3} \frac{\mathrm{d}^3k}{(2\pi)^3} \exp\left(-\frac{k^2R^2}{4}\right) \mathrm{e}^{\mathrm{i}\mathbf{k}\cdot\mathbf{x}} \delta(\mathbf{k}, a) \tag{4.38}$$

be the density contrast smoothed over a Gaussian ball of radius R. The connected moment $\langle \delta_R^n \rangle_c$ is obtained by attaching one Gaussian window to each external density field and summing the connected Wick contractions. At statistical loop order L, its growing-mode contribution has the form

$$\langle \delta_R^n(a) \rangle_c^{(L)} = D_+^{2(n-1+L)}(a)\, C_{n,L}(R), \tag{4.39}$$

where $C_{n,L}(R)$ is a finite sum of deterministic momentum integrals.

The benchmark is the regular growing solution before shell crossing. The Euler–Poisson equations supply the perturbative kernels on this branch. Their fixed-order statistical coefficients are the observables calculated here. Appendix D gives the detailed kernel calculations, the role of cosmic expansion, and the behavior of density and velocity fields near classical singularities.

4.2 Random-wave comparison

I next examine cubic nonlinear Schrödinger evolution with Gaussian random initial conditions. The nonlinear interactions introduce oscillatory phases whose resonance structure differs from

the momentum dependence of the GGRW gravitational kernels. Both systems involve cancellations among perturbative contributions, although their dominant mechanisms differ. I consider the equation

$$\mathrm{i}\partial_t\psi + \Delta\psi = \alpha|\psi|^2\psi, \tag{4.40}$$

where α is the nonlinear coupling. I take independent centered complex Gaussian initial Fourier amplitudes on a periodic spatial domain, as specified in Appendix E. The coefficient $\psi_{\mathbf{k}}(t)$ denotes the mode with wave-vector $\mathbf{k}$.

The linear evolution contributes the phase $\exp(-\mathrm{i}|\mathbf{k}|^2 t)$. I remove it by defining the interaction-picture amplitude

$$a_{\mathbf{k}}(t) = \exp(\mathrm{i}|\mathbf{k}|^2 t)\psi_{\mathbf{k}}(t). \tag{4.41}$$

The nonlinear equation becomes

$$\partial_t a_{\mathbf{k}} = -\mathrm{i}\alpha \sum_{\mathbf{k}_1-\mathbf{k}_2+\mathbf{k}_3=\mathbf{k}} \exp(\mathrm{i}t\Omega) a_{\mathbf{k}_1}\overline{a}_{\mathbf{k}_2} a_{\mathbf{k}_3}, \tag{4.42}$$

where the Fourier normalization is absorbed into the coupling and

$$\Omega = |\mathbf{k}|^2 - |\mathbf{k}_1|^2 + |\mathbf{k}_2|^2 - |\mathbf{k}_3|^2. \tag{4.43}$$

The quantity Ω is the frequency mismatch between the outgoing wave and the three incoming waves. Momentum conservation fixes the corresponding relation among their wave-vectors.

I integrate the interaction-picture equation in time and substitute lower-order amplitudes recursively. Each cubic interaction contributes three incoming fields and one interaction-time integral. The statistical observable is the wave-action spectrum $n_T(\mathbf{k}) = \mathbb{E}|a_{\mathbf{k}}(T)|^2$. At fixed perturbative order, Wick's theorem contracts the initial Gaussian amplitudes into covariance factors, leaving deterministic momentum sums and ordered time integrals. Their behavior in the weak-coupling, large-box, and long-time limits underlies the derivation of wave kinetic theory.

The frequency mismatch introduces a new momentum structure. One interaction-time integration gives

$$\mathcal{R}_T(\Omega) = \int_0^T \mathrm{e}^{\mathrm{i}s\Omega}\,\mathrm{d}s = \frac{\mathrm{e}^{\mathrm{i}T\Omega}-1}{\mathrm{i}\Omega}, \qquad \mathcal{R}_T(0) = T. \tag{4.44}$$

The apparent denominator singularity at $\Omega = 0$ cancels against the numerator. The integral representation gives

$$|\mathcal{R}_T(\Omega)| \le T, \qquad \left|\frac{\mathrm{d}^j\mathcal{R}_T}{\mathrm{d}\Omega^j}\right| \le \frac{T^{j+1}}{j+1}. \tag{4.45}$$

At fixed T, the resonance factor and all its derivatives with respect to Ω are bounded. I use its Taylor expansion near $\Omega = 0$ for stable numerical evaluation. These bounds do not by themselves control derivatives with respect to the independent integration momenta, since Ω depends quadratically on those momenta. The required Sobolev estimates must include the complete Gaussian-contracted integrand and the initial wave-action spectrum. Moreover, the derivative bounds grow as T^{j+1} and are not uniform on kinetic time scales.

At higher perturbative orders, additional cancellations arise between distinct diagrams. Individual paired diagrams can have large absolute values even when their signed sum is small. Deng and Hani identify families of such diagrams and organize their cancellation in the analysis of wave kinetic evolution [37, 39]. Their higher-moment analysis extends the construction to the wave kinetic hierarchy and propagation of chaos [40].

The two theories do not differ simply by whether cancellations occur between diagrams. In GGRW, symmetrization suppresses the coupling of large nearly opposite momenta to a long-wavelength density perturbation. The equal-time power spectrum also exhibits leading infrared

cancellations between P_{22} and P_{13}. The cubic NLS interaction has no analogous inverse-square hard-pair suppression. Its kinetic-limit analysis instead requires cancellations among families of paired diagrams with distinct oscillatory phases, time integrals, and combinatorial weights.

At fixed Fourier cutoff, Wick contraction gives finite momentum sums and interaction-time integrals. Appendix E derives these expressions and an elementary second-order cancellation from particle-number conservation. It does not establish the higher-order cancellations required on kinetic time scales. Applying the continuum quantum integration algorithm of Section 3 requires additional convergence and momentum derivative bounds for the completed expressions, together with their reversible evaluation costs. These bounds have not been established here for NLS. The explicit quantum integration estimate of Eq. (4.37) therefore remains specific to the one-loop GGRW calculation.

5 Outlook

The first extension is to higher orders in gravitational perturbation theory. At one loop, I determined the soft and hard momentum behavior directly from the GGRW kernels $F_2^{(s)}$ and $F_3^{(s)}$. At higher loops, several internal momenta may become large simultaneously. Individual momenta may also remain large while their partial sums approach zero. These overlapping limits probe the complete structure of the symmetrized kernels. GGRW established the suppression associated with one large opposite-momentum pair through sixth order. A general treatment requires derivative bounds for the complete higher-loop integrands, including cancellations between diagrams where necessary. For connected contributions through primordial degree eight, Proposition 15 gives the dimension bound $D \leq 12$, but does not establish the required Sobolev regularity in overlapping momentum limits. Establishing these bounds, together with diagram-construction and reversible-evaluation costs, would permit a quantum resource analysis at higher perturbative orders.

The next extension concerns short-distance effects beyond the pressureless single-stream description. The pressureless Euler–Poisson description follows a single-stream fluid. Gravitational evolution eventually produces shell crossing, multi-streaming, and velocity dispersion. Short-distance dynamics then feeds back into the evolution of long-wavelength density fluctuations. A complete statistical calculation must account for this feedback. The effective field theory of large-scale structure describes this feedback through effective stresses, counterterms, and stochastic contributions [41]. Deterministic effective interactions modify the perturbative kernels, while stochastic stresses require additional correlation functions beyond those specified by the primordial Gaussian covariance. The effective coefficients must also be matched to short-distance physics or supplied as input. I aim to incorporate these contributions into the fixed-order statistical calculation, including the costs of their statistical and effective-theory inputs.

This extension brings renormalization into the computational problem. Introduce a separation scale Λ between resolved long-wavelength modes and the short-distance dynamics represented by effective interactions. Loop integrals and effective coefficients depend separately on Λ. After matching the effective coefficients, their combined contribution to a physical observable must be independent of Λ up to terms beyond the retained perturbative accuracy. I will examine the cancellation of cutoff dependence, the momentum structure of the required counterterms, and the influence of finite smoothing windows.

Mass and momentum conservation constrain the allowed long-wavelength terms and suppress the response to certain short-scale configurations. Cutoff independence of the integrated observable does not by itself bound the derivatives or intermediate arithmetic magnitudes of its constituent expressions. I will examine whether the combined loop and counterterm con-

tributions admit controlled Sobolev and reversible-evaluation bounds as Λ varies within the effective theory's domain. This connects ultraviolet matching to the numerical complexity of renormalized observables.

A separate problem is the extension from individual perturbative coefficients to complete nonlinear statistics. At fixed order, the number of interaction diagrams is finite. As the order increases, the number of nonlinear trees and Gaussian pairings grows rapidly. Perturbative truncation introduces an additional error beyond numerical integration. I therefore seek bounds on the remainder of the expansion for specified observables and time intervals. The three-loop matter power spectrum exhibits asymptotic behavior at late times, even on scales where linear perturbations remain small [42]. The behavior of high-order coefficients will determine the usefulness of resummation and other reorganizations of the series. Recursive evaluation of diagram families, their symmetry relations, and their cancellations may reduce the cost of this calculation. The next objective is an error-controlled approximation in which perturbative truncation, diagram evaluation, ultraviolet matching, and numerical integration are treated within one complexity estimate.

Primordial non-Gaussianity introduces higher connected correlations in the initial density field. At fixed perturbative order, these correlations replace Gaussian pairings by the corresponding moment-cumulant partitions. The resulting expressions remain deterministic integrals. Their convergence and derivative bounds depend on the momentum structure of the initial cumulant kernels. This extension would permit calculation of fixed-order contributions to observables sensitive to primordial non-Gaussianity, provided the required initial cumulant spectra and their momentum regularity are specified. The same framework also accommodates more general cosmological expansion histories, for which the linear propagator and interaction kernels carry explicit time dependence.

These developments lead to the central computational question. The present algorithm establishes a quantum upper bound for fixed-order integrals with verified derivative bounds and efficient reversible evaluation. A complete complexity analysis must include the construction of interaction kernels, the number of diagrams, the cost of preserving their cancellations, the r^{D_σ} coherent interpolation overhead, and the arithmetic precision required to resolve small differences between large contributions. The resulting algorithm must be compared with classical methods that exploit the same analytic structure, including specialized quadrature, spectral integration, and convolution techniques. A genuine quantum advantage for a physical class of observables requires an asymptotic separation under a common input model. Establishing such a separation is a principal objective of the next stage.

Acknowledgment

I thank the participants in the Fields Institute's 2026 program "Quantum Algorithm for Differential Equations" (organized by Ala Shayeghi, David Fernandez, and Nathan Wiebe) for stimulating discussions. I am particularly grateful to Hari Krovi, Sofia Simon, and Yuan Su for useful exchanges. I acknowledge that this research was undertaken in part at, and financially supported by, the Institute for Pure & Applied Mathematics (IPAM, USA), the Simons Institute for the Theory of Computing (SIfTC, USA), and the Fields Institute for Research in Mathematical Sciences (FIRMS, Canada). This work was also supported by the National Research Foundation of Korea (NRF), Grant No. RS-2021-NR060112.

AI Statement

I used ChatGPT 5.6 to generate visualization of Figure 1.

A Deriving the integrals and bounding their derivatives

I derive the deterministic integral representation used in Sections 2 and 3. At fixed perturbative order, repeated substitution of the nonlinear evolution equation expresses the evolved fields as polynomials in their initial amplitudes. Gaussian averaging contracts these amplitudes into covariance functions and leaves momentum and time integrals. I combine the terms required by symmetry and conservation laws before establishing convergence and derivative bounds for the resulting integrands.

A.1 Perturbative expansion and Gaussian averaging

Consider m fields $u_a(\mathbf{x}, t)$ in d spatial dimensions, evolving on $\mathbb{R}^d$ or a periodic domain $\mathbb{T}^d$. I use continuum Fourier notation below. On a periodic domain, the momentum integrals become Fourier sums with the corresponding volume normalization. The evolution equation is

$$\begin{aligned}\partial_t \widehat{u}_a(\mathbf{k}, t) = &\sum_{b=1}^{m} L_{ab}(\mathbf{k}, t)\widehat{u}_b(\mathbf{k}, t) \\ &+ \sum_{q=2}^{p} g_q \sum_{b_1,\dots,b_q=1}^{m} \int \left[\prod_{j=1}^{q-1} \frac{\mathrm{d}^d k_j}{(2\pi)^d}\right] V^{(q)}_{a;b_1\cdots b_q}(\mathbf{k}_1, \dots, \mathbf{k}_q; t) \prod_{j=1}^{q} \widehat{u}_{b_j}(\mathbf{k}_j, t),\end{aligned} \tag{A.1}$$

where

$$\mathbf{k}_q = \mathbf{k} - \sum_{j=1}^{q-1} \mathbf{k}_j. \tag{A.2}$$

The matrix L_{ab} governs linear propagation and component mixing. The interaction kernel $V^{(q)}$ couples q incoming fields to one outgoing field, g_q is its coupling constant, and p is the maximal polynomial degree. Spatial derivatives become momentum factors, while constraints can introduce inverse momentum powers and projection operators. I retain these factors in the interaction kernels.

The linear propagator satisfies

$$\partial_t S(t, s; \mathbf{k}) = L(\mathbf{k}, t) S(t, s; \mathbf{k}), \qquad S(s, s; \mathbf{k}) = I. \tag{A.3}$$

Its matrix element $S_{ab}(t, s; \mathbf{k})$ propagates component b at time s into component a at time t. I prescribe random initial data,

$$u_a(\mathbf{x}, 0) = \xi_a(\mathbf{x}), \tag{A.4}$$

with a centered, translation-invariant Gaussian law μ_0. The Fourier covariance is

$$\mathbb{E}_{\mu_0}\left[\widehat{\xi}_a(\mathbf{k})\widehat{\xi}_b(\mathbf{k}')\right] = (2\pi)^d \delta^{(d)}(\mathbf{k} + \mathbf{k}') C_{ab}(\mathbf{k}). \tag{A.5}$$

For real fields, the covariance obeys $C_{ab}(\mathbf{k}) = C_{ba}(-\mathbf{k})$ and the corresponding positivity conditions. For complex fields, I include each field and its conjugate among the components entering the covariance matrix. Wick's theorem then determines all higher initial moments from C_{ab}.

I express the observable as a product of n linear measurements of the evolved fields,

$$\mathcal{O}[u(T)] = \prod_{j=1}^{n} \left[\sum_{a=1}^{m} \int \frac{\mathrm{d}^d k}{(2\pi)^d} w_{j,a}(\mathbf{k}) \widehat{u}_a(\mathbf{k}, T)\right]. \tag{A.6}$$

The weights $w_{j,a}$ select field components and momentum windows. Their choices determine smoothed moments, Fourier correlations, and projected observables. Connected correlations follow from combinations of the corresponding moments.

I multiply the nonlinear part of Eq. (A.1) by a formal parameter z while retaining the physical couplings g_q. I then expand

$$\widehat{u}(\mathbf{k},t;z)=\sum_{r=0}^{\infty}z^r\widehat{u}^{[r]}(\mathbf{k},t). \tag{A.7}$$

The coefficient $\widehat{u}^{[r]}$ contains exactly r nonlinear interaction vertices. The zeroth-order field is

$$\widehat{u}_a^{[0]}(\mathbf{k},t)=\sum_{b=1}^{m}S_{ab}(t,0;\mathbf{k})\widehat{\xi}_b(\mathbf{k}). \tag{A.8}$$

For a quadratic interaction, iterating Duhamel's formula gives

$$\begin{aligned}\widehat{u}_a^{[r]}(\mathbf{k},t)=g_2\int_0^t\mathrm{d}s\sum_{a'=1}^{m}S_{aa'}(t,s;\mathbf{k})\sum_{\substack{r_1,r_2\geq0\\r_1+r_2=r-1}}\sum_{b,c=1}^{m}\\ \times\int\frac{\mathrm{d}^dq}{(2\pi)^d}V^{(2)}_{a';bc}(\mathbf{q},\mathbf{k}-\mathbf{q};s)\\ \times\widehat{u}_b^{[r_1]}(\mathbf{q},s)\widehat{u}_c^{[r_2]}(\mathbf{k}-\mathbf{q},s),\qquad r\geq1.\end{aligned} \tag{A.9}$$

The time s locates the last interaction before observation at t. The incoming fields contain r_1 and r_2 earlier vertices, whose orders sum to $r-1$. For a vertex of degree q, the corresponding condition is

$$r_1+\cdots+r_q=r-1. \tag{A.10}$$

Repeated substitution thus produces rooted interaction trees with internal vertex degrees between two and p.

The order-K coefficient of the requested statistic is

$$Q_K(T)=[z^K]\,\mathbb{E}_{\mu_0}\left[\mathcal{O}[u(T;z)]\right]. \tag{A.11}$$

Here $[z^K]$ extracts the coefficient of z^K. The integer K counts the total interaction vertices distributed among the n measured fields, with the physical couplings included in Q_K. Each contribution contains n rooted trees. An interaction vertex contributes its kernel and time integral, an internal line contributes a propagator, and each leaf carries an initial Fourier amplitude. For quadratic evolution, a tree with r vertices has $r+1$ leaves. An order-K contribution to an n-point observable therefore contains $K+n$ initial amplitudes. For interactions of degree at most p, the number of leaves satisfies

$$N_{\mathrm{leaf}}\leq n+K(p-1). \tag{A.12}$$

I average these amplitudes using Wick's theorem. For $2s$ centered Gaussian Fourier amplitudes,

$$\mathbb{E}_{\mu_0}\left[\prod_{j=1}^{2s}\widehat{\xi}_{a_j}(\mathbf{k}_j)\right]=\sum_{\mathcal{P}}\prod_{(i,j)\in\mathcal{P}}\mathbb{E}_{\mu_0}\left[\widehat{\xi}_{a_i}(\mathbf{k}_i)\widehat{\xi}_{a_j}(\mathbf{k}_j)\right], \tag{A.13}$$

where $\mathcal{P}$ runs over all pairings. Odd centered Gaussian moments vanish. Every pairing introduces a covariance factor and a momentum-conserving delta function. The interaction vertices impose additional momentum constraints. After eliminating the dependent momenta, each fully contracted diagram G contributes

$$I_G=\int_{\mathcal{D}_G}A_G(\mathbf{q},\mathbf{t})\,\mathrm{d}^{D_{q,G}}q\,\mathrm{d}^{D_{t,G}}t. \tag{A.14}$$

The variables $\mathbf{q}$ collect the independent momentum coordinates and $\mathbf{t}$ the remaining interaction times. Their dimensions are $D_{q,G}$ and $D_{t,G}$.

The diagram amplitude combines the covariance, vertex, propagator, and observable factors as

$$A_G = \mathrm{Contr}\left[\left(\prod_{e\in E_C(G)} C_e\right)\left(\prod_{v\in V(G)} g_{q_v} V_v\right)\left(\prod_{\ell\in E_S(G)} S_\ell\right)\left(\prod_{j=1}^{n} w_j\right)\right]. \tag{A.15}$$

The operation Contr sums internal component indices. The sets $E_C(G)$, $V(G)$, and $E_S(G)$ contain covariance lines, interaction vertices, and propagator lines. The complete coefficient also includes the combinatorial weights and signs.

Interaction times retain their ordering along each tree branch. For a branch with s successive vertices,

$$0 < t_s < \cdots < t_1 < T. \tag{A.16}$$

Translation-invariant Fourier correlations contain an overall momentum delta function. I remove this distributional factor when defining reduced correlations. For smoothed observables, the external momenta are instead integrated against the prescribed windows.

Proposition 3 (Reduction to integrals at fixed order)**.** *Fix the spatial dimension d, field number m, maximal interaction degree p, observable degree n, and perturbative order K. Introduce finite momentum regulators and a finite observation time T. Assume that the regularized initial-value problem admits the perturbative construction above.*

Then $Q_K(T)$ is a finite linear combination of deterministic momentum and time integrals of the form (A.14)*. On a finite periodic domain with a Fourier cutoff, these expressions contain finite momentum sums and time integrals.*

The number of independent integration coordinates is bounded in terms of d, p, n, and K, independently of the number of spatial grid points or Fourier modes. The integral values and their evaluation costs can depend on the regulators and physical input.

Proof. An order-K contribution contains K interaction vertices distributed among n observable roots. Since every vertex has at most p incoming branches, the number of leaves is at most $n + K(p-1)$. There are finitely many corresponding tree tuples and Gaussian pairings.

Wick contraction introduces covariance factors and momentum constraints. Momentum conservation at the vertices supplies further linear constraints. Before eliminating them, the number of momentum coordinates is at most $d[n + K(p-1)]$, while the number of interaction times is K. Hence

$$D_G \le d[n + K(p-1)] + K. \tag{A.17}$$

Eliminating dependent momenta can only reduce this dimension. Increasing the Fourier cutoff enlarges the summation range or integration domain without changing the number of coordinates. □

The graph count enters the preprocessing cost. For quadratic dynamics, the number of ordered binary trees with r vertices is the Catalan number

$$C_r = \frac{1}{r+1}\binom{2r}{r}, \qquad C_r \sim \frac{4^r}{\sqrt{\pi}\, r^{3/2}}. \tag{A.18}$$

Distributing K vertices among n roots gives $\binom{K+n-1}{n-1}$ assignments of vertex counts. Since $C_r \le 4^r$, the number of tree tuples obeys

$$N_{\mathrm{tree}}(K,n) \le 4^K \binom{K+n-1}{n-1}. \tag{A.19}$$

For quadratic evolution with even $K+n$, Wick's theorem generates at most $(K+n-1)!!$ pairings. The number of raw graph topologies therefore satisfies

$$N_{\text{graph}}(K,n) \le 4^K \binom{K+n-1}{n-1} (K+n-1)!!. \tag{A.20}$$

For quadratic evolution with odd $K+n$, the Gaussian expectation vanishes. For higher-degree interactions, Wick's parity condition depends on the actual number of initial fields rather than $K+n$. Component summations and arithmetic operations add further costs to this topology count.

I generate the trees, perform Gaussian contractions, eliminate dependent momenta, and simplify the resulting integrands classically. I denote this cost by

$$C_{\text{pre}}(K,n;\mathcal{I},b), \tag{A.21}$$

where $\mathcal{I}$ specifies the interaction kernels, covariance data, and regulators, while b denotes the arithmetic precision.

Before estimating the momentum integrals, I identify cancellations among diagram contributions. When these cancellations are required for convergence, controlled derivatives, or stable evaluation, I express the affected terms on a common integration domain. Separately controlled contributions may remain separate, particularly when they admit lower-dimensional integrals. The relevant cancellations can arise from permutation symmetry, transverse projection, parity, or complete time integrations of oscillatory interactions. For a family B of diagrams combined in this manner, including the required changes of variables and Jacobians, I form

$$A_B(\mathbf{q},\mathbf{t}) = \sum_{G\in B} c_G A_G(\mathbf{q},\mathbf{t}), \tag{A.22}$$

where c_G contains their combinatorial weights and signs. Each family includes the terms needed for the cancellation identities used in its momentum bounds. Individual terms can diverge or possess large asymptotic contributions even when A_B remains finite. Taking absolute values before combining these terms can destroy this suppression. I preserve the cancellations in numerical evaluation through algebraic simplification or local expansions where direct subtraction would lose precision. The construction and simplification of these diagram groups are included in C_{pre}.

A.2 Changes of variables and derivative bounds

I now establish the regularity required for quantum integration. The convergence and differentiability of the grouped amplitudes depend on their behavior near soft momenta, large momenta, vanishing partial momentum sums, and resonances. I divide each domain into finitely many regions adapted to these configurations and introduce maps

$$\Phi_\sigma : (0,1)^{D_\sigma} \longrightarrow \mathcal{D}_{B,\sigma}. \tag{A.23}$$

Where regions overlap, I use smooth weights χ_σ forming a partition of unity. The transformed integrand is

$$f_\sigma(x) = [\chi_\sigma A_B]\left(\Phi_\sigma(x)\right) \left|\det D\Phi_\sigma(x)\right|. \tag{A.24}$$

The sum of the sector integrals equals the original grouped integral.

Ordered time integrations admit an elementary transformation. For $0 < t_s < \cdots < t_1 < T$, set

$$t_1 = Ty_1, \qquad t_2 = t_1 y_2, \qquad \ldots, \qquad t_s = t_{s-1} y_s. \tag{A.25}$$

The variables y_j range independently over $(0,1)$, and the Jacobian is

$$\left|\frac{\partial(t_1,\dots,t_s)}{\partial(y_1,\dots,y_s)}\right| = T^s \prod_{j=1}^{s-1} y_j^{s-j}. \tag{A.26}$$

The time-ordering constraints become polynomial weights on a cube.

For momentum integrations, I use radial variables, angular charts, compactification, and local changes of coordinates to separate endpoint powers and logarithms from the remaining regular factors.

Definition 4 (Integrable endpoint representation)**.** A grouped integral has a resolved endpoint representation of order r if its domain admits a finite collection of coordinate regions of the form (A.23) and, in each region, the transformed integrand has the form

$$f_\sigma(x) = \sum_{\nu=1}^{J_\sigma} \left[\prod_{j=1}^{D_\sigma} x_j^{a_{\sigma\nu j}} (\log x_j)^{m_{\sigma\nu j}}\right] \times g_{\sigma\nu}(x). \tag{A.27}$$

Every exponent satisfies $a_{\sigma\nu j} > -1$, every $m_{\sigma\nu j}$ is a nonnegative integer, and each regular factor belongs to

$$g_{\sigma\nu} \in C^r([0,1]^{D_\sigma}) \tag{A.28}$$

with bounded derivatives through total order r.

The coordinate maps, endpoint exponents, regular factors, and their evaluation formulas are supplied as part of the representation.

The condition $a_{\sigma\nu j} > -1$ makes each power-logarithm factor integrable at $x_j = 0$. Since the regular factors are bounded, every term in Eq. (A.27) is absolutely integrable. Other boundary singularities must be brought to the same form by the local coordinates.

The representation is an analytical property of the completed physical integrand. It must be derived from the interaction kernels, propagators, covariance, and observable weights. In particular, an asymptotic bound on the value of an integrand does not imply the derivative bounds needed below. Sector decomposition can extract endpoint powers from suitable rational and algebraic integrals [43]. Transcendental factors and cancellation identities require corresponding analysis.

The endpoint representation controls regularity. Finite-precision evaluation additionally requires a formula that preserves the cancellations.

Definition 5 (Stable evaluation of a cancelling sum)**.** A transformed integrand admits stable evaluation if its complete expression can be written as

$$f_\sigma(x) = \sum_{a=1}^{J_\sigma} c_a \prod_{b=1}^{F_a} h_{ab}(x), \tag{A.29}$$

where the elementary factors and intermediate arithmetic operations admit certified absolute-error evaluation.

Every cancellation required to remove an apparent pole or a leading asymptotic contribution is represented algebraically or by a local expansion with a controlled remainder. The intermediate arithmetic magnitudes are bounded for the specified evaluation procedure.

I denote an upper bound on these intermediate magnitudes by $B_{\mathrm{abs},\sigma}$. It determines the arithmetic precision needed to evaluate the complete sum, whereas the derivative norm determines interpolation accuracy. A small final value can require high precision if it results from cancellation between large intermediate terms.

I next show how an integrable power-logarithm endpoint can be transformed into a function with bounded derivatives.

Lemma 6 (Bounded derivatives after a power substitution)**.** *Let*

$$h(x) = x^a(\log x)^m g(x), \qquad a > -1, \tag{A.30}$$

where m is a nonnegative integer and $g \in C^r([0,1])$. Choose a positive integer s such that

$$s(a+1) - 1 > r. \tag{A.31}$$

Under $x = y^s$, including the Jacobian, the transformed integrand is

$$\widetilde{h}(y) = s^{m+1} y^{s(a+1)-1} (\log y)^m g(y^s). \tag{A.32}$$

It extends to a function in $C^r([0,1])$.

Proof. Set $b = s(a+1) - 1$. Differentiating $y^b(\log y)^m$ ℓ times gives a finite sum of terms

$$y^{b-\ell}(\log y)^{m'}, \qquad 0 \le m' \le m. \tag{A.33}$$

For $\ell \le r$, the condition $b > r$ implies $b - \ell > 0$. Every such term therefore vanishes as $y \to 0$.

The composition $g(y^s)$ belongs to $C^r([0,1])$. Leibniz' rule then gives continuous extensions of all derivatives of $\widetilde{h}$ through order r. □

The substitution also gives a quantitative derivative bound.

Lemma 7 (Derivative bound after substitution)**.** *Under the assumptions of Lemma 6, set*

$$b = s(a+1) - 1, \qquad \delta = b - r > 0. \tag{A.34}$$

There is a constant $C_{r,m}$ depending only on r and m such that

$$\begin{aligned} \|\widetilde{h}\|_{C^r([0,1])} &\le C_{r,m} s^{m+r+1} (1+b)^r \\ &\quad \times (1 + \delta^{-m}) \|g\|_{C^r([0,1])}. \end{aligned} \tag{A.35}$$

For $m = 0$, the factor $1 + \delta^{-m}$ is absorbed into $C_{r,0}$.

Proof. For $\eta > 0$ and an integer $m' \ge 1$,

$$\sup_{0<y\le 1} y^\eta |\log y|^{m'} = \left(\frac{m'}{e\eta}\right)^{m'}. \tag{A.36}$$

For $m' = 0$, the supremum is one. After at most r derivatives of $y^b(\log y)^m$, the remaining power of y is at least $b - r = \delta$. The preceding identity bounds the logarithmic factors by a constant depending on m times $1 + \delta^{-m}$.

Differentiation of y^b contributes products of at most r factors, each bounded by $1 + b$. The chain rule also gives

$$\left\| \frac{\mathrm{d}^\ell}{\mathrm{d}y^\ell} g(y^s) \right\|_\infty \le C_r s^\ell \|g\|_{C^\ell([0,1])}, \qquad 0 \le \ell \le r. \tag{A.37}$$

Leibniz' rule, together with the prefactor s^{m+1}, yields Eq. (A.35). □

I apply the substitution coordinatewise to Eq. (A.27). For every sector σ and coordinate j, choose a positive integer $s_{\sigma j}$ satisfying

$$s_{\sigma j}(a_{\sigma\nu j}+1)-1>r \qquad \text{for every } \nu, \tag{A.38}$$

and set

$$x_j = y_j^{s_{\sigma j}}. \tag{A.39}$$

Since the number of endpoint terms is finite, one exponent $s_{\sigma j}$ can satisfy all of them. The Jacobian is

$$\prod_{j=1}^{D_\sigma} s_{\sigma j} y_j^{s_{\sigma j}-1}. \tag{A.40}$$

The regular factors become

$$g_{\sigma\nu}\left(y_1^{s_{\sigma 1}},\dots,y_{D_\sigma}^{s_{\sigma D_\sigma}}\right). \tag{A.41}$$

The multivariable chain rule bounds their derivatives through total order r. Combining these bounds with the one-dimensional endpoint estimates gives the following result.

Corollary 8 (Sobolev bound for the transformed integrals)**.** *Suppose a grouped integral has a finite resolved endpoint representation of order r in the sense of Definition 4. Apply coordinatewise power substitutions satisfying the preceding inequalities for every endpoint term.*

Then the fully transformed integrand belongs to

$$W_\infty^r([0,1]^{D_\sigma}) \tag{A.42}$$

and admits a finite bound

$$\|f_\sigma\|_{W_\infty^r} \le M_\sigma. \tag{A.43}$$

Here f_σ denotes the integrand after all substitutions have been incorporated into the coordinate map. The same function belongs to W_p^r for every finite $p \ge 1$.

The constant M_σ includes the derivatives of the regular factors, endpoint powers, logarithms, power substitutions, and Jacobians. Increasing a smoothing exponent can improve endpoint regularity while increasing this constant. I retain its actual value in the integration cost.

The construction of an endpoint representation requires analysis of the physical integrand. Once the representation and stable evaluation formula are supplied, their derivative and arithmetic bounds can be verified numerically.

Proposition 9 (Verification of a resolved integral)**.** *Fix perturbative order K, observable degree n, and derivative order r. Consider an integration region with the endpoint representation of Definition 4 and the stable evaluation formula of Definition 5.*

Assume the regular factors and their derivatives through order r admit effective validated interval enclosures on the closed cube. Assume the evaluation formula has certified denominator bounds, branch domains, and local representations at its removable singularities.

Then validated interval calculations, together with Lemma 7, produce finite bounds

$$M_\sigma \ge \|f_\sigma\|_{W_\infty^r} \tag{A.44}$$

and $B_{\mathrm{abs},\sigma}$ on intermediate arithmetic magnitudes.

I denote the verification cost by $C_{\mathrm{cert}}(K,n,r;\mathcal{I},b)$, where b is the working precision.

Proof. Differentiate the supplied regular representation through order r. Lemma 7 bounds the explicit endpoint factors, while the assumed interval enclosures bound the regular factors and their derivatives.

The certified denominator and branch conditions keep the arithmetic operations within their domains. At removable singularities, use the supplied regular expansions with controlled remainders. Combine the resulting bounds by interval arithmetic with outward rounding. A finite subdivision of the compact regular domain, when needed, gives enclosures for every derivative and intermediate quantity. Their upper bounds yield M_σ and $B_{\mathrm{abs},\sigma}$. □

The proposition verifies a supplied representation. Its hypotheses require the cancellation identities, coordinate maps, regular factors, and derivative enclosures to have been established for the selected integrand. They do not assert an automatic construction for arbitrary nonlinear PDEs.

For quantum evaluation, I represent each real transformed integrand by a reversible circuit

$$U_{f_\sigma} : |x\rangle|0\rangle \longmapsto |x\rangle|\widetilde{f}_\sigma(x)\rangle, \tag{A.45}$$

where $\widetilde{f}_\sigma(x)$ approximates $f_\sigma(x)$ to a prescribed absolute error. Complex integrands are evaluated through their real and imaginary components.

The circuit computes the coordinate transformations and Jacobians, evaluates the propagators, covariance factors, interaction kernels, and observable windows, and assembles the completed diagram sums. Reversible arithmetic produces the output and uncomputes its temporary registers. I denote the gate cost of one evaluation at precision b by

$$C_{\mathrm{eval},\sigma}(b). \tag{A.46}$$

The Sobolev constant M_σ controls the interpolation error, while $B_{\mathrm{abs},\sigma}$ controls the arithmetic range needed for accurate evaluation of the completed integrand. I therefore retain $C_{\mathrm{pre}}(K, n; \mathcal{I}, b)$, $C_{\mathrm{cert}}(K, n, r; \mathcal{I}, b)$, and $C_{\mathrm{eval},\sigma}(b)$ as distinct resources. Appendix B derives the quantum integration cost from these data.

B Quantum circuit and its cost

I construct the quantum integration circuit for the deterministic integrals derived in Appendix A. At fixed perturbative order, the interaction diagrams and Gaussian contractions give finitely many integrals. I assume that the required cancellations have been performed and that the transformed integrands have certified derivative bounds. These bounds determine the integration rate, while the explicit integrand formulas determine its gate and arithmetic costs.

B.1 Classical interpolation and quantum estimation of its residual

Consider

$$I_D(f) = \int_{[0,1]^D} f(x)\, \mathrm{d}^D x, \tag{B.1}$$

where D is the integration dimension. I take f to be real-valued. Complex integrals are evaluated through their real and imaginary parts.

For $f \in W_p^r([0,1]^D)$ with $r/D > 1/p$, point evaluation is continuous. A suitable classical quadrature rule J_ℓ at resolution $2^{-\ell}$ satisfies

$$|I_D(f) - J_\ell f| \le C_{D,r,p} 2^{-r\ell} \|f\|_{W_p^r}. \tag{B.2}$$

Quantum integration improves the estimation of the successive quadrature corrections by quantum summation. The construction and its query bounds were developed by Novak and Heinrich [33, 34, 44]. For $2 < p < \infty$ and $r/D > 1/p$, the optimal worst-case quantum query error is [34]

$$e_n^{\mathrm{q}}\left(I_D, B(W_p^r)\right) = \Theta\left(n^{-r/D-1}\right). \tag{B.3}$$

Here $B(W_p^r)$ denotes the unit Sobolev ball, and e_n^{q} is the smallest worst-case error achievable with n quantum function queries and fixed success probability. The upper and lower bounds have the same exponent for this function class.

Proposition 10 (Quantum integration with bounded Sobolev norm)**.** *Let $f \in W_p^r([0,1]^D)$, where $2 < p < \infty$ and $r/D > 1/p$. If*

$$\|f\|_{W_p^r} \le M, \tag{B.4}$$

then $I_D(f)$ can be estimated to additive error ϵ, with fixed success probability, using

$$N_{\mathrm{q}} = O_{D,r,p}\left[\max\left\{1, \left(\frac{M}{\epsilon}\right)^{D/(D+r)}\right\}\right] \tag{B.5}$$

quantum function queries.

Proof. For $M > 0$, apply the upper bound in Eq. (B.3) to f/M, with target error ϵ/M. Solving $n^{-1-r/D} = O(\epsilon/M)$ gives the stated query count. If $M \le \epsilon$, the zero estimate meets the requested absolute accuracy. □

The proposition treats function evaluation as a query. For the PDE integrals, that query must be implemented from their interaction kernels, covariance factors, propagators, and coordinate maps. I give an explicit construction for the stronger regularity class

$$f : [0,1]^D \longrightarrow \mathbb{R}, \qquad \|f\|_{W_\infty^r} \le M, \qquad r \ge 2. \tag{B.6}$$

Throughout the precision analysis, D and r are fixed. The case $M = 0$ is trivial, so I assume $M > 0$ below.

Divide the cube into cells of side length $h = 2^{-m}$. On each cell, construct the tensor-product nodal interpolant of degree $r-1$ in each coordinate, using consistent nodes on shared faces. The resulting interpolant $\Pi_h f$ is continuous and satisfies

$$\|f - \Pi_h f\|_\infty \le c_{D,r}^{(0)} M h^r \tag{B.7}$$

and, within each cell,

$$\|\nabla(f - \Pi_h f)\|_\infty \le c'_{D,r} M h^{r-1}. \tag{B.8}$$

Since the interpolant is continuous, the second estimate also gives a global Lipschitz bound by subdividing line segments at cell boundaries.

Define

$$R_h(x) = f(x) - \Pi_h f(x) \tag{B.9}$$

and choose

$$B_h = 2c_{D,r}^{(0)} M h^r. \tag{B.10}$$

The interpolation constant is taken positive. Then

$$|R_h(x)| \le \frac{B_h}{2}. \tag{B.11}$$

The integral separates exactly.

$$I_D(f) = I_h + I_D(R_h), \qquad I_h = \int_{[0,1]^D} \Pi_h f(x)\, \mathrm{d}^D x. \tag{B.12}$$

I calculate I_h classically by integrating the interpolation basis functions. The number of distinct nodal evaluations is

$$N_h = O_{D,r}(h^{-D}). \tag{B.13}$$

These values may be stored in ordinary classical memory.

The same interpolant gives the appropriate classical randomized comparison. For independent uniform points $U_1, \ldots, U_{N_s} \in [0,1]^D$, the estimator

$$\widehat{I}_{\mathrm{C}} = I_h + \frac{1}{N_s} \sum_{j=1}^{N_s} R_h(U_j) \tag{B.14}$$

is unbiased, with variance bounded by

$$\mathrm{Var}(\widehat{I}_{\mathrm{C}}) \le \frac{(c_{D,r}^{(0)} M h^r)^2}{N_s}. \tag{B.15}$$

The combined classical evaluation count at fixed success probability therefore obeys

$$N_{\mathrm{C,rand}}(h) = O_{D,r}\left[h^{-D} + \max\left\{ 1, \left(\frac{M h^r}{\epsilon} \right)^2 \right\} \right]. \tag{B.16}$$

Balancing the two terms gives

$$N_{\mathrm{C,rand}} = O_{D,r}\left[\left(\frac{M}{\epsilon} \right)^{2D/(D+2r)} \right] \qquad (M/\epsilon \gg 1). \tag{B.17}$$

This is the optimal randomized exponent for the bounded-derivative input class [33].

The quantum circuit reconstructs the local interpolant independently. It locates the cell containing x, evaluates f at its $\nu_{D,r} = r^D$ nodes, and combines the nodal values with the interpolation weights. Thus a coherent residual evaluation uses at most $1 + \nu_{D,r}$ evaluations of f and requires no quantum random-access memory.

I discretize the residual integral on a dyadic midpoint grid. With q bits per coordinate, let

$$\mathcal{X}_q = \left\{ \frac{j + 1/2}{2^q} \;\middle|\; j = 0, \ldots, 2^q - 1 \right\}^D. \tag{B.18}$$

The grid contains 2^{qD} points. A register of qD qubits represents their integer labels. Hadamard gates prepare

$$|\mathrm{unif}_q\rangle = 2^{-qD/2} \sum_{x \in \mathcal{X}_q} |x\rangle. \tag{B.19}$$

Reversible arithmetic converts each label into its midpoint coordinates.

Normalize the residual by

$$z_h(x) = \frac{R_h(x)}{B_h}, \qquad |z_h(x)| \le \frac{1}{2}. \tag{B.20}$$

After computing $z_h(x)$, a controlled rotation acts on an auxiliary qubit.

$$|z\rangle|0\rangle_a \longmapsto |z\rangle \left[\sqrt{\frac{1-z}{2}}|0\rangle_a + \sqrt{\frac{1+z}{2}}|1\rangle_a \right]. \tag{B.21}$$

The probability of obtaining $|1\rangle_a$ is $(1+z)/2$, between $1/4$ and $3/4$. I then uncompute the arithmetic registers, leaving the midpoint-label register entangled with the auxiliary qubit.

The good-state probability is

$$a_h = \frac{1}{2} + \frac{1}{2|\mathcal{X}_q|} \sum_{x \in \mathcal{X}_q} z_h(x). \tag{B.22}$$

It determines the residual midpoint mean.

$$\frac{1}{|\mathcal{X}_q|} \sum_{x \in \mathcal{X}_q} R_h(x) = B_h(2a_h - 1). \tag{B.23}$$

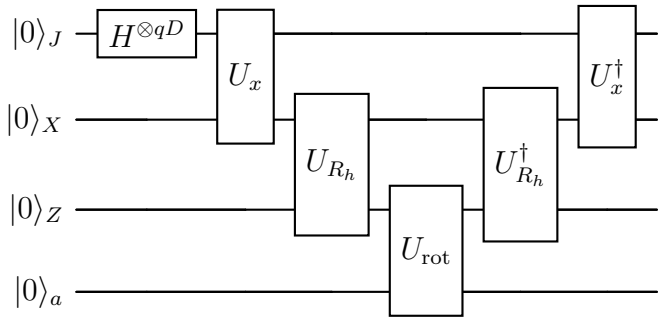


Figure 3: State preparation for the residual integral. The register J contains the midpoint labels. U_x computes the coordinates, U_{R_h} computes the normalized residual, and U_{rot} implements Eq. (B.21). The inverse arithmetic operations restore the work registers to zero.

Let $\mathcal{A}_{h,q}$ be the complete state-preparation unitary. Define

$$\begin{aligned} S_0 &= I - 2|0\cdots0\rangle\langle 0\cdots0|, \\ S_1 &= I - 2\left(I \otimes |1\rangle_a\langle 1|\right). \end{aligned} \tag{B.24}$$

The Grover iterate is

$$Q_h = -\mathcal{A}_{h,q} S_0 \mathcal{A}_{h,q}^\dagger S_1. \tag{B.25}$$

Amplitude estimation determines a_h from controlled applications of Q_h [45]. Powers through 2^{t-1} require

$$\sum_{j=0}^{t-1} 2^j = O(2^t) \tag{B.26}$$

Grover iterations. Iterative amplitude estimation avoids the inverse quantum Fourier transform, with an additional double-logarithmic factor in its proven query bound [46].

I first bound the midpoint discretization error. The Lipschitz estimate (B.8) gives

$$\left| I_D(R_h) - \frac{1}{|\mathcal{X}_q|} \sum_{x \in \mathcal{X}_q} R_h(x) \right| \quad \leq \quad c_D c'_{D,r} M h^{r-1} 2^{-q}. \tag{B.27}$$

To make this contribution at most $\epsilon/8$, it suffices to choose

$$2^{-q} \leq \frac{\epsilon}{8 c_D c'_{D,r} M h^{r-1}}. \tag{B.28}$$

For the mesh chosen below,

$$q = O_{D,r}\left[1 + \log\left(1 + \frac{M}{\epsilon}\right)\right]. \tag{B.29}$$

If amplitude estimation returns $\widetilde{a}_h$, the induced residual integration error is

$$2B_h|\widetilde{a}_h - a_h|. \tag{B.30}$$

I allocate a probability error

$$\delta_a = \Theta\left(\frac{\epsilon}{B_h}\right) \tag{B.31}$$

when B_h exceeds the residual error tolerance. Amplitude estimation then requires $O(B_h/\epsilon)$ state-preparation calls. When B_h is already below that tolerance, I omit the quantum residual stage. Thus

$$N_{\text{res}} = O\left[\max\left\{1, \frac{B_h}{\epsilon}\right\}\right]. \tag{B.32}$$

The corresponding coherent integrand-evaluation count satisfies

$$N_{f,\text{coh}}(h) \le (1 + r^D) N_{\text{res}}(h). \tag{B.33}$$

Combining classical interpolation with residual estimation gives

$$N_{\text{tot}}(h) = O_{D,r}\left[h^{-D} + (1 + r^D)\max\left\{1, \frac{Mh^r}{\epsilon}\right\}\right]. \tag{B.34}$$

For $M/\epsilon \gg 1$, balancing the two terms yields

$$h_* = \Theta_{D,r}\left[\left(\frac{\epsilon}{M}\right)^{1/(D+r)}\right]. \tag{B.35}$$

The nearest dyadic mesh changes only the constant. The resulting function-evaluation count is

$$N_{\text{tot}}(h_*) = O_{D,r}\left[\left(\frac{M}{\epsilon}\right)^{D/(D+r)}\right]. \tag{B.36}$$

This construction attains the quantum Sobolev integration exponent with an explicit residual evaluation circuit.

The interpolation decomposition is exact. The numerical error consists of classical evaluation error, midpoint discretization, residual evaluation error, amplitude-estimation error, and gate-implementation error. The last two must be distinguished from the bias introduced by finite-precision arithmetic.

A reversible arithmetic circuit computes a finite-precision function $\widetilde{f}(x)$. When its Boolean operations are implemented exactly, the resulting circuit is an exact unitary for that approximate function. Repeated amplitude-estimation calls do not accumulate new arithmetic bias. That bias is the difference between the exact and finite-precision integrands.

Suppose the computed residual satisfies

$$\sup_x |\widetilde{R}_h(x) - R_h(x)| \le \delta_R. \tag{B.37}$$

Its midpoint mean differs from the exact midpoint mean by at most δ_R. The choice

$$\delta_R \le \min\left\{\frac{\epsilon}{16}, \frac{B_h}{8}\right\} \tag{B.38}$$

controls the integration bias and keeps the normalized approximate residual inside a fixed interval contained in $(-1, 1)$. Amplitude estimation then estimates the probability defined by $\widetilde{R}_h$. The arithmetic bias enters the final error budget once.

Errors in approximate quantum gates behave differently because the same imperfect operation is applied repeatedly.

Lemma 11 (Accumulated coherent circuit error)**.** *Let T_{AE} be the total number of calls to $\mathcal{A}_{h,q}$ and $\mathcal{A}_{h,q}^{\dagger}$ during amplitude estimation. Suppose each implemented call differs from its specified unitary by operator norm at most η_{circ}.*

The total operator-norm error is bounded by

$$O(T_{\mathrm{AE}}\eta_{\mathrm{circ}}). \tag{B.39}$$

A sufficient choice for an accumulated error of order T_{AE}^{-1} is

$$\eta_{\mathrm{circ}} \leq cT_{\mathrm{AE}}^{-2}, \tag{B.40}$$

where c is a sufficiently small constant.

Proof. Replace the specified unitary calls by their implementations one at a time. The difference between consecutive circuits contains one unitary error conjugated by products of unitaries. Its operator norm is at most η_{circ}. The triangle inequality bounds the complete error by $T_{\mathrm{AE}}\eta_{\mathrm{circ}}$. Substituting Eq. (B.40) gives the stated result. □

For amplitude estimation with $T_{\mathrm{AE}} = O(\delta_a^{-1})$, the lemma gives a sufficient gate-implementation accuracy of order δ_a^2 per call. This precision is logarithmic in $1/\delta_a$ for standard gate synthesis. The reversible evaluation formula separately requires uniform absolute error $O(\epsilon)$, with the allocation adjusted for interpolation and normalization. The physical integrand may require more bits when its evaluation involves large intermediate quantities.

Theorem 12 (Query and gate cost for one smooth integral)**.** *Let $f : [0, 1]^D \to \mathbb{R}$ satisfy*

$$\|f\|_{W_\infty^r} \leq M, \qquad r \geq 2, \tag{B.41}$$

with fixed D and r. Assume a reversible circuit evaluates f to prescribed absolute precision with gate cost $C_{\mathrm{eval}}(b)$ at b-bit precision.

Then $I_D(f)$ can be estimated to additive error ϵ, with fixed success probability, using

$$N_{\mathrm{tot}} = O_{D,r}\left[\max\left\{1, \left(\frac{M}{\epsilon}\right)^{D/(D+r)}\right\}\right] \tag{B.42}$$

classical and quantum function evaluations.

Suppose the evaluation formula has certified bounds on its intermediate quantities and admits polynomial-cost reversible arithmetic. Let $B_{\mathrm{abs}} \geq 1$ bound these intermediate magnitudes. Then logarithmic arithmetic and gate-synthesis precision in the inverse accuracy, evaluation bounds, and formula size suffices.

Writing N_{q} for the number of quantum residual state-preparation calls, the gate count satisfies

$$\begin{aligned} G_{\mathrm{sector}} &= O_{D,r}\left[N_{\mathrm{q}}\left((1+\nu_{D,r})C_{\mathrm{eval}}(b) + P_{\mathrm{arith}}\right)\right], \\ P_{\mathrm{arith}} &= \mathrm{poly}\left(D, r, b, q, \log(1+N_{\mathrm{q}}), \log(1+B_{\mathrm{abs}})\right). \end{aligned} \tag{B.43}$$

The classical coarse-stage cost is counted separately. The circuit requires no quantum random-access memory.

Proof. Equations (B.7) and (B.13) give the interpolation error and classical evaluation count. The residual normalization bounds its amplitude by $B_h/2$, while Eq. (B.28) controls midpoint discretization.

The rotation (B.21) converts the midpoint mean into a_h. Amplitude estimation requires $O(\max\{1, B_h/\epsilon\})$ state-preparation calls. Balancing this count with the classical interpolation cost gives Eqs. (B.35) and (B.36).

Each state-preparation call evaluates f at one midpoint and at most $\nu_{D,r}$ interpolation nodes. Reversible arithmetic computes their interpolation weights, the residual, and the controlled rotation. The remaining arithmetic and reflections contribute P_{arith}.

Uniform absolute error bounds control the evaluation bias, while Lemma 11 controls repeated gate errors. These requirements give the stated gate estimate under the assumed arithmetic model. □

B.2 Reversible evaluation and total computational cost

For an integration region σ, let Φ_σ denote the full coordinate map from the unit cube to the physical momentum and time variables, including the endpoint power substitutions of Appendix A. That appendix also constructs the completed interaction amplitude, including the diagram cancellations and partition weights.

The circuit implements

$$U_{f_\sigma} : |x\rangle|0\rangle_Y|0\rangle_W \longmapsto |x\rangle|\widetilde{f}_\sigma(x)\rangle_Y|0\rangle_W, \tag{B.44}$$

where Y contains the finite-precision integrand value and W is temporary workspace.

I calculate the coordinate transformation and Jacobian reversibly, evaluate the covariance factors, propagators, interaction vertices, and observable windows, and assemble the completed diagram sum. For a cancellation group B_σ, the transformed integrand is

$$\begin{aligned} f_\sigma(x) = {} & |\det D\Phi_\sigma(x)|\, \chi_\sigma(\Phi_\sigma(x)) \\ & \times \sum_{G \in B_\sigma} c_G A_G(\Phi_\sigma(x)). \end{aligned} \tag{B.45}$$

Here c_G contains the signs and combinatorial factors, and χ_σ is the region weight. The amplitude A_G is the contracted product of the physical factors defined in Eq. (A.15). The result is copied into the output register before the temporary arithmetic is reversed.

The evaluation uses the stable combined formula of Definition 5. Apparent poles and large cancelling contributions are handled algebraically or through local expansions with controlled remainders. This representation determines the numerical precision required by the circuit.

Suppose the formula contains J terms, each with at most F elementary factors. Include coefficients among the factors and assume their magnitudes are bounded by $B \geq 1$. If each factor is evaluated to absolute error at most $\delta_{\text{prim}} \leq 1$, the product and triangle inequalities give

$$\delta_f \leq CJF(1+B)^{F-1}\delta_{\text{prim}}, \tag{B.46}$$

where C incorporates the fixed arithmetic convention. A sufficient primitive accuracy is therefore

$$\delta_{\text{prim}} \leq \frac{c\,\delta_f}{JF(1+B)^{F-1}}. \tag{B.47}$$

The required bit precision grows with

$$\log(1/\delta_f) + \log(1+J) + \log(1+F) + F\log(1+B), \tag{B.48}$$

together with the precision required by the elementary functions and maps.

This estimate uses absolute error. Zeros of the completed integrand impose no relative-error requirement. intermediate values can nevertheless increase B and the arithmetic cost. The derivative norm M_σ and the intermediate-value bound $B_{\mathrm{abs},\sigma}$ therefore enter different parts of the resource estimate.

I denote the cost of one reversible sector evaluation by $C_{\mathrm{eval},\sigma}(b)$. For an explicit representation containing J_σ terms of at most F_σ factors each, direct evaluation gives

$$C_{\mathrm{eval},\sigma}(b) = O\big[J_\sigma F_\sigma C_{\mathrm{factor},\sigma}(b) + C_{\mathrm{map},\sigma}(b) + C_{\mathrm{sum},\sigma}(b)\big]. \tag{B.49}$$

The terms count elementary-factor evaluation, coordinate transformation, and the remaining arithmetic of the combined sum. A nontrivial numerical propagator is included in the relevant factor cost.

Algebraic factorization, symmetry reduction, and reuse of intermediate expressions can reduce this cost. Their construction belongs to classical preprocessing. The dependence on formula size remains explicit, even though the number of diagram terms is finite at fixed perturbative order.

Suppose the coefficient $Q_K(T)$ is the sum of S transformed regions, with

$$f_\sigma : [0,1]^{D_\sigma} \longrightarrow \mathbb{R}, \qquad \|f_\sigma\|_{W^r_\infty} \le M_\sigma. \tag{B.50}$$

I allocate tolerances $\epsilon_\sigma > 0$ satisfying

$$\sum_{\sigma=1}^{S} \epsilon_\sigma \le \epsilon. \tag{B.51}$$

Each allocation covers classical interpolation arithmetic, midpoint discretization, integrand evaluation bias, amplitude estimation, and gate implementation.

For the optimized mesh in each region, the classical and quantum evaluation counts satisfy

$$N_{\mathrm{coarse},\sigma} = O_{D_\sigma,r}\left[\max\left\{1, \left(\frac{M_\sigma}{\epsilon_\sigma}\right)^{D_\sigma/(D_\sigma+r)}\right\}\right], \tag{B.52}$$

$$N_{\mathrm{q},\sigma} = O_{D_\sigma,r}\left[\max\left\{1, \left(\frac{M_\sigma}{\epsilon_\sigma}\right)^{D_\sigma/(D_\sigma+r)}\right\}\right]. \tag{B.53}$$

The first counts classical evaluations of f_σ, while the second counts quantum residual state-preparation calls. Each quantum call requires at most $1 + r^{D_\sigma}$ coherent evaluations of f_σ, including the local interpolation nodes. This factor enters the gate cost below and is absorbed into $O_{D_\sigma,r}$ only when D_σ and r are fixed.

The quantum gate cost is

$$G_{\mathrm{q},\sigma} = O\left[N_{\mathrm{q},\sigma}\left((1+\nu_{D_\sigma,r})C_{\mathrm{eval},\sigma}(b_\sigma) + P_\sigma\right)\right], \tag{B.54}$$

where P_σ includes interpolation, coordinate arithmetic, normalization, controlled rotations, and amplitude-estimation operations not already charged to $C_{\mathrm{eval},\sigma}$.

The quantum workspace obeys

$$Q_{\mathrm{q},\sigma} = O\big[D_\sigma q_\sigma + W_{\mathrm{eval},\sigma}(b_\sigma) + b_\sigma + \log(1+N_{\mathrm{q},\sigma})\big]. \tag{B.55}$$

The terms account for integration coordinates, integrand-evaluation workspace, arithmetic registers, and amplitude-estimation controls.

Theorem 13 (Conditional resource bounds for a fixed perturbative coefficient)**.** *Fix perturbative order K, observable degree n, final time T, and derivative order $r \geq 2$. Assume the following conditions hold.*

1. *$Q_K(T)$ has the deterministic integral representation of Proposition 3.*
2. *The required diagram cancellations have been performed, and the integrals admit a finite decomposition into regions.*
3. *Each region has the endpoint representation of Definition 4 with explicit coordinate transformations.*
4. *After endpoint smoothing, $\|f_\sigma\|_{W^r_\infty} \leq M_\sigma$, and the completed integrand admits stable evaluation in the sense of Definition 5.*
5. *The reversible evaluation circuit has certified gate cost $C_{\mathrm{eval},\sigma}(b)$ and workspace $W_{\mathrm{eval},\sigma}(b)$ at the required absolute precision.*

Then a hybrid classical–quantum algorithm estimates $Q_K(T)$ to additive error ϵ, with fixed success probability, without quantum random-access memory.

For fixed region count, dimensions, and derivative order, the combined function evaluation count is

$$N_{\mathrm{total}} = O\left[\sum_{\sigma=1}^{S} \max\left\{1, \left(\frac{M_\sigma}{\epsilon_\sigma}\right)^{D_\sigma/(D_\sigma+r)}\right\}\right], \qquad \sum_{\sigma=1}^{S} \epsilon_\sigma \leq \epsilon. \tag{B.56}$$

The gate and qubit costs are given by Eqs. (B.54) *and* (B.55)*. Classical graph construction, cancellation analysis, coordinate transformations, derivative certification, and coarse integration remain separate computational costs.*

Proof. Apply Theorem 12 to every transformed region. The bound M_σ determines its interpolation mesh and residual amplitude. The coarse integral is calculated classically; amplitude estimation evaluates the residual midpoint mean.

Equation (B.28) controls the midpoint error. The uniform absolute accuracy of the evaluation circuit controls the integrand bias, and Lemma 11 bounds accumulated gate errors. The remaining integration error is allocated to amplitude estimation.

Summing the regional estimates gives the stated error bound by the triangle inequality. Standard repetition and median selection establish fixed success probability for their combined result, with logarithmic overhead in the number of regions when necessary.

The function-evaluation bounds follow from Eqs. (B.52) and (B.53). The reversible evaluation circuit and amplitude-estimation operations give the gate and workspace bounds. All analytical preprocessing and certification costs are charged separately. □

The classical work is

$$C_{\mathrm{classical}} = C_{\mathrm{pre}}(K, n; \mathcal{I}, b) + C_{\mathrm{cert}}(K, n, r; \mathcal{I}, b) + W_{\mathrm{coarse}}, \tag{B.57}$$

where

$$W_{\mathrm{coarse}} = \sum_{\sigma=1}^{S} N_{\mathrm{coarse},\sigma} C^{\mathrm{cl}}_{\mathrm{eval},\sigma}(b_\sigma). \tag{B.58}$$

The superscript cl denotes classical evaluation of the same integrand formula. The complete resource accounting is

$$\mathcal{R} = \left(C_{\mathrm{pre}}, C_{\mathrm{cert}}, W_{\mathrm{coarse}}, N_{\mathrm{q}}, G_{\mathrm{q}}, Q_{\mathrm{q}}\right). \tag{B.59}$$

Algorithm 1 Quantum integration of a fixed perturbative coefficient

Input. Evolution data (S, V, C), observable weights, order K, tolerance ϵ, derivative order r

Expand the nonlinear solution through order K
Perform Gaussian contractions and eliminate dependent momenta
Assemble diagram sums with the required cancellations
Decompose the integrals and map each region to a unit cube
Establish derivative and intermediate-value bounds
Allocate numerical tolerances among the regions
for each region σ **do**
    Construct and integrate the coarse interpolant classically
    Build the reversible residual-evaluation circuit
    Estimate the residual integral by amplitude estimation
    Add the coarse and residual contributions
end for
Sum the regional estimates and return $\widehat{Q}_K(T)$

This retains the input-dependent preprocessing and arithmetic costs alongside the quantum query count.

The smooth-integrand construction uses certified Sobolev bounds. For an integrable function lacking such bounds, I may instead choose a normalized proposal density π that is positive wherever f is nonzero and write

$$I(f) = \mathbb{E}_{X\sim\pi}\left[\frac{f(X)}{\pi(X)}\right]. \tag{B.60}$$

Suppose a coherent sampler prepares π and a reversible circuit evaluates f/π. If the variance $\mathrm{Var}_{X\sim\pi}[f(X)/\pi(X)] \le V$, quantum mean estimation uses $\widetilde{O}(\max\{1, \sqrt{V}/\epsilon\})$ queries under the corresponding access assumptions [47, 48]. The complete cost must also include coherent state preparation and weight evaluation.

The principal algorithm uses the smooth-integrand representation. Its query rate is optimal for the ambient Sobolev information class. For integrands generated by a specific nonlinear PDE, additional symmetries and analytic structure can improve classical integration. The corresponding computational comparison must use the same input and accuracy requirements and include all resources in Eq. (B.59).

C Calibration with Burgers and Navier–Stokes

I examine two fluid equations in which the perturbative kernels and their Gaussian contractions can be calculated explicitly. Viscous Burgers evolution provides a scalar quadratic interaction with a removable denominator in its time-integrated kernel. Incompressible Navier–Stokes evolution adds tensor vertices and transverse momentum projectors. These examples verify the perturbative Gaussian reduction of Appendix A and identify the momentum limits in which the derivative bounds required by the quantum algorithm must be established.

For comparison, consider a perturbative calculation with N retained Fourier modes and the expansion [49–52]

$$u(\mathbf{x}, t; g) = \sum_{r\ge 0} g^r u^{[r]}(\mathbf{x}, t). \tag{C.1}$$

At order r, the quadratic interaction sums over the r ordered pairs satisfying $r_1 + r_2 = r - 1$. For Burgers and incompressible Navier–Stokes, the nonlinear vertices can be evaluated

using a fixed number of Fourier multipliers and pointwise products in position space. At each time step, Fourier transforms of the perturbative coefficients through order K require $O(KN\log N)$ operations, while their quadratic products require $O(K^2N)$ operations. A direct implementation over N_t time steps therefore costs

$$C_{\mathrm{rec}} = O\left[N_t(KN\log N + K^2N)\right] \tag{C.2}$$

per realization, for fixed field-component number and a fixed-stage time integrator. This estimate excludes initial-data generation, time-discretization error control, and arithmetic precision. Storage of the perturbative coefficients at one time requires $O(KN)$ Fourier values.

A trajectory-based ensemble calculation repeats this evolution for independently sampled initial fields and averages the resulting observables. Quantum mean estimation can reduce its sampling cost when coherent initial-state preparation and reversible evolution are available, with their implementation costs included. This trajectory method is one classical comparison, rather than a lower bound on the cost of evaluating fixed-order statistics. Classical algorithms can also perform Gaussian averaging analytically and evaluate the resulting integrals directly. The calculations below establish this reduction for Burgers and Navier–Stokes without solving the evolution for individual random realizations.

C.1 Viscous Burgers equation

Consider one-dimensional viscous Burgers evolution

$$\partial_t u + gu\partial_x u = \nu\partial_x^2 u, \qquad \nu > 0. \tag{C.3}$$

I retain boldface momentum notation, with $\mathbf{k},\mathbf{q} \in \mathbb{R}^1$, and define $\kappa(\mathbf{k}) = \mathbf{k}\cdot\mathbf{e}_x$. Since $u\partial_x u = \partial_x(u^2)/2$, Fourier transformation gives

$$\partial_t u_{\mathbf{k}} = -\nu|\mathbf{k}|^2 u_{\mathbf{k}} - \frac{\mathrm{i}g\kappa(\mathbf{k})}{2}\int_{\mathbb{R}} \frac{\mathrm{d}^1\mathbf{q}}{2\pi} u_{\mathbf{q}} u_{\mathbf{k}-\mathbf{q}}. \tag{C.4}$$

The initial field is centered, real, Gaussian, and translation invariant, with covariance

$$\mathbb{E}[\xi_{\mathbf{q}}\xi_{\mathbf{q}'}] = 2\pi\delta^{(1)}(\mathbf{q}+\mathbf{q}')C(\mathbf{q}), \qquad C(-\mathbf{q}) = C(\mathbf{q}). \tag{C.5}$$

Expanding $u = u^{[0]} + gu^{[1]} + \cdots$, I obtain the linear solution

$$u^{[0]}_{\mathbf{k}}(t) = \exp(-\nu|\mathbf{k}|^2 t)\xi_{\mathbf{k}} \tag{C.6}$$

and its first nonlinear correction,

$$u^{[1]}_{\mathbf{k}}(t) = \int_{\mathbb{R}} \frac{\mathrm{d}^1\mathbf{q}}{2\pi} F_2^{\mathrm{B}}(\mathbf{k},\mathbf{q};t)\xi_{\mathbf{q}}\xi_{\mathbf{k}-\mathbf{q}}. \tag{C.7}$$

Iterating Duhamel's formula gives the quadratic kernel

$$\begin{aligned} F_2^{\mathrm{B}}(\mathbf{k},\mathbf{q};t) = -\frac{\mathrm{i}\kappa(\mathbf{k})}{2}\int_0^t \mathrm{d}s\, \exp[-\nu|\mathbf{k}|^2(t-s)] \\ \times \exp\left[-\nu\big(|\mathbf{q}|^2 + |\mathbf{k}-\mathbf{q}|^2\big)s\right]. \end{aligned} \tag{C.8}$$

Define

$$\Delta(\mathbf{k},\mathbf{q}) = |\mathbf{k}|^2 - |\mathbf{q}|^2 - |\mathbf{k}-\mathbf{q}|^2 = 2\mathbf{q}\cdot(\mathbf{k}-\mathbf{q}). \tag{C.9}$$

The time integral gives

$$F_2^{\mathrm{B}}(\mathbf{k},\mathbf{q};t) = -\frac{\mathrm{i}\kappa(\mathbf{k})}{2}\exp(-\nu|\mathbf{k}|^2 t) \times \frac{\exp[\nu\Delta(\mathbf{k},\mathbf{q})t]-1}{\nu\Delta(\mathbf{k},\mathbf{q})}. \tag{C.10}$$

Although the denominator vanishes at $\Delta = 0$, the numerator vanishes there as well. Their complete quotient has the Taylor expansion

$$\frac{\exp(\nu\Delta t)-1}{\nu\Delta} = t + \frac{\nu\Delta t^2}{2} + \frac{\nu^2\Delta^2 t^3}{6} + O(\Delta^3). \tag{C.11}$$

Consequently,

$$F_2^{\mathrm{B}}(\mathbf{k},\mathbf{q};t) \longrightarrow -\frac{\mathrm{i}\kappa(\mathbf{k})t}{2}\exp(-\nu|\mathbf{k}|^2 t) \tag{C.12}$$

as $\Delta \to 0$. I evaluate the complete exponential quotient away from $\Delta = 0$ and use its Taylor expansion near that point to avoid subtracting nearly equal exponentials.

I next calculate the contribution of two first-order fields to the equal-time power spectrum, defined by

$$\mathbb{E}[u_{\mathbf{k}}(t)u_{\mathbf{k}'}(t)] = 2\pi\delta^{(1)}(\mathbf{k}+\mathbf{k}')P(\mathbf{k},t). \tag{C.13}$$

The contribution from $g^2\mathbb{E}[u^{[1]}u^{[1]}]$ is

$$P_{22}^{\mathrm{B}}(\mathbf{k},t) = 2g^2\int_{\mathbb{R}}\frac{\mathrm{d}^1\mathbf{q}}{2\pi}\left|F_2^{\mathrm{B}}(\mathbf{k},\mathbf{q};t)\right|^2 C(\mathbf{q})C(\mathbf{k}-\mathbf{q}). \tag{C.14}$$

The factor of two follows from the Gaussian contractions. Substituting Eq. (C.7) before averaging gives

$$\begin{aligned}&\mathbb{E}[u_{\mathbf{k}}^{[1]}(t)u_{\mathbf{k}'}^{[1]}(t)]\\ &= \int_{\mathbb{R}^2}\frac{\mathrm{d}^1\mathbf{q}\,\mathrm{d}^1\mathbf{q}'}{(2\pi)^2}F_2^{\mathrm{B}}(\mathbf{k},\mathbf{q};t)F_2^{\mathrm{B}}(\mathbf{k}',\mathbf{q}';t)\\ &\quad\times\mathbb{E}[\xi_{\mathbf{q}}\xi_{\mathbf{k}-\mathbf{q}}\xi_{\mathbf{q}'}\xi_{\mathbf{k}'-\mathbf{q}'}].\end{aligned} \tag{C.15}$$

Wick's theorem produces three pairings. The pairing within each quadratic vertex is supported at zero external momentum. Its contribution vanishes because the Burgers vertex contains $\kappa(\mathbf{k})$. The remaining two pairings connect the vertices. They are equal because

$$F_2^{\mathrm{B}}(\mathbf{k},\mathbf{q};t) = F_2^{\mathrm{B}}(\mathbf{k},\mathbf{k}-\mathbf{q};t). \tag{C.16}$$

The kernel also satisfies

$$F_2^{\mathrm{B}}(-\mathbf{k},-\mathbf{q};t) = \overline{F_2^{\mathrm{B}}(\mathbf{k},\mathbf{q};t)}. \tag{C.17}$$

The two cross-vertex contractions therefore give

$$\begin{aligned}&\mathbb{E}[u_{\mathbf{k}}^{[1]}(t)u_{\mathbf{k}'}^{[1]}(t)]\\ &= 2\pi\delta^{(1)}(\mathbf{k}+\mathbf{k}')\,2\int_{\mathbb{R}}\frac{\mathrm{d}^1\mathbf{q}}{2\pi}\left|F_2^{\mathrm{B}}(\mathbf{k},\mathbf{q};t)\right|^2 C(\mathbf{q})C(\mathbf{k}-\mathbf{q}).\end{aligned} \tag{C.18}$$

Multiplication by g^2 yields Eq. (C.14). Four initial Gaussian fields have been contracted into one momentum integral. The complete order-g^2 power-spectrum correction also contains the 13 contribution from the contraction of $u^{[0]}$ with $u^{[2]}$. The calculation above isolates the 22 term.

The time-integrated kernel has a useful large-momentum behavior. For fixed nonzero $\mathbf{k}$ and fixed $t > 0$,

$$\Delta(\mathbf{k}, \mathbf{q}) = -2|\mathbf{q}|^2 + O(|\mathbf{q}|) \tag{C.19}$$

as $|\mathbf{q}| \to \infty$. Hence

$$\frac{\exp(\nu\Delta t) - 1}{\nu\Delta} = \frac{1}{2\nu|\mathbf{q}|^2}\left[1 + O(|\mathbf{q}|^{-1})\right], \tag{C.20}$$

and

$$\begin{aligned} F_2^{\mathrm{B}}(\mathbf{k}, \mathbf{q}; t) = &-\frac{\mathrm{i}\kappa(\mathbf{k})}{4\nu|\mathbf{q}|^2}\exp(-\nu|\mathbf{k}|^2 t) \\ &\times \left[1 + O(|\mathbf{q}|^{-1})\right]. \end{aligned} \tag{C.21}$$

The decay is algebraic, despite the viscous exponentials in the original time integral. Interactions arbitrarily close to the initial time contribute to the high-momentum tail.

The ultraviolet 22 integrand consequently obeys

$$\begin{aligned} &\left|F_2^{\mathrm{B}}(\mathbf{k}, \mathbf{q}; t)\right|^2 C(\mathbf{q})C(\mathbf{k} - \mathbf{q}) \\ &\quad = O\left(|\mathbf{q}|^{-4} C(\mathbf{q})C(\mathbf{k} - \mathbf{q})\right) \end{aligned} \tag{C.22}$$

in magnitude, provided the covariance is nonnegative. A bounded covariance gives ultraviolet integrability in one dimension.

For derivative estimates, I divide the momentum axis into a bounded interval and two asymptotic regions. The complete exponential quotient is smooth on the bounded interval when the covariance is sufficiently differentiable. In each asymptotic region I use an inverse-momentum coordinate, including its Jacobian. The kernel contributes an explicit endpoint power, while the transformed covariance factors determine the remaining regularity. Their differentiated asymptotics must satisfy the endpoint hypotheses of Appendix A. Boundedness of C alone proves convergence here, but does not establish the required Sobolev derivative bound.

C.2 Incompressible Navier–Stokes equation

Consider an incompressible velocity field $u_i(\mathbf{x}, t)$ in $d \geq 2$ dimensions, with $\partial_i u_i = 0$. Eliminating pressure through the Leray projector gives

$$\partial_t u_i + g\,\mathcal{P}_{ij}\partial_\ell(u_j u_\ell) = \nu\nabla^2 u_i. \tag{C.23}$$

Repeated spatial indices are summed. For nonzero momentum, the Fourier projector is

$$P_{ij}(\mathbf{k}) = \delta_{ij} - \frac{(\mathbf{k})_i(\mathbf{k})_j}{|\mathbf{k}|^2}. \tag{C.24}$$

It satisfies

$$P_{ij}(\mathbf{k})(\mathbf{k})_j = 0, \qquad P_{ij}(\mathbf{k})P_{j\ell}(\mathbf{k}) = P_{i\ell}(\mathbf{k}). \tag{C.25}$$

I take the spatial mean velocity to vanish, so the zero Fourier mode is absent.

The quadratic interaction is symmetric under interchange of its incoming velocity fields. Its Fourier vertex is

$$M_{i;j\ell}(\mathbf{k}) = -\frac{\mathrm{i}}{2}\left[(\mathbf{k})_\ell P_{ij}(\mathbf{k}) + (\mathbf{k})_j P_{i\ell}(\mathbf{k})\right]. \tag{C.26}$$

The Fourier evolution equation becomes

$$\partial_t u_i(\mathbf{k},t) = -\nu|\mathbf{k}|^2 u_i(\mathbf{k},t) + g\int_{\mathbb{R}^d} \frac{\mathrm{d}^d\mathbf{q}}{(2\pi)^d} M_{i;j\ell}(\mathbf{k}) u_j(\mathbf{q},t) u_\ell(\mathbf{k}-\mathbf{q},t). \tag{C.27}$$

For fixed nonzero $\mathbf{k}$, this vertex depends only on the outgoing momentum. The operator norm of $P(\mathbf{k})$ is one, and the vertex is bounded by a constant times $|\mathbf{k}|$. Its Cartesian momentum derivatives are nevertheless singular at $\mathbf{k}=\mathbf{0}$.

I prescribe homogeneous, isotropic Gaussian initial velocity fluctuations with transverse covariance

$$\mathbb{E}[\xi_i(\mathbf{k})\xi_j(\mathbf{k}')] = (2\pi)^d \delta^{(d)}(\mathbf{k}+\mathbf{k}') P_{ij}(\mathbf{k}) C(|\mathbf{k}|). \tag{C.28}$$

The scalar function C is nonnegative and specifies the initial spectrum. The projector enforces incompressibility of the Gaussian field.

The linear solution is

$$u_i^{[0]}(\mathbf{k},t) = \exp(-\nu|\mathbf{k}|^2 t)\xi_i(\mathbf{k}). \tag{C.29}$$

Substituting it into Eq. (C.27) gives the first nonlinear coefficient,

$$u_i^{[1]}(\mathbf{k},t) = \int_{\mathbb{R}^d} \frac{\mathrm{d}^d\mathbf{q}}{(2\pi)^d} M_{i;j\ell}(\mathbf{k}) H_\nu(\mathbf{k},\mathbf{q};t) \times \xi_j(\mathbf{q})\xi_\ell(\mathbf{k}-\mathbf{q}), \tag{C.30}$$

where

$$H_\nu(\mathbf{k},\mathbf{q};t) = \exp(-\nu|\mathbf{k}|^2 t)\frac{\exp[\nu\Delta(\mathbf{k},\mathbf{q})t]-1}{\nu\Delta(\mathbf{k},\mathbf{q})}, \tag{C.31}$$

$$\Delta(\mathbf{k},\mathbf{q}) = |\mathbf{k}|^2 - |\mathbf{q}|^2 - |\mathbf{k}-\mathbf{q}|^2. \tag{C.32}$$

The scalar time integral is identical to the one obtained for Burgers evolution. In particular,

$$H_\nu(\mathbf{k},\mathbf{q};t) \longrightarrow t\exp(-\nu|\mathbf{k}|^2 t) \tag{C.33}$$

as $\Delta \to 0$. Its Taylor expansion provides the regular evaluation formula near this removable singularity.

Define the velocity covariance tensor by

$$\mathbb{E}[u_i(\mathbf{k},t)u_m(\mathbf{k}',t)] = (2\pi)^d\delta^{(d)}(\mathbf{k}+\mathbf{k}')P^u_{im}(\mathbf{k},t). \tag{C.34}$$

The contribution from $g^2\mathbb{E}[u^{[1]}u^{[1]}]$ contains four initial Gaussian fields. Wick's theorem gives two equivalent cross-vertex pairings. For nonzero external momentum, their sum is

$$P^{\mathrm{NS}}_{22,im}(\mathbf{k},t) = 2g^2\int_{\mathbb{R}^d}\frac{\mathrm{d}^d\mathbf{q}}{(2\pi)^d}|H_\nu(\mathbf{k},\mathbf{q};t)|^2 \times M_{i;j\ell}(\mathbf{k})\overline{M_{m;j'\ell'}(\mathbf{k})} \times P_{jj'}(\mathbf{q})P_{\ell\ell'}(\mathbf{k}-\mathbf{q}) \times C(|\mathbf{q}|)C(|\mathbf{k}-\mathbf{q}|). \tag{C.35}$$

The factor of two counts the two cross-vertex pairings. Their equality follows from the symmetry of $M_{i;j\ell}$ and interchange of the two incoming momenta. The projectors contract the velocity indices of the initial covariances. As in Burgers evolution, the complete order-g^2 power spectrum also contains the contraction of $u^{[0]}$ with $u^{[2]}$.

The tensor integral exposes a regularity issue absent from the scalar Burgers example. The internal projectors $P_{ij}(\mathbf{q})$ and $P_{ij}(\mathbf{k}-\mathbf{q})$ are bounded, but their Cartesian derivatives are singular where their momentum arguments vanish. I therefore analyze the neighborhoods of $\mathbf{q}=\mathbf{0}$ and $\mathbf{k}-\mathbf{q}=\mathbf{0}$ separately, with fixed nonzero external $\mathbf{k}$.

Near $\mathbf{q}=\mathbf{0}$, introduce

$$\mathbf{q}=\rho\mathbf{n}, \qquad \rho=|\mathbf{q}|, \qquad |\mathbf{n}|=1. \tag{C.36}$$

Then

$$P_{ij}(\mathbf{q})=\delta_{ij}-n_in_j, \qquad \mathrm{d}^d\mathbf{q}=\rho^{d-1}\mathrm{d}\rho\,\mathrm{d}\Omega_{d-1}. \tag{C.37}$$

The projector now depends smoothly on the angular variables and is independent of ρ. Finitely many regular angular charts cover the sphere. The remaining factors are smooth in ρ near zero, apart from the specified covariance spectrum.

For example, if

$$C(\rho)=\rho^a(\log\rho)^mA(\rho), \qquad a>-d, \tag{C.38}$$

where A has bounded derivatives through the required order, the radial measure produces the endpoint factor

$$\rho^{d-1+a}(\log\rho)^m. \tag{C.39}$$

A substitution $\rho=y^s$ gives bounded derivatives through order r when

$$s(d+a)-1>r. \tag{C.40}$$

The same analysis applies near $\mathbf{k}-\mathbf{q}=\mathbf{0}$ after interchanging the two incoming momenta. Thus the angular decomposition resolves the projector's directional dependence, while the covariance controls radial regularity.

At large internal momentum, with $\mathbf{k}\neq\mathbf{0}$ fixed and $t>0$,

$$H_\nu(\mathbf{k},\mathbf{q};t)=\frac{\exp(-\nu|\mathbf{k}|^2t)}{2\nu|\mathbf{q}|^2}\left[1+O(|\mathbf{q}|^{-1})\right]. \tag{C.41}$$

The vertex is independent of $\mathbf{q}$, and the internal projectors remain bounded. Therefore the squared time kernel contributes four inverse powers of internal momentum. In d dimensions, the radial ultraviolet integral is bounded by a constant multiple of

$$\int^\infty \mathrm{d}\rho\,\rho^{d-5}C(\rho)^2, \tag{C.42}$$

provided the covariance at $|\mathbf{k}-\mathbf{q}|$ obeys the corresponding large-momentum bound. A bounded covariance gives ultraviolet convergence for $d<4$.

To obtain the Sobolev certificate, I compactify the large-momentum region and include the radial Jacobian. The transformed covariance and its derivatives must then satisfy the regularity conditions of Appendix A. A bounded spectrum establishes the preceding convergence estimate but does not guarantee bounded derivatives after compactification. The projector factors require regular angular coordinates, while the radial factors and covariance determine the endpoint powers and smoothing substitutions.

The Burgers calculation establishes the exact time-integrated quadratic kernel, its removable denominator, and the two cross-vertex Wick contractions. Navier–Stokes retains the same scalar time structure but adds transverse tensor contractions. For both equations, Gaussian averaging reduces the first nonlinear power-spectrum contribution to one internal momentum integral. The subsequent integration bounds depend on the regularity of the prescribed initial covariance.

D GGRW technical details and Euler–Poisson singularities

D.1 GGRW kernels and one-loop momentum integrals

I apply the general perturbative construction to the Euler–Poisson equations in an Einstein–de Sitter (EdS) universe. The regular growing solution has time-independent momentum kernels, so its statistical coefficients reduce to momentum integrals. This permits a direct identification of the graph expansion with the GGRW hierarchy and an explicit analysis of its one-loop integrals.

For pressureless matter in comoving coordinates and conformal time τ, the equations are

$$\begin{aligned} \partial_\tau \delta + \nabla \cdot [(1+\delta)\mathbf{v}] &= 0, \\ \partial_\tau \mathbf{v} + \mathcal{H}\mathbf{v} + (\mathbf{v}\cdot\nabla)\mathbf{v} &= -\nabla\phi, \\ \nabla^2\phi &= \frac{3}{2}\mathcal{H}^2\Omega_m\delta. \end{aligned} \tag{D.1}$$

Here δ is the density contrast, $\mathbf{v}$ the peculiar velocity in conformal coordinates, and $\mathcal{H} = a'/a$ the conformal Hubble parameter. EdS has $\Omega_m = 1$ and vanishing cosmological constant, with

$$a(t) \propto t^{2/3}, \qquad D_+(a) = a, \qquad f \equiv \frac{\mathrm{d}\log D_+}{\mathrm{d}\log a} = 1. \tag{D.2}$$

Set $\eta = \log a$ and introduce the density–velocity doublet

$$\Psi_a(\mathbf{k},\eta) = \left(\delta(\mathbf{k},\eta), -\frac{\theta(\mathbf{k},\eta)}{\mathcal{H}}\right)_a, \qquad \theta = \nabla\cdot\mathbf{v}. \tag{D.3}$$

Its evolution has the quadratic form

$$\begin{aligned} \partial_\eta \Psi_a(\mathbf{k},\eta) + \Omega_{ab}\Psi_b(\mathbf{k},\eta) = \int \frac{\mathrm{d}^3q}{(2\pi)^3}\gamma_{abc}(\mathbf{k},\mathbf{q},\mathbf{k}-\mathbf{q}) \\ \times \Psi_b(\mathbf{q},\eta)\Psi_c(\mathbf{k}-\mathbf{q},\eta), \end{aligned} \tag{D.4}$$

where

$$\Omega = \begin{pmatrix} 0 & -1 \\ -3/2 & 1/2 \end{pmatrix}. \tag{D.5}$$

The eigenvalues of $-\Omega$ are 1 and $-3/2$. Thus the linear system has a growing mode proportional to a and a decaying mode proportional to $a^{-3/2}$. Hubble drag acts on the velocity, but self-gravity preserves the growing density mode.

The EdS matrix and quadratic vertices are independent of η. Consequently, the regular growing solution factorizes into powers of D_+ and time-independent momentum kernels. In a general FLRW background, the propagators and perturbative kernels become time dependent. For a single pressureless fluid in ΛCDM, the kernels can be expanded in momentum functions whose time-dependent coefficients satisfy coupled ordinary differential equations [53]. These coefficients can be calculated before the momentum integrations, without retaining the interaction times as additional integration variables.

Introduce an auxiliary vertex counter g,

$$\partial_\eta\Psi + \Omega\Psi = g\,\gamma[\Psi,\Psi], \tag{D.6}$$

and impose the regular growing boundary condition as $\eta \to -\infty$. The perturbative solution is

$$\Psi_a(\mathbf{k},\eta;g) = \sum_{r\geq 1} g^{r-1} D_+^r(\eta)\Psi_a^{(r)}(\mathbf{k}). \tag{D.7}$$

The density component is

$$\delta^{(r)}(\mathbf{k}) = \int \left[\prod_{j=1}^{r} \frac{\mathrm{d}^3 q_j}{(2\pi)^3}\right] (2\pi)^3 \delta_D^{(3)}\left(\sum_{j=1}^{r} \mathbf{q}_j - \mathbf{k}\right) \times F_r^{(s)}(\mathbf{q}_1, \ldots, \mathbf{q}_r) \prod_{j=1}^{r} \delta_0(\mathbf{q}_j). \tag{D.8}$$

The symmetrized kernels $F_r^{(s)}$ follow from the EdS quadratic vertices

$$\alpha(\mathbf{p}, \mathbf{q}) = \frac{(\mathbf{p}+\mathbf{q})\cdot\mathbf{p}}{p^2}, \qquad \beta(\mathbf{p}, \mathbf{q}) = \frac{|\mathbf{p}+\mathbf{q}|^2(\mathbf{p}\cdot\mathbf{q})}{2p^2q^2}, \tag{D.9}$$

where $p = |\mathbf{p}|$ and $q = |\mathbf{q}|$. Substituting Eq. (D.7) into Eq. (D.6) reproduces the algebraic GGRW recursion. Each term of degree r in the initial field contains $r-1$ quadratic vertices.

Proposition 14 (GGRW identification)**.** *For the regular EdS growing solution, the coefficient with K quadratic vertices in the general iterative expansion equals the GGRW contribution of total primordial degree $n+K$ to an n-point statistic.*

For a connected contribution with L statistical loops, the number I of primordial covariance lines satisfies

$$K = n - 2 + 2L, \qquad I = n - 1 + L, \qquad D_+\text{-power} = 2I. \tag{D.10}$$

Proof. An n-point contribution with K quadratic vertices contains $n+K$ initial fields. Wick pairing joins them into $I = (n+K)/2$ covariance lines.

Collapse each rooted interaction tree to its external root. The connected covariance graph has n vertices and I edges, so its cycle number is $L = I - n + 1$. Eliminating I gives $K = n - 2 + 2L$ and $I = n - 1 + L$. Each initial field contributes one factor of D_+, giving the stated growth power. □

The factorization assumes the regular growing boundary condition. Initializing the fluid at a finite scale factor with approximate growing data generally introduces decaying-mode transients. Their kernels acquire additional time dependence.

The linear density field is

$$\delta_L(\mathbf{k}, a) = D_+(a)\delta_0(\mathbf{k}). \tag{D.11}$$

The dimensionless linear power or the smoothed variance determines the physical size of perturbative corrections. Powers of D_+ describe their time dependence once the initial normalization has been fixed.

The loops in this expansion arise from Gaussian averaging of a classical random field. For the power spectrum,

$$P(k, a) = D_+^2 P_{11}(k) + D_+^4[P_{22}(k) + P_{13}(k)] + D_+^6 P_{2\text{loop}}(k) + \cdots. \tag{D.12}$$

The one-loop coefficients are

$$P_{22}(k) = 2\int \frac{\mathrm{d}^3 q}{(2\pi)^3} \left|F_2^{(s)}(\mathbf{q}, \mathbf{k}-\mathbf{q})\right|^2 P_0(q) P_0(|\mathbf{k}-\mathbf{q}|),$$
$$P_{13}(k) = 6P_0(k) \int \frac{\mathrm{d}^3 q}{(2\pi)^3} F_3^{(s)}(\mathbf{k}, \mathbf{q}, -\mathbf{q}) P_0(q). \tag{D.13}$$

For the bispectrum,

$$B = D_+^4 B_{\text{tree}} + D_+^6 B_{1\text{loop}} + D_+^8 B_{2\text{loop}} + \cdots. \tag{D.14}$$

The same counting applies to higher connected correlations, including cumulants of the density averaged over a Gaussian ball,

$$\kappa_{n,R}^{(L)}(a) = \langle \delta_R^n(a) \rangle_{c,L} \,. \tag{D.15}$$

The numerical algorithm calculates the momentum coefficient at fixed order. Its EdS time dependence is restored by Eq. (D.10).

I now specify the statistical input. The initial growing density amplitude is Gaussian, with

$$\mathbb{E}[\delta_0(\mathbf{k})\delta_0(\mathbf{k}')] = (2\pi)^3 \delta_D^{(3)}(\mathbf{k}+\mathbf{k}') P_0(k). \tag{D.16}$$

Here $P_0(k)$ is the prescribed linear matter power spectrum at a reference epoch normalized by $D_+ = 1$. It is an input covariance, not the nonlinear power spectrum being calculated.

The original GGRW benchmark uses a cold-dark-matter model with a Harrison–Zel'dovich primordial spectrum. For a modern linear matter benchmark, one may instead use the total CDM–baryon density spectrum. In the adiabatic, pressureless single-fluid approximation, its transfer function can be written

$$T_m(k) = f_c T_c(k) + f_b T_b(k), \qquad f_c + f_b = 1, \tag{D.17}$$

where f_c and f_b are the CDM and baryon fractions. Accordingly,

$$P_0(k) = A_s k^{n_s} T_m(k)^2 \tag{D.18}$$

with dimensional reference factors absorbed into A_s. This spectrum contains the baryonic transfer features while retaining the same EdS evolution kernels in the stated single-fluid approximation. Scale-dependent growth from additional dynamical components requires an extension of those kernels.

For the endpoint analysis I impose regularity conditions directly on P_0. In the infrared, take

$$P_0(k) = k^{n_s} A_{\mathrm{IR}}(k), \qquad A_{\mathrm{IR}} \in C^2([0, k_{\mathrm{IR}}]), \tag{D.19}$$

with $n_s > -1$. At finite nonzero momentum, require $P_0 \in C^2$. In the ultraviolet, suppose that, for $j = 0, 1, 2$,

$$\left| \frac{\mathrm{d}^j P_0(k)}{\mathrm{d}k^j} \right| \le C_j k^{n_s - 4 - j} \left[1 + \log(k/k_{\mathrm{UV}}) \right]^2, \qquad k \ge k_{\mathrm{UV}}, \tag{D.20}$$

where $-1 < n_s < 3$ and k_{UV} is chosen beyond the transfer-function turnover. These bounds describe the usual logarithmically corrected matter-spectrum tail, subject to verification for the selected transfer function. The historical case $n_s = 1$ has

$$P_0(k) = O(k^{-3} \log^2 k). \tag{D.21}$$

The derivative conditions, rather than this leading value alone, enter the Sobolev certificate.

A second ingredient is the hard-pair behavior of the symmetrized gravitational kernels. For one pair of large opposite momenta and fixed remaining momenta, the explicitly verified low-order kernels satisfy

$$F_r^{(s)}(\mathbf{k}_1, \ldots, \mathbf{k}_{r-2}, \mathbf{p}, -\mathbf{p}) = O(p^{-2}), \qquad p \to \infty. \tag{D.22}$$

The leading contributions of the unsymmetrized terms cancel after their permutations are added. GGRW use this decoupling together with the initial spectrum to analyze ultraviolet convergence. At higher orders, or when several independent momentum combinations become hard, the complete kernel requires a corresponding derivation.

For Gaussian-ball observables, define

$$\delta_R(\mathbf{x}, a) = \int \frac{\mathrm{d}^3 k}{(2\pi)^3} \exp(-k^2 R^2/4) \exp(\mathrm{i}\mathbf{k} \cdot \mathbf{x}) \delta(\mathbf{k}, a). \tag{D.23}$$

Every external momentum is weighted by a Gaussian factor. Internal loop momenta are controlled by the interaction kernels and the covariance spectrum. Their convergence must be checked in all simultaneous soft and hard regions.

Proposition 15 (Degree-eight GGRW dimension bound)**.** *For the regular EdS growing hierarchy with Gaussian initial data, every connected contribution of total primordial degree at most eight can be represented using at most four independent primordial covariance momenta. A conservative Gaussian-ball representation therefore has*

$$D \leq 12. \tag{D.24}$$

Momentum conservation and rotational symmetry can reduce this dimension.

Proof. A contribution of total primordial degree at most eight contains at most four Gaussian covariance contractions. Assign one three-dimensional momentum to each covariance line. The vertex constraints express all other momenta as linear combinations of these variables. Thus twelve real momentum coordinates suffice. □

The dimension bound is independent of the ultraviolet cutoff. Its derivative constants need not be. If the complete degree-eight integrands admit uniform W^2_∞ certificates after their momentum transformations, the general integration theorem gives the conservative query exponent

$$\frac{D}{D+2} \leq \frac{6}{7}. \tag{D.25}$$

Establishing this estimate for all degree-eight GGRW contributions requires the corresponding multi-hard and partial-momentum bounds.

The connected contributions through degree eight are organized as follows:

Connected function	Loop order	Growth power	Covariance lines	Highest kernel
2-point	0	a^2	1	F_1
2-point	1	a^4	2	F_3
2-point	2	a^6	3	F_5
2-point	3	a^8	4	F_7
3-point	0	a^4	2	F_2
3-point	1	a^6	3	F_4
3-point	2	a^8	4	F_6
4-point	0	a^6	3	F_3
4-point	1	a^8	4	F_5
5-point	0	a^8	4	F_4

The connected six-point function begins at primordial degree ten.

I now establish the endpoint behavior of the one-loop power-spectrum integrals. For $n_s > -1$, both P_{22} and P_{13} are separately infrared convergent. Their leading soft-momentum contributions nevertheless cancel in the sum $P_{22} + P_{13}$, as required by the equivalence principle [9]. This cancellation can be implemented at the integrand level, as in the infrared-safe formulation of Carrasco et al. [54]. I retain the separate representations here to exploit the lower-dimensional radial integral for P_{13}. The P_{22} contribution is

$$P_{22}(k) = 2 \int \frac{\mathrm{d}^3 q}{(2\pi)^3} \left| F_2^{(s)}(\mathbf{q}, \mathbf{k} - \mathbf{q}) \right|^2 P_0(q) P_0(|\mathbf{k} - \mathbf{q}|). \tag{D.26}$$

For the symmetrized EdS kernel,

$$F_2^{(s)}(\mathbf{p},\mathbf{q}) = \frac{5}{7} + \frac{1}{2}\frac{\mathbf{p}\cdot\mathbf{q}}{pq}\left(\frac{p}{q}+\frac{q}{p}\right) + \frac{2}{7}\left(\frac{\mathbf{p}\cdot\mathbf{q}}{pq}\right)^2. \tag{D.27}$$

This expression permits direct analysis of the two soft regions and the hard-momentum limit.

Fix $\mathbf{k} \neq \mathbf{0}$. Near $\mathbf{q} = \mathbf{0}$, write

$$\mathbf{q} = \rho\mathbf{n}, \qquad \rho = |\mathbf{q}|, \qquad |\mathbf{n}| = 1. \tag{D.28}$$

The kernel expands as

$$F_2^{(s)}(\rho\mathbf{n}, \mathbf{k}-\rho\mathbf{n}) = \frac{\mathbf{k}\cdot\mathbf{n}}{2\rho} + O(1). \tag{D.29}$$

The remainder and its required derivatives are regular in ρ and in smooth angular coordinates for sufficiently small ρ. Using the infrared spectrum $P_0(\rho) = \rho^{n_s} A_{\rm IR}(\rho)$, the full radial integrand, including the measure $\rho^2 \mathrm{d}\rho$, takes the form

$$\rho^{n_s} H_{\rm IR}(\rho,\mathbf{n})\,\mathrm{d}\rho\,\mathrm{d}\Omega_2, \tag{D.30}$$

where

$$H_{\rm IR}(\rho,\mathbf{n}) = \frac{2}{(2\pi)^3} A_{\rm IR}(\rho) P_0(|\mathbf{k}-\rho\mathbf{n}|)\left|\rho F_2^{(s)}(\rho\mathbf{n},\mathbf{k}-\rho\mathbf{n})\right|^2. \tag{D.31}$$

For $\rho < k/2$, the argument of P_0 remains separated from zero, while $\rho F_2^{(s)}$ is smooth in ρ and the angular variables. The stated C^2 assumptions on $A_{\rm IR}$ and P_0, together with the product and chain rules, therefore give bounded derivatives of $H_{\rm IR}$ through order two on regular angular charts.

Choose an integer $s_{\rm IR} > 0$ satisfying

$$s_{\rm IR}(n_s+1) - 1 > 2. \tag{D.32}$$

The substitution $\rho = y^{s_{\rm IR}}$, including its Jacobian, gives

$$s_{\rm IR} y^{s_{\rm IR}(n_s+1)-1} H_{\rm IR}(y^{s_{\rm IR}},\mathbf{n})\,\mathrm{d}y\,\mathrm{d}\Omega_2. \tag{D.33}$$

This function has bounded derivatives through order two at $y = 0$. For the Harrison–Zel'dovich value $n_s = 1$, the choice $s_{\rm IR} = 2$ produces the factor $2y^3$.

The second soft region, $\mathbf{k}-\mathbf{q} \to \mathbf{0}$, is identical after setting $\mathbf{p} = \mathbf{k}-\mathbf{q}$. A finite collection of regular angular charts covers the corresponding spheres. Together with a compact region separated from both soft points, these charts control the bounded-momentum domain.

The hard region admits a particularly simple exact expression. Write

$$\mathbf{q} = \rho\mathbf{n}, \qquad \mu = \frac{\mathbf{k}\cdot\mathbf{n}}{k}, \qquad x = \frac{k}{\rho}. \tag{D.34}$$

The second-order kernel becomes

$$F_2^{(s)}(\mathbf{q},\mathbf{k}-\mathbf{q}) = \frac{k^2}{14\rho^2}\frac{3-10\mu^2+7x\mu}{1-2x\mu+x^2}. \tag{D.35}$$

For $\rho > 2k$, the denominator is uniformly separated from zero. The kernel and its differentiated asymptotic expansion are therefore uniform in the angular variables, with

$$F_2^{(s)}(\mathbf{q},\mathbf{k}-\mathbf{q}) = \frac{k^2}{14\rho^2}(3-10\mu^2) + O(\rho^{-3}). \tag{D.36}$$

The differentiated ultraviolet bounds on P_0 now determine the endpoint behavior. The radial integrand, including its measure, obeys

$$\rho^2 \left|F_2^{(s)}\right|^2 P_0(\rho) P_0(|\mathbf{k}-\rho\mathbf{n}|) = O\left(\rho^{2n_s-10}[1+\log\rho]^4\right), \tag{D.37}$$

with corresponding derivative bounds. Under $z = 1/\rho$, including $\mathrm{d}\rho = z^{-2}\mathrm{d}z$, the transformed integrand has order

$$O\left(z^{8-2n_s}[1+|\log z|]^4\right). \tag{D.38}$$

For $n_s < 3$, the endpoint exponent $8 - 2n_s$ is greater than two. The differentiated kernel and spectrum bounds therefore give a C^2 extension at $z = 0$, uniformly in regular angular coordinates.

The soft neighborhoods, compact region, and hard region provide a finite W^2_∞ representation of P_{22} under the stated spectral assumptions. The transformed derivative bound depends on the actual functions A_{IR} and P_0, the external momentum k, and the chosen coordinate charts. These dependencies enter the constant M_{22} rather than the query exponent.

The second one-loop contribution is

$$P_{13}(k) = 6P_0(k)\int \frac{\mathrm{d}^3q}{(2\pi)^3} F_3^{(s)}(\mathbf{k},\mathbf{q},-\mathbf{q})P_0(q). \tag{D.39}$$

Angular integration gives the standard one-dimensional EdS representation [38],

$$P_{13}(k) = \frac{k^3 P_0(k)}{252(4\pi^2)}\int_0^\infty \mathrm{d}r\, P_0(kr)\mathcal{K}_{13}(r), \tag{D.40}$$

where

$$\begin{aligned}\mathcal{K}_{13}(r) = {}& \frac{12}{r^2} - 158 + 100r^2 - 42r^4 \\ & + \frac{3}{r^3}(r^2-1)^3(7r^2+2)\log\left|\frac{1+r}{1-r}\right|.\end{aligned} \tag{D.41}$$

The apparent singularities of this expression cancel in the complete kernel.

At $r = 1$, write $r = 1 + h$. Direct expansion gives

$$\begin{aligned}\mathcal{K}_{13}(1+h) = {}& -88 + 8h - 116h^2 \\ & + 216h^3\left[\log 2 - 1 - \log|h|\right] + O(h^4|\log|h||).\end{aligned} \tag{D.42}$$

The term $h^3\log|h|$ has two continuous derivatives at $h = 0$. Thus the complete kernel belongs to C^2 across $r = 1$. Its polynomial prefactor must be combined with the logarithm before differentiation or numerical evaluation.

At large r,

$$\mathcal{K}_{13}(r) = -\frac{488}{5} + \frac{96}{5r^2} - \frac{160}{21r^4} + O(r^{-6}). \tag{D.43}$$

Its differentiated asymptotic expansion is bounded through second order. The ultraviolet spectrum gives

$$P_0(kr) = O\left(r^{n_s-4}[1+\log r]^2\right). \tag{D.44}$$

Hence the radial integral converges for $n_s < 3$.

To establish the derivative bound, choose an integer s_{UV} satisfying

$$s_{\mathrm{UV}}(3-n_s) - 1 > 2 \tag{D.45}$$

and set $r = y^{-s_{\rm UV}}$. Including the Jacobian, the ultraviolet integrand becomes

$$f_{13}^{\rm UV}(y) = s_{\rm UV} y^{-s_{\rm UV}-1} P_0(k y^{-s_{\rm UV}}) \times \mathcal{K}_{13}(y^{-s_{\rm UV}}). \tag{D.46}$$

The ultraviolet derivative bounds on P_0 and the expansion (D.43) imply

$$\left| \frac{\mathrm{d}^j f_{13}^{\rm UV}}{\mathrm{d}y^j} \right| \le C_j y^{s_{\rm UV}(3-n_s)-1-j} [1 + |\log y|]^2, \qquad j = 0, 1, 2. \tag{D.47}$$

All three expressions tend to zero as $y \to 0$. For $n_s = 1$, the choice $s_{\rm UV} = 2$ gives the familiar endpoint factor of order $y^3(\log y)^2$.

The infrared radial expansion is

$$\mathcal{K}_{13}(r) = -168 + \frac{928}{5} r^2 - \frac{4512}{35} r^4 + O(r^6). \tag{D.48}$$

Since $P_0(kr) = r^{n_s}$ times a regular factor, the substitution $r = y^{s_{\rm IR}}$ used for the P_{22} soft region also gives two bounded derivatives at $r = 0$. The compact intervals away from these endpoints are C^2 by the regularity assumed for P_0.

The complete one-loop calculation thus admits a finite collection of transformed integrands in W^2_∞, with norms bounded by a constant $M_{\rm 1loop}$ determined by the specified spectrum and coordinate maps. Applying Theorem 13 with $r = 2$, and retaining at most three momentum coordinates, gives

$$N_{\rm eval} = O\left[\max\left\{ 1, \left(\frac{M_{\rm 1loop}}{\epsilon} \right)^{3/5} \right\} \right]. \tag{D.49}$$

The gate cost includes reversible evaluation of the spectrum, kernels, and coordinate maps. This is the quantum integration upper bound for the specified representation. Rotational reduction also gives a two-dimensional representation of P_{22} and the one-dimensional representation (D.40). FAST-PT and FFTLog-based methods exploit the convolution structure of these loop integrals [35, 36]. Their computational costs, together with the reversible integrand evaluation and interpolation overhead, must enter any end-to-end comparison for the physical GGRW coefficients.

D.2 Flat-space Euler–Poisson and caustic formation

The GGRW expansion describes the regular single-stream branch of pressureless gravitational evolution. I now identify the singularity that limits this branch, first in flat space and then in an expanding background.

Let $\rho(\mathbf{x}, t) \ge 0$ be the mass density, $\mathbf{u}(\mathbf{x}, t)$ the Eulerian velocity, and $\Phi(\mathbf{x}, t)$ the Newtonian potential. The isentropic Euler–Poisson system is

$$\partial_t \rho + \nabla \cdot (\rho \mathbf{u}) = 0, \tag{D.50}$$

$$\partial_t \mathbf{u} + (\mathbf{u} \cdot \nabla)\mathbf{u} + \frac{1}{\rho} \nabla p(\rho) = -\nabla \Phi, \tag{D.51}$$

$$\Delta \Phi = c_d G(\rho - \rho_b). \tag{D.52}$$

The coefficient c_d fixes the dimensional Newtonian normalization. For an isolated system, $\rho_b = 0$ and the potential obeys the appropriate condition at infinity. On a periodic domain, the source must have zero mean, so $\rho_b = \langle \rho \rangle$. The pressureless model has $p = 0$.

The Cauchy data are

$$\rho(\mathbf{x},0)=\rho_0(\mathbf{x}),\qquad \mathbf{u}(\mathbf{x},0)=\mathbf{u}_0(\mathbf{x}). \tag{D.53}$$

The potential is fixed by the Poisson constraint and its boundary conditions; it is not independent initial data.

For an isentropic pressure law with

$$c_s^2(\rho)=p'(\rho)>0, \tag{D.54}$$

the Euler block is symmetrizable hyperbolic away from vacuum. The Poisson equation supplies a nonlocal elliptic constraint. Its force does not introduce an additional propagating characteristic. The local characteristic speeds are $\mathbf{u}\cdot\mathbf{n}\pm c_s$ and the advected speeds. When $p=0$, the acoustic speeds coalesce. At positive density, the principal Euler matrix is no longer diagonalizable, and the pressureless system becomes weakly hyperbolic.

The distinction affects local theory. For smooth positive-density solutions with a regular pressure law, classical evolution continues while the necessary Sobolev norms and density conditions remain controlled. Physical-vacuum boundaries require additional weighted estimates [55]. Pressureless Euler–Poisson instead admits a characteristic description until the Lagrangian map loses invertibility. Critical-threshold and blowup results depend on the force sign, dimension, and initial compression [56, 57].

The nonlocal force can be written for an isolated system as

$$\nabla\Phi(\mathbf{x},t)=G\int_{\mathbb{R}^d}K_d(\mathbf{x}-\mathbf{y})\rho(\mathbf{y},t)\,\mathrm{d}^d y,\qquad K_d(\mathbf{z})\propto\frac{\mathbf{z}}{|\mathbf{z}|^d}. \tag{D.55}$$

The velocity transports the density, and the transported density changes the gravitational force. The convective derivative can steepen velocity gradients while gravity amplifies compression.

The force is irrotational. Taking the curl of the momentum equation eliminates $\nabla\Phi$. For barotropic pressure, the pressure force also produces no baroclinic vorticity source. An initially irrotational smooth flow therefore remains irrotational before singularity formation.

The pressureless dynamics is most transparent in Lagrangian coordinates. Let $\mathbf{X}(\mathbf{q},t)$ be the trajectory starting from label $\mathbf{q}$:

$$\frac{\mathrm{d}\mathbf{X}}{\mathrm{d}t}=\mathbf{u}(\mathbf{X},t),\qquad \mathbf{X}(\mathbf{q},0)=\mathbf{q}. \tag{D.56}$$

Define

$$J(\mathbf{q},t)=\det\nabla_{\mathbf{q}}\mathbf{X}(\mathbf{q},t). \tag{D.57}$$

Mass conservation gives

$$\rho(\mathbf{X}(\mathbf{q},t),t)J(\mathbf{q},t)=\rho_0(\mathbf{q}), \tag{D.58}$$

while each trajectory satisfies

$$\frac{\mathrm{d}^2\mathbf{X}}{\mathrm{d}t^2}=-\nabla\Phi(\mathbf{X},t). \tag{D.59}$$

As long as $J>0$, the flow map is locally invertible and the Eulerian density is single-valued. A caustic forms when J reaches zero in a region carrying nonzero initial mass. Equation (D.58) then gives an unbounded density. Beyond the first crossing, different Lagrangian labels can occupy the same Eulerian position. Their velocities need not agree, so a single-stream pressureless Eulerian description no longer represents the multi-stream flow.

This caustic differs from a compressible Euler shock. A shock requires a weak solution and an admissibility condition. The pressureless caustic is a loss of invertibility of the particle-position map. The GGRW hierarchy describes the regular single-stream evolution. Its fixed-order coefficients can remain mathematically defined after shell crossing, but they do not provide a continuation of the physical multi-stream dynamics.

For smooth isolated solutions, the Euler–Poisson system conserves mass and total energy. Define the internal-energy density $\Pi(\rho)$ by

$$\rho\Pi'(\rho) - \Pi(\rho) = p(\rho). \tag{D.60}$$

The energy is

$$E_{\text{flat}} = \int \left[\frac{1}{2}\rho|\mathbf{u}|^2 + \Pi(\rho)\right] \mathrm{d}^d x + \frac{1}{2}\int \rho\Phi \, \mathrm{d}^d x. \tag{D.61}$$

The gravitational term is negative for attractive gravity under the usual isolated-system convention. Pressureless evolution has $\Pi = 0$ and no viscous damping. The energy conservation law does not prevent concentration of density or velocity gradients.

The mathematical structures of several Euler–Poisson models are distinguished below.

Model	Principal PDE type	Singular mechanism	Application
Pressureless, attractive	Degenerate hyperbolic–elliptic	Caustics, density concentration, multistreaming	Collisionless dust before crossing
Isentropic, attractive	Symmetrizable hyperbolic–elliptic away from vacuum	Shocks, collapse, vacuum degeneracy	Self-gravitating gas
Pressureless, repulsive	Degenerate hyperbolic–elliptic	Critical-threshold gradient blowup or global smoothness	Cold plasma
Periodic neutralized	Euler classification determined by the pressure law, with mean-zero Poisson source	Depends on pressure and force sign	Homogeneous-background perturbations

The cosmological equations follow the neutralized-background structure after the homogeneous FRW solution has been separated. Expansion then modifies the velocity equation and the linear growth of density perturbations.

D.3 Einstein–de Sitter expansion and algebraic damping

I derive the effect of expansion on peculiar motion and density growth. Hubble drag suppresses free peculiar velocities, but self-gravity retains a growing density mode. Expansion therefore changes the rate of gravitational focusing without providing a spatial regulator for pressureless matter.

Let physical and comoving positions be related by $\mathbf{r} = a(t)\mathbf{x}$. Decompose the physical velocity as

$$\dot{\mathbf{r}} = H(t)\mathbf{r} + \mathbf{v}(\mathbf{x}, t), \qquad H = \frac{\dot{a}}{a}, \tag{D.62}$$

and write

$$\rho(\mathbf{r}, t) = \bar{\rho}(t)[1 + \delta(\mathbf{x}, t)]. \tag{D.63}$$

Subtracting the homogeneous FRW solution gives

$$\dot{\delta} + \frac{1}{a}\nabla \cdot [(1+\delta)\mathbf{v}] = 0, \tag{D.64}$$

$$\dot{\mathbf{v}} + H\mathbf{v} + \frac{1}{a}(\mathbf{v}\cdot\nabla)\mathbf{v} = -\frac{1}{a}\nabla\phi, \tag{D.65}$$

$$\nabla^2\phi = 4\pi G a^2 \bar{\rho}\,\delta. \tag{D.66}$$

Here ∇ differentiates with respect to comoving position.

For a freely moving particle,

$$\dot{\mathbf{v}} + H\mathbf{v} = 0 \quad \Longrightarrow \quad \mathbf{v} \propto a^{-1}. \tag{D.67}$$

Its peculiar kinetic energy falls as a^{-2}. This damping is spatially homogeneous. It contains no factor of k^2 and therefore does not suppress high spatial frequencies more strongly than low ones.

For EdS,

$$a(t) \propto t^{2/3}, \qquad H(t) = \frac{2}{3t}, \qquad 4\pi G\bar{\rho} = \frac{3}{2}H^2. \tag{D.68}$$

Free peculiar velocities decay as $t^{-2/3}$. Since $H \propto t^{-1}$, the integrated damping produces algebraic decay in cosmic time.

Linearizing Eqs. (D.64)– (D.66) gives the density equation

$$\ddot{\delta} + 2H\dot{\delta} - 4\pi G\bar{\rho}\,\delta = 0. \tag{D.69}$$

Its independent EdS solutions are

$$D_+(t) = a(t) \propto t^{2/3}, \qquad D_-(t) = a^{-3/2}(t) \propto t^{-1}. \tag{D.70}$$

Self-gravity overcomes Hubble drag on the growing branch. In $\eta = \log a$, these solutions become exponentials with constant exponents 1 and $-3/2$, as obtained from Eq. (D.5).

For comparison, the neutralized homogeneous flat-space Jeans linearization with constant density ρ_0 obeys

$$\ddot{\delta} - 4\pi G\rho_0\,\delta = 0, \tag{D.71}$$

and therefore has an unstable mode

$$\delta_+(t) \propto \exp\left(\sqrt{4\pi G\rho_0}\,t\right). \tag{D.72}$$

EdS expansion replaces this exponential growth law by

$$\delta_+(t) \propto t^{2/3}. \tag{D.73}$$

The instability grows more slowly in cosmic time, but it remains an instability.

Expansion also leaves the Lagrangian criterion for shell crossing unchanged. Let $\mathbf{X}(\mathbf{q}, t)$ be the comoving particle-position map and define

$$J(\mathbf{q}, t) = \det \nabla_{\mathbf{q}} \mathbf{X}. \tag{D.74}$$

If the labels coincide with comoving positions at an initial epoch when $J = 1$, mass conservation gives

$$1 + \delta(\mathbf{X}(\mathbf{q}, t), t) = \frac{1 + \delta_i(\mathbf{q})}{J(\mathbf{q}, t)}. \tag{D.75}$$

Shell crossing occurs when the Jacobian vanishes in a region with nonzero mass.

Plane-parallel growing solutions provide an exact pre-crossing example. Using uniform Lagrangian labels at $a = 0$, write

$$X(q, a) = q + a\,s(q). \tag{D.76}$$

Then

$$J(q, a) = 1 + a\,s'(q). \tag{D.77}$$

If $\min_q s'(q) < 0$, the first crossing occurs at

$$a_{\rm sc} = -\frac{1}{\min_q s'(q)}. \tag{D.78}$$

Thus a growing-mode solution can reach a caustic at finite scale factor despite Hubble drag.

At a generic first one-dimensional crossing, the minimum of J touches zero:

$$J(q_c, t_c) = 0, \qquad \partial_q J(q_c, t_c) = 0, \qquad \partial_q^2 J(q_c, t_c) \neq 0. \tag{D.79}$$

Consequently,

$$J(q, t_c) \sim C(q - q_c)^2, \qquad X - X_c \sim C'(q - q_c)^3, \tag{D.80}$$

and mass conservation gives

$$\rho(X, t_c) \sim |X - X_c|^{-2/3}. \tag{D.81}$$

A generic fold after crossing has the exponent $-1/2$. These powers follow from the local geometry of the Lagrangian map. Expansion changes the time and coefficients of the crossing, not its generic singularity type.

The distinction between temporal damping and spatial regularization is important for the loop calculation. Hubble drag slows the growth of density perturbations. The ultraviolet convergence of the GGRW integrals instead follows from their momentum kernels and the initial spectrum. No k^2 smoothing follows from the term $H\mathbf{v}$.

The Layzer–Irvine relation describes the energy balance of self-gravitating matter in an expanding background. Let T denote its peculiar kinetic energy and W its gravitational potential energy relative to the homogeneous background, assuming these quantities are finite or suitably regulated. They satisfy [58]

$$\frac{\mathrm{d}}{\mathrm{d}t}(T + W) + H(2T + W) = 0. \tag{D.82}$$

For attractive gravity, $W < 0$ in the usual bound-system convention. Expansion reduces free peculiar kinetic energy, while gravitational attraction can convert potential energy into peculiar motion. When $2T + W = 0$, the explicit Hubble exchange vanishes at leading order.

I now formulate a corresponding energy criterion for a general PDE written on an expanding background. Let

$$U_{\rm phys}(\mathbf{r}, t) = a^{-\sigma}(t) V(\mathbf{x}, t), \qquad \mathbf{r} = a(t)\mathbf{x}. \tag{D.83}$$

At fixed physical position,

$$\partial_t U_{\rm phys}|_{\mathbf{r}} = a^{-\sigma} \left[\partial_t V|_{\mathbf{x}} - H\mathbf{x} \cdot \nabla_{\mathbf{x}} V - \sigma H V \right]. \tag{D.84}$$

After the homogeneous expansion flow has been absorbed into the comoving variables, an evolution equation may take the form

$$\partial_t V = \mathcal{L}_a(t) V + \mathcal{N}_a(t, V) - H(t) \Sigma V. \tag{D.85}$$

The operator Σ depends on the chosen field variables and their scaling weights. For peculiar fluid velocity, the expansion term is $H\mathbf{v}$. Conformally rescaled variables can instead have no explicit expansion damping.

Suppose the linearized equation admits a time-independent, positive symmetrizer S. Write

$$\|V\|_S^2 = \langle V, SV \rangle \tag{D.86}$$

and assume

$$\begin{aligned} \mathrm{Re}\langle V, S\mathcal{L}_a V\rangle &\le \lambda_a(t)\|V\|_S^2, \\ \mathrm{Re}\langle V, S\Sigma V\rangle &\ge \mu\|V\|_S^2. \end{aligned} \tag{D.87}$$

Taking the energy inner product of Eq. (D.85) then gives

$$\begin{aligned} \frac{1}{2}\frac{\mathrm{d}}{\mathrm{d}t}\|V\|_S^2 \le -[\mu H(t) - \lambda_a(t)]\|V\|_S^2 \\ + \mathrm{Re}\langle V, S\mathcal{N}_a(t,V)\rangle. \end{aligned} \tag{D.88}$$

If S depends on time, the identity acquires the additional term $\frac{1}{2}\langle V, \dot{S}V\rangle$. It must then be included in the linear growth bound.

For a quadratic nonlinearity, suppose the chosen norm also satisfies

$$|\langle V, S\mathcal{N}_a(t,V)\rangle| \le C\|V\|_S^3. \tag{D.89}$$

Define the expansion gap by

$$\gamma(t) = \mu H(t) - \lambda_a(t) > 0. \tag{D.90}$$

The energy inequality gives decay on any time interval where the nonlinear term remains dominated by the linear gap. For example, if $C\|V(t)\|_S \le \gamma(t)/2$ throughout that interval, then

$$\|V(t)\|_S \le \|V(t_0)\|_S \exp\left[-\frac{1}{2}\int_{t_0}^{t}\gamma(s)\,\mathrm{d}s\right]. \tag{D.91}$$

For $\gamma(t)$ proportional to t^{-1}, this gives algebraic decay while the smallness condition is maintained. A positive time-dependent gap alone does not guarantee that the condition persists for all time.

Cosmic expansion weakens gravitational instability without eliminating the growing density mode. In a static homogeneous background, the Jeans instability grows exponentially in time. In EdS, Hubble drag and the decreasing background density convert this instability into algebraic growth, $D_+(t) \propto t^{2/3}$. The resulting evolution has substantially weaker temporal growth, although it is not contractive. This distinction is relevant to quantum algorithms whose complexity depends on the stability and growth of the linear propagator.

After spatial discretization, the same competition may appear in a quadratic system

$$\dot{X} = -[\Lambda_0 + H(t)\Lambda_H]X + B(t)X + Q(X,X). \tag{D.92}$$

If the symmetric part of $\Lambda_0 + H\Lambda_H - B$ has a uniform positive lower bound, the linearized dynamics is contractive in the corresponding norm. Such conditions underlie quantum algorithms for dissipative nonlinear evolution [21, 23]. The EdS growing mode does not satisfy strict contractivity, but its algebraic growth in cosmic time is weaker than the exponential instability in a static self-gravitating background. This distinction motivates investigating whether cosmological expansion permits improved bounds for nonlinear quantum evolution beyond the existing dissipative conditions. The present algorithm takes a separate route by calculating fixed-order statistical coefficients without simulating the full field evolution.

D.4 Euler–Poisson and forced Navier–Stokes singularities

I compare pressureless Euler–Poisson caustics with the reported finite-time blowup of the three-dimensional incompressible Navier–Stokes equations under smooth external forcing [59]. A closely related construction by Alpöge and Buckmaster establishes finite-time blowup for

the three-dimensional incompressible Euler equations with smooth forcing [60]. The latter concerns inviscid evolution, while the former retains positive viscosity. Neither result resolves the unforced Navier–Stokes regularity problem [61]. I focus on the Navier–Stokes construction because its viscous dynamics provides a useful contrast with gravitational Euler–Poisson evolution. Both exhibit concentration on shrinking spatial scales, but their singular variables and conservation constraints differ. The comparison also shows why bounded integrated statistics do not imply pointwise regularity.

For pressureless Euler–Poisson, the Lagrangian identity is

$$\rho(\mathbf{X}(\mathbf{q},t),t)J(\mathbf{q},t)=\rho_0(\mathbf{q}),\qquad J=\det\nabla_{\mathbf{q}}\mathbf{X}. \tag{D.93}$$

A dust caustic occurs when $J\to 0$ in a region carrying mass. The density diverges as the particle-position map loses invertibility.

The forced incompressible Navier–Stokes equations are

$$\begin{aligned}\partial_t\mathbf{u}+(\mathbf{u}\cdot\nabla)\mathbf{u}-\nu\Delta\mathbf{u}+\nabla p&=\mathbf{f},\\ \nabla\cdot\mathbf{u}&=0.\end{aligned} \tag{D.94}$$

For a smooth Lagrangian flow, incompressibility gives

$$\frac{\mathrm{d}}{\mathrm{d}t}\det\nabla_{\mathbf{q}}\mathbf{X}=(\nabla\cdot\mathbf{u})(\mathbf{X},t)\det\nabla_{\mathbf{q}}\mathbf{X}=0,\qquad \det\nabla_{\mathbf{q}}\mathbf{X}=1. \tag{D.95}$$

A Navier–Stokes singularity therefore cannot arise from collapse of the incompressible flow Jacobian.

The construction reported in Ref. [59] starts from zero velocity and uses a smooth compactly supported external force. The solution develops unbounded velocity at finite time while its kinetic energy remains uniformly bounded. Thus the two mechanisms differ at the level of their singular variables:

$$\begin{array}{ll}\text{Euler–Poisson:} & J\to 0,\quad \rho\to\infty,\\ \text{incompressible Navier–Stokes:} & J=1,\quad \|\mathbf{u}\|_{L^\infty}\to\infty.\end{array} \tag{D.96}$$

At a generic first one-dimensional Euler–Poisson caustic, the local geometry derived above gives

$$J\sim(q-q_c)^2,\qquad \rho\sim|X-X_c|^{-2/3}. \tag{D.97}$$

The density divergence reflects compression of mass into a singular Eulerian projection of the Lagrangian sheet.

The forced Navier–Stokes construction instead uses a contracting axisymmetric vortex. Set

$$\tau=1-t. \tag{D.98}$$

In the reported core scaling, the radial and axial lengths behave as

$$\ell_r\asymp\tau^{1/2},\qquad \ell_z\asymp\tau^{1/2-h},\qquad 0<h<10^{-2}, \tag{D.99}$$

while the velocity components have characteristic sizes

$$|u_\theta|,|u_z|\asymp\tau^{-1/2-h},\qquad |u_r|=O(\tau^{-1/2}). \tag{D.100}$$

The core volume scales as $\tau^{3/2-h}$. Consequently, its kinetic-energy scaling is

$$E_{\mathrm{core}}\asymp\tau^{3/2-h}\tau^{-1-2h}=\tau^{1/2-3h}\longrightarrow 0. \tag{D.101}$$

The shrinking core therefore supports divergent pointwise velocity while its kinetic energy tends to zero. This scaling concerns the core alone. The uniform kinetic-energy bound for the complete solution is a separate result of the construction, stated below in Eq. (D.105).

The suppressing mechanisms also differ. In EdS, Hubble drag acts as $H\mathbf{v}$, with no growing strength at large spatial wavenumber. Viscosity instead gives the Fourier damping rate νk^2. The latter suppresses short wavelengths more strongly, but the forced vortex construction organizes a nonlinear concentration despite that smoothing.

The competing terms can be displayed directly:

$$\underbrace{2H\dot{\delta}}_{\text{expansion drag}} \qquad \text{and} \qquad \underbrace{4\pi G\bar{\rho}\,\delta}_{\text{gravitational focusing}} \tag{D.102}$$

in the linear EdS density equation, and

$$\underbrace{\nu\Delta\mathbf{u}}_{\text{viscous smoothing}} \qquad \text{and} \qquad \underbrace{(\mathbf{u}\cdot\nabla)\mathbf{u}}_{\text{nonlinear transport}} \tag{D.103}$$

in Navier–Stokes system. The EdS growing mode is driven by self-gravity. In the forced Navier–Stokes construction, transport and diffusion participate in the concentrating vortex balance.

Using the radial core width ℓ_r as the characteristic length, I define $\mathrm{Re}_\theta = |u_\theta|\ell_r/\nu$ and $\mathrm{Re}_r = |u_r|\ell_r/\nu$. For fixed positive viscosity, the reported core scalings give

$$\mathrm{Re}_\theta \asymp \tau^{-h} \longrightarrow \infty, \qquad \mathrm{Re}_r = O(1). \tag{D.104}$$

The radial Reynolds number remains bounded, so radial transport does not grow relative to radial diffusion by a negative power of τ. The azimuthal Reynolds number diverges, reflecting increasingly rapid rotation at the radial core scale.

The construction satisfies

$$\sup_{0\le t<1} \|\mathbf{u}(t)\|_{L^2} < \infty, \qquad \limsup_{t\uparrow 1} \|\mathbf{u}(t)\|_{L^\infty} = \infty. \tag{D.105}$$

A bounded global quadratic quantity therefore coexists with a pointwise singularity.

Pressureless Euler–Poisson provides a complementary example. Although the density diverges at a caustic, its convolution with a fixed smooth window,

$$\delta_R(\mathbf{x},t) = \int W_R(\mathbf{x}-\mathbf{y})\delta(\mathbf{y},t)\,\mathrm{d}^d y, \tag{D.106}$$

can remain finite when the caustic is locally integrable. Selected moments of this smoothed field can likewise remain finite. Their existence must be established for the specified ensemble and time.

The forced Navier–Stokes result is a constructed instance: the external force is selected together with the solution and is smooth and compactly supported. It establishes a breakdown mechanism in the forced formulation. It does not assert generic blowup for arbitrary forcing or unforced smooth initial data. For the present comparison, the relevant fact is the coexistence of nonlinear concentration and a bounded global energy.

The two calculations both involve quadratic products of short-wavelength fields, but their long-wavelength effects differ. In GGRW, permutation symmetrization cancels the leading hard-pair contributions to a long-wavelength density mode, leaving the inverse-square response of Eq. (D.22). In the forced Navier–Stokes construction, oscillatory velocity corrections have small or vanishing angular mean but generate a nonzero quadratic momentum stress. This

stress is arranged to cancel the singular residual of the concentrating background flow [59]. The first mechanism suppresses the density response, while the second uses a nonzero mean stress to support the constructed flow.

The relevant properties are collected below.

	Pressureless Euler–Poisson	Forced incompressible Navier–Stokes
Constraint	Compressible mass transport	$\nabla \cdot \mathbf{u} = 0$
Jacobian	$J \to 0$ at shell crossing	$J = 1$ while smooth
Singular quantity	Density and inverse Jacobian	Velocity and its gradients
Suppressing mechanism	Hubble drag in EdS	Viscosity
Short-scale damping	No k^2 damping from $H\mathbf{v}$	Parabolic k^2 damping
Integrated control	Selected smoothed statistics can remain finite	Kinetic energy remains bounded
Concentration	Gravitational focusing	Contracting vortex
Short-scale coupling	Hard-pair decoupling	Oscillatory mean stress

These examples place a restriction on the interpretation of statistical algorithms. A finite smoothed observable need not imply a regular underlying field. The fixed-order theorem computes coefficients defined by the specified convergent integrals on the chosen solution branch. Continuation through a caustic or a dynamical blowup requires additional evolution data and does not follow from the existence of those coefficients.

E Random-wave Schrödinger equations and cancellation between diagrams

I apply the perturbative averaging method to nonlinear dispersive waves with random initial conditions. The cubic nonlinear Schrödinger equation provides a useful example because its interaction kernels contain oscillatory phases, and its statistical evolution involves cancellations between distinct perturbative diagrams [62].

Consider

$$\mathrm{i}\partial_t \psi = -\Delta\psi + g|\psi|^2\psi \tag{E.1}$$

on a periodic box of side length L in d spatial dimensions. I prescribe the initial Fourier amplitudes by

$$\psi(\mathbf{x}, 0) = \sum_{\mathbf{k}} \xi_{\mathbf{k}} \exp(\mathrm{i}\mathbf{k}\cdot\mathbf{x}), \qquad \mathbf{k} \in \frac{2\pi}{L}\mathbb{Z}^d. \tag{E.2}$$

The amplitudes are independent centered complex Gaussian variables with

$$\mathbb{E}[\xi_{\mathbf{k}}\overline{\xi}_{\mathbf{k}'}] = n_0(\mathbf{k})\delta_{\mathbf{k},\mathbf{k}'}, \qquad \mathbb{E}[\xi_{\mathbf{k}}\xi_{\mathbf{k}'}] = 0. \tag{E.3}$$

Here $n_0(\mathbf{k})$ is the initial wave-action spectrum. I impose a finite Fourier–Galerkin cutoff, projecting the cubic interaction onto the retained modes, and absorb the Fourier volume normalization into g. I calculate ensemble averages from the perturbative expansion and Gaussian contractions, without sampling initial fields or evolving individual realizations.

The linear frequency is $\omega_{\mathbf{k}} = |\mathbf{k}|^2$. I remove the linear oscillation by defining

$$a_{\mathbf{k}}(t) = \exp(\mathrm{i}|\mathbf{k}|^2 t)\psi_{\mathbf{k}}(t). \tag{E.4}$$

The interaction-picture equation becomes

$$\partial_t a_{\mathbf{k}} = -\mathrm{i}g \sum_{\mathbf{k}_1-\mathbf{k}_2+\mathbf{k}_3=\mathbf{k}} \exp(\mathrm{i}t\Omega) \times a_{\mathbf{k}_1}\overline{a}_{\mathbf{k}_2}a_{\mathbf{k}_3}, \tag{E.5}$$

where

$$\Omega = |\mathbf{k}|^2 - |\mathbf{k}_1|^2 + |\mathbf{k}_2|^2 - |\mathbf{k}_3|^2, \qquad \mathbf{k} = \mathbf{k}_1 - \mathbf{k}_2 + \mathbf{k}_3. \tag{E.6}$$

Four-wave resonance occurs when momentum conservation holds and $\Omega = 0$.

Expand

$$a_{\mathbf{k}}(t) = \sum_{r=0}^{\infty} g^r a_{\mathbf{k}}^{[r]}(t), \qquad a_{\mathbf{k}}^{[0]} = \xi_{\mathbf{k}}. \tag{E.7}$$

At first order,

$$a_{\mathbf{k}}^{[1]}(T) = -\mathrm{i} \sum_{\mathbf{k}_1-\mathbf{k}_2+\mathbf{k}_3=\mathbf{k}} \Phi_T(\Omega) \times \xi_{\mathbf{k}_1}\overline{\xi}_{\mathbf{k}_2}\xi_{\mathbf{k}_3}, \tag{E.8}$$

with the time integral

$$\Phi_T(\Omega) = \int_0^T \exp(\mathrm{i}s\Omega)\,\mathrm{d}s = T\exp(\mathrm{i}\Omega T/2)\,\mathrm{sinc}(\Omega T/2). \tag{E.9}$$

I use $\mathrm{sinc}(x) = \sin(x)/x$ with $\mathrm{sinc}(0) = 1$.

The exact time integral is analytic at resonance. Its expansion is

$$\Phi_T(\Omega) = T + \frac{\mathrm{i}\Omega T^2}{2} - \frac{\Omega^2 T^3}{6} + O(|\Omega|^3 T^4). \tag{E.10}$$

The alternative expression

$$\Phi_T(\Omega) = \frac{\exp(\mathrm{i}\Omega T) - 1}{\mathrm{i}\Omega} \tag{E.11}$$

has a removable denominator. Evaluating the complete factor avoids a false resonance pole and the loss of precision associated with subtracting nearly equal exponentials.

Differentiation under the time integral gives

$$\left|\frac{\mathrm{d}^j \Phi_T}{\mathrm{d}\Omega^j}\right| = \left|\int_0^T (\mathrm{i}s)^j \exp(\mathrm{i}s\Omega)\,\mathrm{d}s\right| \le \frac{T^{j+1}}{j+1}. \tag{E.12}$$

The estimate establishes regularity with respect to Ω at fixed T. It does not bound momentum derivatives of $\Phi_T(\Omega)$, since the frequency mismatch is quadratic in the interacting momenta and its momentum derivatives can grow with the Fourier cutoff. The derivative estimates required by the quantum integration algorithm must therefore be established for the complete contracted integrand. Moreover, the bound grows as T^{j+1} and is not uniform on kinetic time scales.

I calculate the wave-action spectrum

$$n_T(\mathbf{k}) = \mathbb{E}|a_{\mathbf{k}}(T)|^2. \tag{E.13}$$

At first order in g, it contains

$$2g\ \mathrm{Re}\,\mathbb{E}[\overline{\xi}_{\mathbf{k}} a_{\mathbf{k}}^{[1]}(T)]. \tag{E.14}$$

Wick's theorem gives

$$\begin{aligned}&\mathbb{E}[\overline{\xi}_{\mathbf{k}}\xi_{\mathbf{k}_1}\overline{\xi}_{\mathbf{k}_2}\xi_{\mathbf{k}_3}]\\&\quad= n_0(\mathbf{k})n_0(\mathbf{k}_2)\left[\delta_{\mathbf{k},\mathbf{k}_1}\delta_{\mathbf{k}_2,\mathbf{k}_3}+\delta_{\mathbf{k},\mathbf{k}_3}\delta_{\mathbf{k}_2,\mathbf{k}_1}\right].\end{aligned}\tag{E.15}$$

Both pairings impose $\Omega = 0$. Hence

$$\mathbb{E}[\overline{\xi}_{\mathbf{k}}a_{\mathbf{k}}^{[1]}(T)] = -2\mathrm{i}Tn_0(\mathbf{k})\sum_{\mathbf{p}} n_0(\mathbf{p}).\tag{E.16}$$

This expression is purely imaginary. The first-order correction to the wave-action spectrum therefore vanishes, although the first-order field itself is nonzero.

At second order,

$$\begin{aligned}n_T(\mathbf{k}) &= n_0(\mathbf{k})\\&\quad+ g^2\left[\mathbb{E}|a_{\mathbf{k}}^{[1]}(T)|^2 + 2\,\mathrm{Re}\,\mathbb{E}[\overline{\xi}_{\mathbf{k}}a_{\mathbf{k}}^{[2]}(T)]\right] + O(g^3).\end{aligned}\tag{E.17}$$

The second-order field follows directly from the interaction equation:

$$\begin{aligned}a_{\mathbf{k}}^{[2]}(T) = -\mathrm{i}\sum_{\mathbf{k}_1-\mathbf{k}_2+\mathbf{k}_3=\mathbf{k}}&\int_0^T \mathrm{d}s\,\exp(\mathrm{i}s\Omega)\\&\times\Big[a_{\mathbf{k}_1}^{[1]}(s)\overline{\xi}_{\mathbf{k}_2}\xi_{\mathbf{k}_3} + \xi_{\mathbf{k}_1}\overline{a_{\mathbf{k}_2}^{[1]}(s)}\xi_{\mathbf{k}_3}\\&\qquad+\xi_{\mathbf{k}_1}\overline{\xi}_{\mathbf{k}_2}a_{\mathbf{k}_3}^{[1]}(s)\Big].\end{aligned}\tag{E.18}$$

The term $\mathbb{E}|a_{\mathbf{k}}^{[1]}|^2$ pairs two first-order interaction trees. The term $\mathbb{E}[\overline{\xi}_{\mathbf{k}}a_{\mathbf{k}}^{[2]}]$ pairs a second-order tree with the initial field. Each expectation contains six initial Gaussian amplitudes and reduces to products of three covariances.

These two contributions are linked by particle-number conservation. For real g, the Fourier-truncated Hamiltonian evolution conserves

$$\mathcal{N} = \sum_{\mathbf{k}}|a_{\mathbf{k}}(T)|^2 = \sum_{\mathbf{k}}|\xi_{\mathbf{k}}|^2.\tag{E.19}$$

Expanding this identity through order g^2 gives

$$\sum_{\mathbf{k}}\left[|a_{\mathbf{k}}^{[1]}(T)|^2 + 2\,\mathrm{Re}\left(\overline{\xi}_{\mathbf{k}}a_{\mathbf{k}}^{[2]}(T)\right)\right] = 0.\tag{E.20}$$

This identity holds for every initial realization. Taking its Gaussian expectation yields

$$\begin{aligned}\sum_{\mathbf{k}}\Big[&\mathbb{E}|a_{\mathbf{k}}^{[1]}(T)|^2\\&+2\,\mathrm{Re}\,\mathbb{E}[\overline{\xi}_{\mathbf{k}}a_{\mathbf{k}}^{[2]}(T)]\Big] = 0.\end{aligned}\tag{E.21}$$

The positive first term is canceled by contributions from the second after summation over external momenta. Individual modes can gain or lose wave action, but their total is conserved. This exact identity provides a check on the diagram weights and signs. It does not by itself establish the stronger cancellations needed to control high-order diagrams at long times.

The long-time behavior follows from the same finite-time interaction factor. In a continuous frequency variable,

$$\frac{|\Phi_T(\Omega)|^2}{T} = T\,\mathrm{sinc}^2(\Omega T/2) \;\longrightarrow\; 2\pi\delta(\Omega)\tag{E.22}$$

in the distributional sense as $T \to \infty$. The resonance profile narrows while its peak grows. Thus regularity at each finite time does not provide uniform derivative bounds as T increases.

In the standard weak-coupling scaling, the kinetic time is proportional to g^{-2}, together with an appropriate large-box limit. Rigorous derivations of wave kinetic theory organize the high-order paired interaction diagrams into families whose leading large contributions cancel. Their results also describe higher Fourier moments and the wave kinetic hierarchy under the corresponding scaling assumptions [37,39,40]. These results concern a coupled long-time limit, whereas the present theorem fixes the observation time and perturbative order.

The GGRW hard-pair estimate follows from permutation symmetrization of the gravitational density kernels, which gives

$$F_r^{(s)}(\mathbf{k}_1, \ldots, \mathbf{k}_{r-2}, \mathbf{p}, -\mathbf{p}) = O(|\mathbf{p}|^{-2}), \qquad |\mathbf{p}| \to \infty \tag{E.23}$$

at the explicitly established kernel orders. Leading hard-momentum terms cancel within a symmetrized density kernel. Gravitational perturbation theory also has cross-diagram infrared cancellations between P_{22} and P_{13}, so the two mechanisms are not exclusive. The cubic NLS vertex has no analogous inverse-square hard-pair suppression. Its higher-order paired diagrams involve distinct time integrations, oscillatory phases, and combinatorial weights whose cancellations require the analysis of complete diagram families. The second-order particle-number identity above demonstrates cancellation only after summing over external momenta. It does not establish the corresponding bounds for individual mode statistics needed in the kinetic-limit analysis.

For numerical integration, I combine the relevant diagram contributions with their exact weights before estimating absolute values or derivatives. The completed sum determines the integrand supplied to the quantum circuit. Its evaluation cost includes constructing the diagram family and computing the combined time-oscillation factors.

At fixed Fourier cutoff, Gaussian averaging produces finite momentum sums rather than the smooth integrals considered in Appendix B. Quantum summation can be applied to these sums under suitable coherent evaluation and state-preparation assumptions. For continuum integrals, the fixed-order Sobolev integration theorem additionally requires convergence, appropriate coordinate transformations, and bounded momentum derivatives of the completed diagram sums. These conditions must be established independently of the regularity of the finite-time resonance factor. The computational cost includes diagram construction and reversible evaluation of the oscillatory terms. Uniform estimates on kinetic time scales require further analysis beyond the fixed-order theorem.

F Non-Gaussian initial data, errors, and computational costs

I extend the fixed-order calculation to non-Gaussian initial fields and examine the additional costs of perturbative truncation, numerical accuracy, and graph construction. I then compare the complete resource requirements with those of other methods for computing nonlinear statistical observables.

F.1 Non-Gaussian initial data and error control

For Gaussian initial data, Wick's theorem expresses every higher moment in terms of the two-point covariance. A non-Gaussian distribution instead has independent higher connected correlations. I specify these correlations through the finite order required by the perturbative calculation.

Let $\xi_a(\mathbf{x})$ be a centered, translation-invariant random field. Define its connected Fourier correlations by

$$\begin{aligned}&\left\langle \widehat{\xi}_{a_1}(\mathbf{k}_1)\cdots\widehat{\xi}_{a_s}(\mathbf{k}_s)\right\rangle_c \\ &\qquad = (2\pi)^d\delta^{(d)}\left(\sum_{j=1}^{s}\mathbf{k}_j\right)C^{(s)}_{a_1\cdots a_s}(\mathbf{k}_1,\ldots,\mathbf{k}_{s-1}).\end{aligned} \tag{F.1}$$

Here $C^{(s)}$ is the connected s-point spectrum. Translation invariance fixes the final momentum through the delta function. For Gaussian data, $C^{(s)} = 0$ for $s > 2$.

Ordinary moments follow from the moment-cumulant identity. For random variables X_1,..., X_m,

$$\mathbb{E}\left[\prod_{j=1}^{m}X_j\right] = \sum_{\pi\in\Pi_m}\prod_{B\in\pi}\kappa(X_j : j\in B), \tag{F.2}$$

where Π_m denotes the partitions of $\{1,\ldots,m\}$ and $\kappa(X_j : j \in B)$ is the joint cumulant associated with block B. For Gaussian data, only blocks containing two labels survive, reproducing Wick's theorem. For non-Gaussian data, each block supplies a connected initial spectrum and its momentum-conserving delta function. The interaction vertices impose further momentum constraints. Assuming the required initial moments exist, the fixed-order expansion at finite momentum regulators therefore reduces to a finite sum of deterministic momentum and time integrals.

The number of initial fields determines how many connected spectra are needed. For an observable of degree n, a polynomial evolution equation with maximal interaction degree p, and a total of K interaction vertices, the number of initial leaves is bounded by

$$m_{\max} = n + K(p-1). \tag{F.3}$$

Thus the initial connected spectra through order $m_{\max}$ suffice. Since the initial field is centered, partitions containing singleton blocks vanish.

The higher connected spectra introduce additional momentum dependence. Their infrared, ultraviolet, and partial-momentum limits must be combined with those of the interaction kernels. After the necessary diagram sums and momentum transformations, the resulting integrands are subject to the same Sobolev regularity conditions as in Appendix A. Their evaluation circuits include the required $C^{(s)}$ factors.

The main theorem calculates fixed perturbative coefficients. Computing the complete nonlinear observable also requires control of the remainder. Using the formal interaction parameter z, write

$$Q(z) = \sum_{r=0}^{\infty} z^r Q_r, \tag{F.4}$$

with the prescribed physical value $z = 1$. Suppose a separate analysis establishes

$$\left|Q(1) - \sum_{r=0}^{K} Q_r\right| \le A\rho^{K+1}, \qquad 0 < \rho < 1, \tag{F.5}$$

where A and ρ are independent of K on the stated parameter and time interval. To reduce the remainder below $\epsilon/2$, it suffices to choose

$$K + 1 \ge \frac{\log(2A/\epsilon)}{\log(1/\rho)}. \tag{F.6}$$

For fixed A and ρ,

$$K = O(\log \epsilon^{-1}). \tag{F.7}$$

The remainder estimate is a property of the nonlinear dynamics and the chosen observable. It must be proved independently of the fixed-order integration theorem. In particular, no bound of the form Eq. (F.5) has been established here for the GGRW perturbative series. The logarithmic truncation order in Eq. (F.7) is therefore conditional and does not constitute a complexity bound for the complete cosmological observable. Near a singularity or over a sufficiently long time, the constants in Eq. (F.5) may deteriorate. Increasing K also increases the number of interaction trees and initial cumulant partitions. Both effects enter the cost of approximating the complete nonlinear statistic.

For one fixed coefficient, I separate numerical errors according to their origin.

$$\begin{aligned}\epsilon_{\mathrm{num}} \le{}& \epsilon_{\mathrm{input}} + \epsilon_{\mathrm{pre}} + \epsilon_{\mathrm{coarse}} + \epsilon_{\mathrm{grid}} \\ &+ \epsilon_{\mathrm{eval}} + \epsilon_{\mathrm{AE}} + \epsilon_{\mathrm{gate}}.\end{aligned} \tag{F.8}$$

The input error covers approximations to the prescribed initial spectra, propagators, and interaction coefficients. The preprocessing error covers approximations introduced in constructing the integral representation, such as truncated local expansions or numerical coordinate maps. Exact algebraic contractions and changes of variables introduce no such error.

The coarse error comes from finite-precision construction and integration of the classical interpolant and any classically integrated control term introduced below. The grid error comes from midpoint discretization of the residual integral. The evaluation error measures the bias caused by computing the residual integrand to finite precision. Amplitude estimation and approximate quantum gates contribute the final two terms. Appendix B bounds these contributions separately. In particular, reusing a reversible finite-precision function does not accumulate its numerical bias with the number of quantum queries.

When the target is the full nonlinear observable, the perturbative remainder adds

$$\epsilon_{\mathrm{pert}} = \left| Q(1) - \sum_{r=0}^{K} Q_r \right|. \tag{F.9}$$

If ϵ_r bounds the numerical error in the computed coefficient Q_r, then

$$\epsilon_{\mathrm{total}} \le \epsilon_{\mathrm{pert}} + \sum_{r=0}^{K} \epsilon_r. \tag{F.10}$$

I allocate the tolerances for the individual coefficients according to this inequality.

Known analytic contributions can reduce the numerical integration cost. Write

$$f = f_{\mathrm{ctrl}} + f_{\mathrm{res}}. \tag{F.11}$$

I integrate f_{ctrl} analytically or by a classical method and apply the quantum integration algorithm to f_{res}. The known contribution may come from an endpoint expansion, an exactly integrable term, a low-rank approximation, or a spectral representation.

If the control-function remainder satisfies

$$\|f_{\mathrm{res}}\|_{W^r_\infty} \le M_{\mathrm{res}}, \tag{F.12}$$

the combined classical and coherent function-evaluation count of Appendix B becomes

$$N_{\mathrm{tot}}(f_{\mathrm{res}}) = O_{D,r}\left[\max\left\{ 1, \left(\frac{M_{\mathrm{res}}}{\epsilon} \right)^{D/(D+r)} \right\} \right]. \tag{F.13}$$

The subtraction can improve the derivative norm and remove difficult endpoint terms. Its construction and classical integration costs remain part of the total computation.

F.2 Preprocessing and computational comparisons

I first quantify the work needed to construct a fixed-order coefficient. For quadratic dynamics, Appendix A bounds the number of ordered interaction-tree tuples and Gaussian pairings. For even $K+n$, their product satisfies

$$N_{\mathrm{raw}}(K,n) \le \binom{K+n-1}{n-1} 4^K (K+n-1)!!. \tag{F.14}$$

For odd $K+n$, the Gaussian expectation vanishes. The displayed count precedes component-index summations, symmetry reduction, and identification of equivalent diagrams. Let $C_{\mathrm{term}}(K, n; \mathcal{I}, b)$ bound the arithmetic work allotted per contracted term in a direct enumeration, including component contractions, formula construction, and the grouping and simplification needed to preserve cancellations. For quadratic evolution, direct enumeration then gives

$$C_{\mathrm{pre}}(K,n;\mathcal{I},b) \le N_{\mathrm{graph}}(K,n) C_{\mathrm{term}}(K,n;\mathcal{I},b), \tag{F.15}$$

where $\mathcal{I}$ specifies the PDE coefficients, initial distribution, and regulators, while b denotes the arithmetic precision.

Equation (F.14) is deliberately conservative. Symmetries, equivalent diagrams, recursive evaluation, and cancellation identities can reduce the number of expressions that must be computed. Their implementation costs must nevertheless be included in preprocessing. For fixed K and n, the combinatorial factor is independent of ϵ. Under the separate geometric remainder hypothesis of Eq. (F.5), one may choose $K = O(\log \epsilon^{-1})$. The factorial growth of Wick pairings then contributes to the accuracy-dependent preprocessing cost. The quantum integration exponent alone does not control this growth.

I also account for converting raw moments into connected correlations. For a scalar random variable X, the cumulant is

$$\kappa_n(X) = \sum_{\pi \in \Pi_n} (|\pi|-1)!(-1)^{|\pi|-1} \prod_{B \in \pi} \mathbb{E}[X^{|B|}]. \tag{F.16}$$

This formula combines complete moments. At fixed perturbative order, I must also distribute the interaction order among the factors. For each block B of a partition π, let

$$M_{B,j} = [z^j]\, \mathbb{E}\left[\prod_{i \in B} X_i(z)\right] \tag{F.17}$$

denote the order-j coefficient of the moment associated with that block. The connected n-point coefficient at order K is

$$\kappa_n^{[K]} = \sum_{\pi \in \Pi_n} (|\pi|-1)!(-1)^{|\pi|-1} \cdot \sum_{\substack{K_B \ge 0 \ (B \in \pi) \\ \sum_{B \in \pi} K_B = K}} \prod_{B \in \pi} M_{B,K_B}. \tag{F.18}$$

Here $X_i(z)$ denotes the ith measured field or observable with the same formal interaction parameter z. This convolution of perturbative orders is necessary when constructing a connected coefficient from separately computed moments. For fixed n and K, the partitions and order assignments are finite. Numerical errors propagate through the corresponding polynomial combination. I choose moment tolerances using bounds on the moments and on the coefficients of that polynomial.

The resulting computational target differs from direct simulation of random-field realizations. A trajectory method samples the initial distribution, evolves the full discretized field,

and averages the requested observable. Its cost includes state generation, time evolution, and statistical sampling. The present method performs the statistical contractions before numerical integration and calculates the specified perturbative coefficients without constructing individual evolved realizations.

Other quantum algorithms for nonlinear evolution employ several representations. Carleman embeddings treat polynomial nonlinearities through enlarged linear systems [21–23], while Liouville, Koopman, and level-set methods reformulate classical dynamics in linear equations [25, 26]. Nonlinear unitary dynamics has also been examined through quantum and randomized classical algorithms [27]. For uncertainty quantification, Golse, Jin, and Liu encode uncertain PDE inputs in enlarged deterministic systems [28]. Quantum algorithms for stochastic nonlinear evolution also target statistical observables, including low-order correlation functions [29–31]. Their formulations incorporate noise and dissipation in the dynamics, whereas the present work treats deterministic nonlinear evolution with Gaussian random initial data. I evaluate fixed-order statistical coefficients by applying Wick's theorem before numerical integration. The computational costs then depend on diagram construction, derivative bounds, and reversible evaluation of the resulting deterministic integrands. A meaningful comparison requires the same observables, input assumptions, time intervals, and accuracy. For linear matrix evolution, Simon, Berry, and Somma [20] directly compute selected matrix entries and establish end-to-end quantum complexity bounds. Their approach further illustrates the importance of specifying the desired observable rather than the full evolved state.

The quantum query exponent established in Appendix B is optimal for the ambient smooth-function integration class [33, 34]. The randomized classical integration bound derived in Appendix B.1 provides the corresponding general comparison. Integrands generated by a particular PDE occupy a more restricted family whose symmetries and analytic structure may support faster classical methods. In cosmology, rotational reduction and specialized convolution algorithms such as FAST-PT and FFTLog exploit this additional structure [35,36]. An end-to-end comparison must therefore include these classical methods under the same physical input and accuracy requirements (See [63] for careful comparison between oracle speedups and end-to-end algorithmic advantages).

The full cost is recorded through the resource accounting of Eq. (B.59). In a common elementary-operation cost model, it has the schematic decomposition

$$C_{\text{total}} = C_{\text{pre}} + C_{\text{cert}} + C_{\text{coarse}} + C_{\text{quantum}}, \tag{F.19}$$

where the terms represent construction of the integrals, derivative certification, classical coarse integration, and quantum residual estimation. The quantum contribution includes reversible integrand evaluation and amplitude estimation. At fixed perturbative order, this gives a finite-dimensional algorithm for specified statistical coefficients. Extending it to the complete nonlinear observable requires control of the perturbative remainder and the growing diagram count. Its comparison with classical algorithms must include the same preprocessing and numerical accuracy requirements.

References

[1] V. F. Mukhanov and G. V. Chibisov, "Quantum fluctuations and a nonsingular universe," *JETP Lett.* **33**, 532–535 (1981).

[2] A. H. Guth and S.-Y. Pi, "Fluctuations in the new inflationary universe," *Phys. Rev. Lett.* **49**, 1110–1113 (1982).

[3] S. W. Hawking, "The development of irregularities in a single bubble inflationary universe," *Phys. Lett. B* **115**, 295–297 (1982).

[4] A. A. Starobinsky, "Dynamics of phase transition in the new inflationary universe scenario and generation of perturbations," *Phys. Lett. B* **117**, 175–178 (1982).

[5] A.A. Starobinsky, "Stochastic de Sitter (inflationary) stage in the early universe," *Field Theory, Quantum Gravity and Strings*, 107-126, Berlin, Heidelberg: Springer Berlin Heidelberg (1986).

[6] S.-J. Rey, "Dynamics of inflationary phase transition," Nucl. Phys. B **284**, 706-728 (1986).

[7] M. H. Goroff, B. Grinstein, S.-J. Rey, and M. B. Wise, "Coupling of modes of cosmological mass density fluctuations," *Astrophys. J.* **311**, 6–14 (1986).

[8] J.N. Fry, "The Galaxy correlation hierarchy in perturbation theory," *Astrophys. J.* **279**, 499-510 (1984).

[9] F. Bernardeau, S. Colombi, E. Gaztañaga, and R. Scoccimarro, "Large-scale structure of the Universe and cosmological perturbation theory," *Phys. Rep.* **367**, 1–248 (2002).

[10] R. Courant, and D. Hilbert. *Methods of Mathematical Physics, vol. II. Partial differential equations*, Wiley Pub. Co. (1963).

[11] L. C. Evans, *Partial Differential Equations*, 2nd ed., Graduate Studies in Mathematics **19**, American Mathematical Society (2010).

[12] F. Villaescusa-Navarro et al., "The Quijote simulations," *Astrophys. J. Suppl. Ser.* **250**, 2 (2020).

[13] N. A. Maksimova, L. H. Garrison, D. J. Eisenstein, B. Hadzhiyska, S. Bose, and T. P. Satterthwaite, "AbacusSummit: a massive set of high-accuracy, high-resolution N-body simulations," *Mon. Not. R. Astron. Soc.* **508**, 4017–4037 (2021).

[14] K. Toyoizumi, N. Yamamoto, and K. Hoshino, "Hamiltonian simulation using the quantum singular-value transformation: Complexity analysis and application to the linearized Vlasov-Poisson equation," *Phys. Rev. A* **109**, 012430 (2024).

[15] K. Miyamoto, S. Yamazaki, F. Uchida, K. Fujisawa, and N. Yoshida, "Quantum algorithm for the Vlasov simulation of the large-scale structure formation with massive neutrinos," *Phys. Rev. Research* **6**, 013200 (2024).

[16] T. Vaszary, A. Datta, T. Goffrey, and B. Appelbe, "Solving the nonlinear Vlasov equation on a quantum computer," *Quantum* **10**, 2206 (2026).

[17] M. Christensen, T. Goffrey, and A. Datta, "Improved convergence of Carleman-embedded quantum algorithm for the Vlasov-Poisson System," arXiv:2607.28426 (2026).

[18] D. W. Berry, A. M. Childs, A. Ostrander, and G. Wang, "Quantum algorithm for linear differential equations with exponentially improved dependence on precision," *Commun. Math. Phys.* **356**, 1057–1081 (2017), doi:10.1007/s00220-017-3002-y.

[19] D. W. Berry and P. C. S. Costa, "Quantum algorithm for time-dependent differential equations using Dyson series," *Quantum* **8**, 1369 (2024), doi:10.22331/q-2024-06-13-1369.

[20] S. Simon, D. W. Berry, and R. D. Somma, "Efficient quantum algorithm for linear matrix differential equations and applications to open quantum systems," arXiv:2605.16195 (2026).

[21] J.-P. Liu, H. Ø. Kolden, H. K. Krovi, N. F. Loureiro, K. Trivisa, and A. M. Childs, "Efficient quantum algorithm for dissipative nonlinear differential equations," *Proc. Natl. Acad. Sci. USA* **118**, e2026805118 (2021).

[22] A. Engel, G. Smith, and S. E. Parker, "Linear embedding of nonlinear dynamical systems and prospects for efficient quantum algorithms," *Phys. Plasmas* **28**, 062305 (2021).

[23] H. Krovi, "Improved quantum algorithms for linear and nonlinear differential equations," *Quantum* **7**, 913 (2023).

[24] P.C.S. Costa, P. Schleich, M. Morales, and W. Berry, "Further improving quantum algorithms for nonlinear differential equations via higher-order methods and rescaling" NPJ Quant. Info. **11** (2025): 141.

[25] S. Jin, N. Liu, and Y. Yu, "Time complexity analysis of quantum algorithms via linear representations for nonlinear ordinary and partial differential equations," *J. Comput. Phys.* **487**, 112149 (2023).

[26] S. Jin and N. Liu, "Quantum algorithms for nonlinear partial differential equations," *Bull. Sci. Math.* **194**, 103457 (2024).

[27] N. Brüstle and N. Wiebe, "Quantum and classical algorithms for nonlinear unitary dynamics," *Quantum* **9**, 1741 (2025).

[28] F. Golse, S. Jin, and N. Liu, "Quantum algorithms for uncertainty quantification: Applications to partial differential equations," *Sci. China Phys. Mech. Astron.* **68**, 104704 (2025).

[29] S. Bravyi, R. Manson-Sawko, M. Zayats, and S. Zhuk, "Quantum simulation of a noisy classical nonlinear dynamics," arXiv:2507.06198v2 (2025).

[30] X. Li, A.B. Catli, H.K. Lim, M. Pocrnic, D. An, J.-P. Liu, and Na. Wiebe, "Efficient quantum simulation for nonlinear stochastic differential equations," arXiv:2603.12398 (2026).

[31] S. Bravyi, A. Byrne, M. Zayats, and S. Zhuk, "Quantum algorithms for stochastic nonlinear differential equations," arXiv:2606.08349 (2026).

[32] N. S. Bakhvalov, "On the approximate calculation of integrals," *Vestnik Moskov. Univ., Ser. Mat. Mekh. Astron. Fiz. Khim.* **4**, 3–18 (1959).

[33] E. Novak, "Quantum Complexity of Integration," *J. Complexity* **17**, 2–16 (2001), arXiv:quant-ph/0008124.

[34] S. Heinrich, "Quantum integration in Sobolev classes," *J. Complexity* **19**, 19–42 (2003), arXiv:quant-ph/0112153.

[35] J. E. McEwen, X. Fang, C. M. Hirata, and J. A. Blazek, "FAST-PT: a novel algorithm to calculate convolution integrals in cosmological perturbation theory," *JCAP* **09**, 015 (2016), arXiv:1603.04826.

[36] M. Simonović, T. Baldauf, M. Zaldarriaga, J. J. Carrasco, and J. A. Kollmeier, "Cosmological perturbation theory using the FFTLog: formalism and connection to QFT loop integrals," *JCAP* **04**, 030 (2018), arXiv:1708.08130.

[37] Y. Deng and Z. Hani, "Derivation of the wave kinetic equation: full range of scaling laws," *Memoirs of the American Mathematical Society* **320**(1631) (2026), arXiv:2301.07063.

[38] N. Makino, M. Sasaki, and Y. Suto, "Analytic approach to the perturbative expansion of nonlinear gravitational fluctuations in cosmological density and velocity fields," *Phys. Rev. D* **46**, 585–602 (1992).

[39] Y. Deng and Z. Hani, "Full derivation of the wave kinetic equation," *Inventiones Mathematicae* **233**, 543–724 (2023), arXiv:2104.11204.

[40] Y. Deng and Z. Hani, "Propagation of chaos and higher order statistics in wave kinetic theory," *J. Eur. Math. Soc.* **28**, 673–733 (2026).

[41] A. A. Abolhasani, M. Mirbabayi, and E. Pajer, "Systematic renormalization of the effective theory of large scale structure," *JCAP* **05**, 063 (2016), arXiv:1509.07886.

[42] D. Blas, M. Garny, and T. Konstandin, "Cosmological perturbation theory at three-loop order," *JCAP* **01**, 010 (2014), arXiv:1309.3308.

[43] C. Bogner and S. Weinzierl, "Resolution of singularities for multi-loop integrals," *Comput. Phys. Commun.* **178**, 596–610 (2008), arXiv:0709.4092.

[44] S. Heinrich, "Quantum summation with an application to integration," *J. Complexity* **18**, 1–50 (2002).

[45] G. Brassard, P. Høyer, M. Mosca, and A. Tapp, "Quantum amplitude amplification and estimation," *Contemp. Math.* **305**, 53–74 (2002).

[46] D. Grinko, J. Gacon, C. Zoufal, and S. Woerner, "Iterative quantum amplitude estimation," *NPJ Quantum Information* **7**, 52 (2021).

[47] A. Montanaro, "Quantum speedup of Monte Carlo methods," *Proc. R. Soc. A* **471**, 20150301 (2015).

[48] Y. Hamoudi, "Quantum sub-Gaussian mean estimator," *LIPIcs ESA* **204**, 50:1–50:17 (2021).

[49] D. Gottlieb and S. A. Orszag, *Numerical Analysis of Spectral Methods: Theory and Applications*, SIAM, Philadelphia (1977).

[50] L.N. Trefethen, *Spectral Methods in MATLAB*, (2000, Society for Industrial and Applied Mathematics).

[51] J. P. Boyd, *Chebyshev and Fourier Spectral Methods*, 2nd ed., Dover, New York (2001).

[52] C. Canuto, M. Y. Hussaini, A. Quarteroni, and T. A. Zang, *Spectral Methods: Fundamentals in Single Domains*, Springer, Berlin (2006).

[53] M. Fasiello, T. Fujita, and Z. Vlah, "Perturbation theory of large scale structure in the ΛCDM Universe. Exact time evolution and the two-loop power spectrum," *Phys. Rev. D* **106**, 123504 (2022).

[54] J. J. M. Carrasco, S. Foreman, D. Green, and L. Senatore, "The 2-loop matter power spectrum and the IR-safe integrand," *JCAP* **07**, 057 (2014), arXiv:1304.4946.

[55] X. Gu and Z. Lei, "Local well-posedness of the three dimensional compressible Euler–Poisson equations with physical vacuum," arXiv:1405.4612 (2014).

[56] S. Engelberg, H. Liu, and E. Tadmor, "Critical thresholds in Euler–Poisson equations," arXiv:math/0112014 (2001).

[57] Y.-P. Choi, D.-H. Kim, D. Koo, and E. Tadmor, "Critical thresholds in pressureless Euler–Poisson equations with background states," arXiv:2402.12839 (2024).

[58] P. P. Avelino and A. Barreira, "Layzer–Irvine equation: new perspectives and the role of interacting dark energy," arXiv:1112.0417 (2011).

[59] OpenAI, "Finite Time Blowup for Navier–Stokes," preprint (2026), `https://cdn.openai.com/pdf/32d9f210-8b73-45e0-91bc-82a30aef8a9a/navier-stokes.pdf`.

[60] L. Alpöge and T. Buckmaster, "Finite-time blowup for the 3D incompressible Euler equations with smooth forcing," preprint (2026), `https://cims.nyu.edu/~tristanb/euler.pdf`.

[61] C. L. Fefferman, "Existence and Smoothness of the Navier–Stokes Equation," in *The Millennium Prize Problems*, Clay Mathematics Institute (2006), `https://www.claymath.org/millennium/Navier-Stokes-Equation/`.

[62] Y. Deng and Z. Hani, "On the derivation of the wave kinetic equation for NLS," *Forum of Mathematics, Pi* **9**, e6 (2021), arXiv:1912.09518.

[63] S. Aaronson, "How much atructure is needed for huge quantum speedups?," arXiv:2209.06930 (2022).